


APPROVAL SHEET

Title of Dissertation: STRUCTURAL DETERMINANTS FOR THE
ACTIVATION OF SOLUBLE GUANYLYL CYCLASE

Name of Candidate: Kenneth C. Childers
Doctor of Philosophy, 2019

Dissertation and Abstract Approved: _____



Dr. Elsa. D. Garcin
Associate Professor
Chemistry & Biochemistry

Date Approved: April 23rd 2019

ABSTRACT

Title of Document: STRUCTURAL DETERMINANTS FOR THE
ACTIVATION OF SOLUBLE GUANYLYL
CYCLASE

Kenneth C. Childers, Doctor of Philosophy,
2019

Directed By: Dr. Elsa D. Garcin
Associate Professor
Department of Chemistry and Biochemistry

Soluble guanylyl cyclase (GC-1) converts guanosine 5'-triphosphate (GTP) into cyclic guanosine 3',5'-monophosphate (cGMP), a potent vasodilator. Nitric oxide (NO) binds to an N-terminal heme cofactor and stimulates GC-1 activity 100 – 200-fold, inducing vasodilation. In cardiovascular diseases, GC-1 heme is prone to oxidation which abolishes NO-sensitivity and reduces cGMP turnover, causing vasoconstriction and enhancing oxidative stress. Because GC-1 is central to the pathway regulating vascular function, the enzyme is a target for pharmaceutical intervention to promote GC-1 activity and improve cardiovascular health. However, the structural elements that relay the NO-binding event to the catalytic domain are unknown. We hypothesize that a series of amino acids promotes GC-1 catalytic activity upon NO binding through a network of hydrogen bonds and hydrophobic interactions. Identification of these amino acids will aid structure-based drug design efforts to target dysfunctional GC-1.

To identify these amino acids, we designed, optimized, and tested a luciferase reporter assay, which relies on a cGMP-dependent promoter upstream of the luciferase gene. In an *E. coli* host, GC-1 was expressed and produced cGMP which induced luciferase expression. Luciferase activity was measured in cell lysates as an indirect measurement of GC-1 activity. We optimized this assay by using cAMP-deficient *E. coli* cells to decrease background luciferase activity by ~90%. By targeting distinct structural elements in the catalytic domain through site-directed mutagenesis, we identified several novel activating GC-1 variants and confirmed their effect via extracellular cGMP measurements. When mutants from various regions are combined, we measured synergistic or antagonistic effects, supporting our hypothesis whereby discrete regions in GC-1 act as hotspots for allosteric regulation of GC-1 activity.

Our lab had previously determined the structure of the apo inactive wild-type heterodimeric catalytic domain of GC-1 ($\alpha\beta\text{GC}^{\text{cat}}$). To determine a structure of the active $\alpha\beta\text{GC}^{\text{cat}}$ conformation and to overcome preferential $\beta\beta\text{GC}^{\text{cat}}$ homodimerization, we made several mutants and constructs of the catalytic domain. However, we only crystallized and solved the structure of mutant $\beta\beta\text{GC}^{\text{cat}}$.

Overall, our results describe the design of the first bacterial assay to identify activating GC-1 mutations, and suggest cross talk between various structural elements of the catalytic domain, which regulate GC-1 activity.

STRUCTURAL DETERMINANTS FOR THE ACTIVATION OF SOLUBLE
GUANYLYL CYCLASE

By

Kenneth C. Childers

Dissertation submitted to the Faculty of the Graduate School of the
University of Maryland, Baltimore County, in partial fulfillment
of the requirements for the degree of
Doctor of Philosophy
2019

© Copyright by
Kenneth C. Childers
2019

Dedication

To Mom and Dad

And my sisters Jen, Leah, and Rachel

For your constant support throughout this experience

You all inspire me

Acknowledgements

First, I would like to thank my advisor, Dr. Elsa Garcin. Elsa has been an invaluable mentor throughout graduate school by providing me with essential skills as a scientist. She has shown me that, through innovative problem solving, critical analysis of results, and sheer determination, challenging projects can be overcome. She has also shown me that we never stop learning in science and literature review is never over. I would also like to acknowledge my dissertation committee – Dr. Michael Summers, Dr. Katherine Seley-Radtke, Dr. Lisa Kelly, and Dr. Philip Farabaugh. Their critical feedback on my project has aided in my progression through graduate school and have shown me the true value in thorough observation and analysis in science.

It goes without saying that projects like this are accomplished not alone, but through extensive collaborations. Dr. Thomas Miller ran multiple luciferase assays and also assisted in bio-layer interferometry experiments at the NIH in Dr. David Roberts' lab. Tom was also kind enough to run several luciferase assays during the evening and trained me on the Octet. Luciferase assay results that Tom helped to collect were crucial in our R21 grant. I would also like to thank Dr. Philip Farabaugh and Dr. Zeev Rosenzweig who granted us access to their luminometer and plate reader, respectively. Having access to these instruments on campus helped to expedite my experiments significantly. I would also like to acknowledge Dr. Farabaugh's lab technician, Brooke Luisi, and the Rosenzweig lab members for training me on their labs' instruments. Dr. Donald Hamelberg (Georgia State Univ.) and his lab provided us with preliminary molecular dynamic simulations, which also were crucial for our R21 grant.

Former Garcin lab members were critical in the progression of this project. Franzi provided the framework for this project and I'm thankful for her troubleshooting multiple parts of this project during her time. Joshua Amason and Sam Giannakoulis were the two undergraduates who I trained and helped in experimental design and execution. Josh, I'm sorry you had to leave after we switched cell lines and all of your mutants went unused, but you were nonetheless crucial in this project. Sam, your patience and optimism blow my mind and I hope you never lose either of them (but I do hope you sleep more). Other Garcin lab students were helpful during group meetings as well as commiserating with when classes and lab got rough – Mohsin, John, Pauline, Thomas, Olivia, Joe, Anh, and Amanda.

Thank you to Dr. Katherine Seley-Radtke and Chemistry-Biology Interface (CBI) members for listening to practice talks, providing critical feedback, and participating in interesting discussions Monday evenings. Dr. Seley encouraged my growth as a graduate student, not just by being on my committee and watching my project grow, but also by pressing CBI members to discuss a variety of topics from science ethics to graduate school. CBI members astound me each week with their insight into each other's projects and I will be forever grateful for my time in the program.

I would be remiss if I did not acknowledge Dr. Aaron Smith and his graduate students Alex and Verna. During Elsa's sabbatical, the Smith lab has been a "surrogate lab" for me. Thank you for adopting me, listening to my practice talks during group meetings and keeping me social. I greatly appreciated your check-ins, especially during these last few months when things were stressful and I sat in a dark lab in front of my laptop.

During graduate school, I was lucky to have met incredible graduate students who I have formed a tight bond with. First, I would like to thank Mike, Danielle, Anand, and Casey. Lunches with you were talkative, hilarious, and got me through the early years of grad school. I hesitate to say playing board games and long lunches at True Grits were a waste of time because they were so memorable for me. You four were a reprieve from work, even when we did inevitably discuss work and the stress associated with it. I'm also thankful that we've all kept in touch, despite all of us moving on since grad school. I would also like to thank Alex Winton. I will be forever-grateful for you corrupting me with a cigar and drinks on my birthday and for our nights with Nick, either at the cigar lounge, my apartment, or Alex's backyard in front of a fire pit. Other friends that I have met in graduate school have helped relieve stress and I've enjoyed watching us progress (and yes, I'm doing this floor-by-floor) – Adam, Nopondo, Miji, Evgenia, Scott, Flair, Brian C., Mary, Arun, Brian S., Eric, Pietro, Dan, Stacy, Chris, Janae, Tonya, and Rachael. I'm lucky to have met each of you and progressed through graduate school together.

I would not have made it this far without the endless support of my family. Mom and Dad have encouraged me to pursue a career in science since high school chemistry. Through my undergraduate career in Arizona, they pushed me through grueling coursework and watched me graduate. Within a month of obtaining my undergraduate degree, they had helped me move to Baltimore for graduate school. I'm particularly thankful for them flying me back and forth during holidays to see them and relieve some stress. I would also like to thank my sisters- Jen, Leah, and Rachel. You three are some of my biggest role models and I want to be like each of you when I grow up. You make me laugh like a complete idiot and I strive to do the same to you when we are together. Also a special thank you to my brother-in-law Josue who, not only has been an ideal brother-in-law to me, but also helped me relieve stress through hours of playing games. If not for my family, it's difficult to imagine where I would be.

Table of Contents

Dedication	ii
Acknowledgements	iii
List of Tables	viii
List of Figures	ix
Chapter 1: Nitric Oxide: Synthesis and Action.....	1
1.1. Abstract	1
1.2. Introduction.....	2
1.3. NO synthesis by nitric oxide synthase enzymes	3
1.3.1. Mechanism of NOS enzymes	6
1.3.2. Structure of NOS enzymes	7
1.4. NO Pathways	12
1.4.1. NOSI and neurotransmission	12
1.4.2. NOSII and high NO levels	14
1.4.3. NOSIII and vasodilation.....	15
1.5. Bacterial NO	17
1.6. Nitrite/Nitrate and NO	19
1.7. Cardiovascular diseases and treatments.....	20
1.8. Summary	22
Chapter 2: Structure/Function of the Soluble Guanylyl Cyclase Catalytic Domain ..	24
2.1. Abstract	24
2.2. Introduction.....	25
2.3. GC-1 domain architecture.....	28
2.4. Structural studies of the cyclase catalytic domains.....	31
2.4.1. The homologous adenylyl cyclase enzyme	31
2.4.2. Bacterial guanylyl cyclase.....	35
2.4.3. Eukaryotic guanylyl cyclase.....	37
2.4.4. Human mutant guanylyl cyclase	38
2.4.5. Human wild-type guanylyl cyclase	41
2.4.6 The guanylyl cyclase of the fusion protein RhoGC	44
2.5. Structural determinants for catalytic activity	46
2.5.1. Activating mutations	46
2.5.2. Inactivating mutations	48
2.5.3. Cys-NO Modification in GC-1 Desensitizes the Enzyme to NO	51
2.5.4. Small Molecules Targeting the Catalytic Domain	53
2.6. Protein-protein interactions regulating GC-1 activity.....	56
2.6.1. β HNOX- α β GC ^{cat} interactions.....	56
2.6.2. Interactions with thioredoxin (Trx)	60
2.6.3 Interactions with protein-disulfide isomerase (PDI)	60
2.7. Conclusions.....	61
2.8 Dissertation Outline	63
2.8.1 Specific Aims	63
Chapter 3: Novel Synergistic Mutations in Soluble Guanylyl Cyclase Reveal a Key Role for Interfacial Dorsal Flaps in the Activation Mechanism	65
3.1. Abstract	65
3.2. Introduction.....	66
3.3. Materials and Methods.....	68

3.3.1. Materials.....	68
3.3.2. Plasmids and Gene Construction.....	68
3.3.3. Cell Growth Conditions	69
3.3.4. Western Blot.....	70
3.3.4. Luciferase Assay	70
3.3.5. cGMP/cAMP Immunoassays	71
3.3.6. Multi-Sequence Alignment	72
3.3.7. Accession Numbers.....	72
3.4. Results.....	72
3.4.1. Assay Promiscuity and Reduction of Background cAMP Signal	72
3.4.2. Luciferase Activity Induction by Wild-type GC-1 and Inhibition by Inactive GC-1 Variants	77
3.4.3. Variants Along Catalytic Domain Dorsal Flaps Modulate GC-1 Activity.....	88
3.4.4. Variants at the Dimer Interface Activate GC-1 and Synergize with Dorsal Flap Variants	93
3.4.5. The β Cys541Gly Mutation Reduces Substrate Specificity and Synergizes with Other Variants to Increase GC-1 Activity.....	94
3.5 Discussion	95
3.5.1. A Luciferase Reporter Assay for Heterologous GC-1 Activity in <i>E. coli</i>	96
3.5.2. Multiple Catalytic Domain Structural Elements Control GC-1 Activity	98
3.7. Acknowledgment	108
Chapter 4: Purification and Characterization of the Activated GC-1 Catalytic Domain	109
4.1. Introduction.....	109
4.2. Materials and Methods.....	111
4.2.1. Mutagenesis.....	111
4.2.2. Expression and Purification of the quadruple α Val587Ile/Val589Thr/Lys590Arg/ β Met537Asn $\alpha\beta$ GC ^{cat} variant	111
4.2.3. Crystallization and Structure Determination of Met537Asn $\beta\beta$ GC ^{cat}	113
4.2.4. Bio-Layer Interferometry	114
4.2.5. Design, Cloning, Expression, and Partial-Purification of Lnk. $\alpha\beta$ GC ^{cat}	114
4.2.6. Activity Assays	118
4.3. Results.....	119
4.3.1. Purification and Crystallization Attempts of Activated $\alpha\beta$ GC ^{cat}	119
4.3.2. Crystal Structure of Met537Asn $\beta\beta$ GC ^{cat}	120
4.3.3. Bio-Layer Interferometry	126
4.3.4. Expression and Purification of “Linked” $\alpha\beta$ GC ^{cat}	127
4.3.5. Activity of Mixed Catalytic Subunits with Wild-type and Mutant $\alpha\beta$ GC ^{cat} and Semi-purified Lnk. $\alpha\beta$ GC ^{cat}	131
4.4. Discussion	134
4.4.1. Structure of Met537Asn $\beta\beta$ GC ^{cat} is similar to that of Wild-type $\beta\beta$ GC ^{cat}	134
4.4.2. Interactions Between Catalytic Subunits.....	135
4.4.3. Activity Measurements Show that Catalytic Domains are Active in Cell Lysates	136
4.5. Conclusions.....	137
4.6. Acknowledgments.....	138
Chapter 5: Summary, Future Outlook, and Conclusions	139
5.1. Summary	139
5.1.1. Aim 1: Identify the amino acids that orient the catalytic domain and promote full catalytic activity	139

5.1.2. Aim 2: Structurally characterize the activated $\alpha\beta\text{GC}^{\text{cat}}$ domain.....	140
5.1.3. Consequences for the NO/GC-1/cGMP Field	141
5.2. Future Outlook	144
5.2.1. Future Studies Using the Novel Luciferase Reporter Assay	144
5.2.2. Elucidation of Regulatory Elements for $\alpha\beta\text{GC}^{\text{cat}}$ Activation	148
5.2.3. Characterizing the regulatory role of N-terminal GC-1 domains.....	150
5.3. Conclusions.....	151
5.3.1. Aim 1: Identify the amino acids that orient the catalytic domain and promote full catalytic activity	151
5.3.2. Aim 2: Structurally characterize the activated $\alpha\beta\text{GC}^{\text{cat}}$ domain.....	151
Appendices.....	153
1. Appendix A.....	153
1.1 Supporting Information	153
Bibliography	164

List of Tables

Table 1.1. NOSI phosphorylation sites and roles	11
Table 1.2. NOSIII phosphorylation sites and roles.....	11
Table 2.1. Key catalytic residues in adenylyl cyclase and guanylyl cyclases	34
Table 2.2. Basal guanylyl cyclase activities. Comparison of reported specific activities (nmol cGMP/min/mg protein) and calculated specific activities adjusted for amounts of heterodimers (100% for GC-1) and normalized to pmol of protein (fmol cGMP/min/pmol heterodimer). @: activity measured in cell lysate. #: calculated activity assuming 100% heterodimeric $\alpha\beta\text{GC}^{\text{cat}}$. \$: activity measured using $\alpha 661\text{-}\beta\text{GC}^{\text{cat}}$ with 82.5% heterodimers as measured (30 residues truncated from $\alpha\text{GC}^{\text{cat}}$ C-terminus). N/D: not determined. All assays performed at 37 °C except where noted (*).	40
Table 3.1. List of plasmids for reporter assay. ^a Oligopeptide transporter X cyclic guanosine 3',5'-monophosphate reporter gene: luciferase.	74
Table 3.2. Extracellular cAMP levels from BL21(DE3) <i>cyaA</i> ⁺ and BL21(DE3) <i>cyaA</i> ⁻ (<i>cyaA</i> deficient) cells. Samples were plated in duplicate and averaged from three experimental replicates. Error represents the standard error of the mean from three or more independent experiments. ^a Not detectable.....	77
Table 3.3. Luciferase activity for wild-type and mutant GC-1. Luciferase assay was measured in cell lysates from cell pellets collected after 72 hour of cell growth and were plated in triplicate. Error represents the standard error of the mean from three or more independent experiments. Statistical significance between wild-type and mutant GC-1 samples was calculated using the Student's <i>t</i> -test (* <i>p</i> < 0.05; ** <i>p</i> < 0.01; *** <i>p</i> < 0.001). ^a Not detectable.	79
Table 3.4. Extracellular cGMP and cAMP levels from wild-type and mutant GC-1 samples. The cGMP and cAMP levels were measured in the extracellular supernatant after 72 hours of cell growth and were plated in duplicate. Error represents the standard error of the mean from three or more independent experiments. ^a Not detectable.	82
Table 3.5. Extracellular cGMP from wild-type and inactive GC-1 variants. ^a Samples were plated in duplicate and averaged from two or more experimental replicates. Error represents a 95% confidence interval. ^b Not detectable. ^c Not measured.	88
Table 4.1. X-Ray data collection and refinement statistics for Met537Asn $\beta\text{GC}^{\text{cat}}$	122
Table 5.1. Extracellular cGMP levels from wild-type and $\beta\text{Arg536Ala}$ GC-1 cells. cGMP levels were measured in the extracellular supernatant after 72 hours of cell growth using the R&D immunoassay kit and were plated in duplicate. Error represents the standard error of the mean from three or more independent experiments.	147

List of Figures

Figure 1.1. Overall mechanism and architecture of NOS enzymes. (a) General mechanism for NO production. (b) The overall architecture of NOS enzymes is very similar and contains an N-terminal NOS oxygenase module (NOSox), an intervening Ca^{2+} /calmodulin binding region (CaM) and a C-terminal NOS reductase module (NOSred). (c) Specific features of each NOS isoform include a PDZ domain for NOSI, myristoylation and palmitoylation sites in NOSII. All three isoforms contain a C-terminal tail (CT). NOSI and NOSIII also contain an autoinhibitory helix (AH) and a CD2A inhibitory element, as well as various phosphorylation sites. (d) X-ray structure of the human NOSII oxygenase module. (e) X-ray structure of Ca^{2+} /CaM bound to a NOSIII-derived peptide. (f) X-ray structure of the rat NOSI reductase module..... 4

Figure 1.2. Overall NOS pathways and regulation. (a) NOSI becomes activated with increased Ca^{2+} concentrations, phosphorylation and protein–protein interactions. NOSI-derived NO improves blood flow and increases neuronal cell growth (1). Hyperactivated NOSI can lead to excitotoxicity and apoptosis (2). NOSI activity is shutdown through phosphorylation and proteasomal degradation (3). (b) NOSII expression is induced by various cytokines. Immune cells such as macrophages and neutrophils use NOSII to generate cytotoxic levels of NO to kill invading pathogens (1). Excessive NOSII activity can damage healthy cells leading to inflammation and cell death (2). NOSII is neutralised through proteasomal degradation and a negative feedback loop with NF- κ B (3). (c) NOSIII is activated similarly to NOSI. A variety of kinases, protein–protein interactions and increased Ca^{2+} levels enhance NOSIII activity. NOSIII-derived NO inhibits platelet aggregation and dilates neighbouring blood vessels (1). Reactive oxygen species (ROS) and low BH4 levels can uncouple NOSIII activity and lead to superoxide formation, which in turn decreases available NO and exacerbates oxidative stress (2). Phosphorylation and proteasomal degradation turn this pathway off (3). 13

Figure 1.3. The NO–GC1–cGMP pathway and therapeutic targets. NO is generated in the endothelium and diffuses to smooth muscle cells. GC1 (blue) is the primary target for NO binding, which triggers an increase in cGMP generation. Second messenger cGMP activates PKG, which phosphorylates downstream targets for improved blood flow. Reactive oxygen species (ROS) and phosphodiesterase-5 (PDE5) can inhibit this pathway (red arrows). Several pharmacological targets for this pathway are shown with green arrows..... 16

Figure 1.4. The nitrate/nitrite/NO pathway. Nitrate is obtained primarily in the diet from leafy greens and cured meats. Oral bacteria oxidise nitrate to nitrite, which acts as an important source of NO under hypoxic and acidic conditions. 20

Figure 2.1. Overview of the NO/GC-1/cGMP pathway. The NO/GC-1/cGMP pathway mediates vasodilation and vasoconstriction and is regulated by a variety of inhibitors and activators. Green arrows indicate pathway activation/stimulation and red arrows indicate pathway inhibition. Abbreviations- CaM: calmodulin. NOSI/II/III: nitric oxide synthase-isoforms 1, 2, and 3. GC-1: soluble guanylyl cyclase. GTP: guanosine 5'-triphosphate. cGMP: cyclic guanosine 3',5'-monophosphate. PKG: protein kinase G. PDE: phosphodiesterase. ROS: reactive oxygen species. ODQ: 1H-(1,2,4)oxadiazolo(4,3-a)quinoxaline-1-one. MANT-NTP: 2',3'-O-(N-methylanthraniloyl) nucleotide 5'-triphosphate. TNP-NTP: 2',3'-O-(2,4,6-trinitrophenyl) nucleotide 5'-triphosphate..... 25

Figure 2.2. GC-1 is a multi-domain enzyme. General domain architecture of GC-1 (top) and crystal structures of homologous or wild-type GC-1 domains (below). HNOX: Heme Nitric oxide-Oxygen binding (PDB code 2O09, red, *Nostoc* PCC 7120 HNOX). PAS: Per-Arnt-Sim (PDB code 4GJ4, cyan, *Manduca sexta* GC-1). CC: Coiled-Coil (PDB code 3HLS, green, *Rattus norvegicus* β GC-1). GC: Guanylyl Cyclase (PDB code 4NI2, gold, *Homo sapiens* $\alpha\beta$ GC-1). Numbering for the α and β chains is from *Homo sapiens* GC-1..... 30

Figure 2.3. Structural overview of adenylyl and guanylyl cyclases. (a) C2/C2 homodimer (C2a, dark/C2b, light yellow) with two forskolin molecules (FOK, cyan) at the dimer interface (PDB code 1AB8). (b) C1/C2 heterodimer (light red/light yellow, respectively) with bound activators Gsa (light blue) and forskolin (FOK, cyan); substrate 2',3'-dideoxyadenosine 5'-triphosphate (2',3'-ddATP, dark blue) and two Mg^{2+} ions (green, PDB code 1CJU). (c) *Synechocystis* PCC 6803 Cya2 GC (GC_{Cya2}) homodimer (green, PDB code 2W01). (d) *Chlamydomonas reinhardtii* CYG12 GC (GC_{Cr}) homodimer (purple, PDB code 3ET6). (e) Human β GCcat homodimer (dark/ light yellow, PDB code 2WZ1). (f) *Blastocladiella emersonii* RhoGC cyclase (GC_{Rho}) monomer (PDB code 6AO9). (g, h) Wild-type *Homo sapiens* $\alpha\beta$ GC^{cat} heterodimer (α GC^{cat} magenta, β GC^{cat} yellow) and putative regions for domain activation (PDB code 4NI2) viewed on the ventral (g) and dorsal (h) side.... 33

Figure 2.4. Alignment of amino acid sequences of cyclase domains. The multi sequence alignment of guanylyl cyclase domains with available x-ray structures was performed with CLUSTAL Omega and displayed using ESript [113,114]. The sequences used are *Homo sapiens* wild-type GC-1 α GC^{cat} and β GC^{cat} (4NI2-A and 4NI2-B, respectively), *C. reinhardtii* CYG12 GC_{Cr} cyclase (3ET6), *Blastocladiella emersonii* GC_{Rho} cyclase (6AO9), and *Synechotistis* PCC6803 GC_{Cya2} cyclase (2W01). The secondary structure elements (α helices: α 1- α 5, β strands: β 1- β 10, TT: β -turns) represented above the sequence belong to β GC^{cat}. Numbering is indicated for all sequences. Residues important for catalysis are highlighted 1-8 above the sequence alignment as in Table 2.1. Invariant residues are highlighted in red boxes while similar residues across all sequences are highlighted in yellow boxes. The consensus sequence (identity > 70%) is shown below the alignment.

Upper case represents identity; lower case represents consensus level>0.5; ! is anyone of IV residues, # is anyone of NDQEBZ (from BloSUM32 table), dots are residues that are not conserved. Stars above the sequence represents residues with alternate positions. 36

Figure 2.5. Model of activated $\alpha\beta\text{GC}^{\text{cat}}$. Theoretical model of activated $\alpha\beta\text{GC}^{\text{cat}}$ bound to Mg^{2+} and 2,3'-ddATP. The model was obtained by superimposition of inactive $\alpha\beta\text{GC}^{\text{cat}}$ (PDB code 4NI2) on “active” adenylyl cyclase structure (PDB code 1CJU). Superposition of the inactive and active GC^{cat} subunits independently shows that the 26° rigid body rotation of the $\alpha\text{GC}^{\text{cat}}$ subunit around $\beta\text{GC}^{\text{cat}}$ allows structural elements of both subunits to close the active site. In addition, the substrate binding loop become more structured in the active model. Inset depicts structural rearrangement at the substrate binding pocket containing two Mg^{2+} ions (green) and 2',3'-dideoxyadenosine 5'-triphosphate (2,3,-ddATP). $\alpha\text{GC}^{\text{cat}}$ (magenta-inactive, violet-active) and $\beta\text{GC}^{\text{cat}}$ (yellow-inactive, orange-active)..... 41

Figure 3.1. Luciferase activity from BL21(DE3) (*cyaA*+) and BL21(DE3) *cyaA*-deficient (*cyaA*-) cells transformed with pOPTXcGMPRE:LUC. Data represent an average of three or more experiments plated in triplicate. Error bars represent the standard error of the mean. Statistical significance between *cyaA*⁺ and *cyaA*⁻ cells at 24 hours was analyzed using Student's t-test (**p* < 0.05). 76

Figure 3.2. Amino acids in the GC-1 catalytic domain targeted for mutagenesis. (a) Ventral (left) and dorsal (right) sides of the GC-1 catalytic domain ($\alpha\beta\text{GC}^{\text{cat}}$) in the predicted activated conformation with Mg^{2+} and dideoxy-ATP (ddATP) bound in the active site. (b) Amino acids αCys595 and βAsn548 were mutated to inactivate GC-1. (c) Amino acids αCys595 , αGlu526 , and βThr474 were predicted to form an interfacial hydrogen-bond network¹¹. (d) βCys541 in the substrate-binding pocket was proposed to modulate substrate specificity.³⁵ (e) Amino acids from both dorsal flaps were mutated. 78

Figure 3.3. Luciferase activities induced by inactive GC-1 variants. Data represent an average of one or more experiments. In cases of one experiment, data represent an average of three technical replicates. Statistical comparison between wild-type and mutant GC-1 at the 72 hour time point was analyzed using the Student's *t* test (**p* < 0.001). Error bars represent a 95% confidence interval. 87

Figure 3.4. Alignment of guanylyl cyclase and adenylyl cyclase dorsal flaps. (Top) Alignment was generated with CLUSTAL Omega⁵⁰⁻⁵² and visualized with ESPript.^{40,41} Numbering corresponds to the dorsal flap sequence for $\alpha\text{GC-1}$ (*H. sapiens*). Similar residues (red letters) are in blue boxes and invariant residues are highlighted in red. Residues in *H. sapiens* $\alpha\beta\text{GC-1}$ that have been targeted for mutagenesis in this study are highlighted as follows: αVal587 (green), αVal587 (yellow), αLys590 (pale green), αMet591 (pink), βIle533 (blue), βMet537 (purple), and βPro538 (teal). Uniprot accession codes are

- indicated for each sequence. (Bottom) Graphic representation of conserved residues generated with WebLogo.⁵³ 92
- Figure 3.5. Model for wild-type CC-GC^{cat}. (a) The model was generated with SWISSMODEL^{54,55} with the 3D structure of the Cya_{sol} helical and cyclase domains as a template (PDB code 5O5K). Residues 442-659 (blue) and 382-607 (orange) were modeled for α GC-1 and β GC-1, respectively. Key residues from the dorsal flaps mutated in this study are shown as sticks and labeled. The helix-turn-Helix (α HtH and β HtH) motifs of the penultimate coiled coil domain are indicated. Magnesium ions (green balls) and dideoxy-ATP (sticks, ddATP) are included in the model. (b) Stereoview of the central positioning for the dorsal flaps, which are sandwiched between the helix-turn-helix motif and the active site of the catalytic domain. The view is the same as in (a). Key residues are shown in sticks and colored in blue (α GC) and orange (β GC). (c) Stereoview of the hydrophobic pocket around residue β Thr474. 103
- Figure 4.1. Purification of $\alpha\beta$ GC^{cat}. The catalytic domains of GC-1 were purified and used for crystallization trials, BLI experiments, and activity assays. 119
- Figure 4.2. Crystal structure of Met537Asn $\beta\beta$ GC^{cat}. Dorsal side (left) and ventral side (right) with the Met537Asn mutation highlighted in sticks (magenta). 121
- Figure 4.3. Stereo view (convergent) of electron densities for covalently-modified Cys489. Electron density was visualized with COOT¹⁹⁵ and used to determine which modification best fit the difference map (green and red). Modifications that were considered were a) dimethyl arsenic, b) sulfenic acid, c) homocysteine, and d) mercaptocysteine. 124
- Figure 4.4. Met537Asn $\beta\beta$ GC^{cat} with dimethyl arsenic-modified Cys489. Dorsal view of Met537Asn $\beta\beta$ GC^{cat} (top) with dimethyl arsenic-modified Cys489 (CAS 489) (bottom). 125
- Figure 4.5. Bio-Layer Interferometry (BLI) measurements on $\alpha\beta$ GC^{cat} interactions. (a) Loading: 6xHis- β GC^{cat} (2.2 μ M) was loaded onto anti-His antibody-coated sensors. (b) Association: varying concentrations of α GC^{cat} was used to bind to β GC^{cat}. (c) Dissociation: sensors were dipped into fresh buffer and dissociation rates of α GC^{cat} were recorded. 127
- Figure 4.6. Overview of Lnk. $\alpha\beta$ GC^{cat} construct. The C-terminus of α GC^{cat} (aa. 467 – 690) was fused to the N-terminus of β GC^{cat} (aa. 407 – 619), linked by a TEV cleavage site. A 6xHis-Trx-SUMO tag was included at the N-terminus for improved solubility, and a C-terminal AviTag preceded by a PreScission Protease cleavage site was added at the C-terminus for BLI studies. 128
- Figure 4.7. Western blot of Lnk. $\alpha\beta$ GC^{cat} crude and clarified lysates. (A) Ponceau red stain for total protein in cell lysates. (B) Western blot using rabbit anti- α GC^{cat} (res. 673-690) primary antibodies confirms expression and solubility of Lnk. $\alpha\beta$ GC^{cat}. 129
- Figure 4.8. SDS-PAGE gels during purification of Lnk. $\alpha\beta$ GC^{cat}. Lnk. $\alpha\beta$ GC^{cat} purity was assessed using SDS-PAGE. (A) The 6xHis-Trx-SUMO tag was cleaved overnight with ULP1. (B) SDS-PAGE of Lnk. $\alpha\beta$ GC^{cat} after elution

from anion exchange where GroEL chaperone protein remained a major contaminant.....	129
Figure 4.9. Biotinylation of Lnk. $\alpha\beta\text{GC}^{\text{cat}}$. Semi-purified Lnk. $\alpha\beta\text{GC}^{\text{cat}}$ was biotinylated using BirA, but precipitated with GroEL.....	130
Figure 4.10. SDS-PAGE of semi-purified Lnk. $\alpha\beta\text{GC}^{\text{cat}}$. Lnk. $\alpha\beta\text{GC}^{\text{cat}}$ was semi-purified using a 5 mL Talon column and 12 μL was analyzed on SDS-PAGE.	131
Figure 4.11. Activities of wild-type and mutant $\alpha\beta\text{GC}^{\text{cat}}$ in cell lysate. Activity from cells expressing wild-type or mutant $\alpha\beta\text{GC}^{\text{cat}}$ was analyzed using 100 μL of clarified cell lysate. Data represent an average of two technical replicates from one experiment. Statistical comparison between wild-type and mutant $\alpha\beta\text{GC}^{\text{cat}}$ was analyzed using the Student's <i>t</i> test. Error bars represent one standard deviation.....	133
Figure 4.12. Activities of wild-type $\alpha\beta\text{GC}^{\text{cat}}$ (black) and Lnk. $\alpha\beta\text{GC}^{\text{cat}}$ in cell lysates (green) and semi-purified (teal). Activity from cell lysates used 100 μL of clarified lysate and activity from semi-purified protein used ~100 pmol of Lnk. $\alpha\beta\text{GC}^{\text{cat}}$. Data represent an average of two technical replicates from one experiment. Error bars represent one standard deviation.....	134
Figure 5.1. Model of GC-1 NO-stimulation through releasing putative inhibition by HNOX. (Left) GC-1 activity is inhibited through putative interactions between GC^{cat} and the βHNOX domain. (Right) Upon NO binding, inhibition is relieved and optimal GC-1 activity is restored.	142
Figure 5.2. Model of GC-1 NO-stimulation through hotspots. (Left) GC-1 maintains basal activity. (Right) NO-binding reorients key amino acids in hotspots along GC-1 and propagates activation to the GTP-binding site through hydrogen bonding and hydrophobic interactions.....	143
Figure 5.3. Luciferase activity induced by wild-type GC-1 and $\beta\text{Arg536Ala}$ GC-1. Data represent an average of three or more experiments. Error bars represent the standard error of the mean. Statistical comparison between wild-type and $\beta\text{Arg536Ala}$ GC-1 at the 72 hour time point was analyzed using the Student's <i>t</i> test (* <i>p</i> < 0.05).	146
Figure 5.4. Highly-conserved residues in GC^{cat} . $\alpha\text{GC}^{\text{cat}}$ (violet) and $\beta\text{GC}^{\text{cat}}$ (orange) with residues that are 100% conserved across 27 GC-1 and AC catalytic sequences (green).....	150

Chapter 1: Nitric Oxide: Synthesis and Action

Reproduced with permission from Kenneth C. Childers and Elsa D. Garcin. "Nitric Oxide: Synthesis and Action." Encyclopedia of Life Sciences, September 2017, doi: 10.1002/9780470015902.a0000634.pub2 Copyright 2017 Wiley

1.1. Abstract

Nitric oxide (NO) is a diatomic radical implicated in a variety of pathways including vascular homeostasis, neurotransmission and immune defense. NO is produced endogenously by three nitric oxide synthases (NOS) and can also be formed from nitrates and nitrites. Several mechanisms regulate NOS function, including protein–protein interactions, posttranslational modifications, cell localization, calcium levels, substrate availability, and the cell redox status. Picomolar NO concentrations activate guanylyl cyclase to increase cGMP levels and lead to vasodilation and memory formation. Excess NO concentrations cause posttranslational modifications of cellular components and formation of peroxynitrite leading to inflammation and cell death. Due to its involvement in multiple pathways and high reactivity with a myriad of downstream targets, tight regulation of NO production is crucial to maintain cellular function. Major advancements in understanding NO chemistry, production and downstream signaling have provided new avenues to target this pathway for the treatment of cardiovascular, neurodegenerative and autoimmune diseases.

1.2. Introduction

Nitric oxide (NO) is a small reactive gaseous molecule, mostly known as a common air pollutant present in vehicle emissions and cigarette smoke. However, in the early 1980s, research by Robert Furchgott, Ferid Murad, Louis Ignarro and Salvador Moncada astonished the entire scientific community, showing that NO was produced endogenously in the human body and played a key role as a signalling molecule.¹⁻⁴ In 1998, the Nobel Prize in Physiology and Medicine was awarded to Furchgott, Murad and Ignarro for their discovery of NO as a signaling molecule in the cardiovascular system. In addition to this role, NO has been shown to play key roles in virtually every organ and to affect a plethora of cellular functions, including neurotransmission, memory, learning, angiogenesis, penile erection, platelet aggregation, gene regulation, and to be involved in numerous diseases, including cardiovascular diseases (CVD), autoimmune diseases, septic shock, asthma, cancer, glaucoma, neural degeneration, pulmonary hypertension (PH) and many more. Much has happened since this article was originally published in 2001 regarding the mechanism of NOS enzymes, the discovery of bacterial homologues, the discovery of other non-NOS sources of NO in the body and the efforts to target the NO–GC1–cGMP pathway for therapeutic use. It is impossible to cite all the work on NO (>60,000 papers in the past 10 years with ‘NO’ as a search term), and we apologize in advance to those whose work is not included here.

1.3. NO synthesis by nitric oxide synthase enzymes

NO is synthesized by nitric oxide synthase enzymes (NOS) that catalyze the five electron oxidation of L-arginine into L-citrulline and NO (**Figure 1.1a**, and **section 1.3.1** below). In mammals, three isozymes have been identified: NOSI (neuronal NOS, nNOS) was originally isolated from neuronal tissues; NOSII (inducible NOS, iNOS) was isolated from macrophages and NOSIII (endothelial,

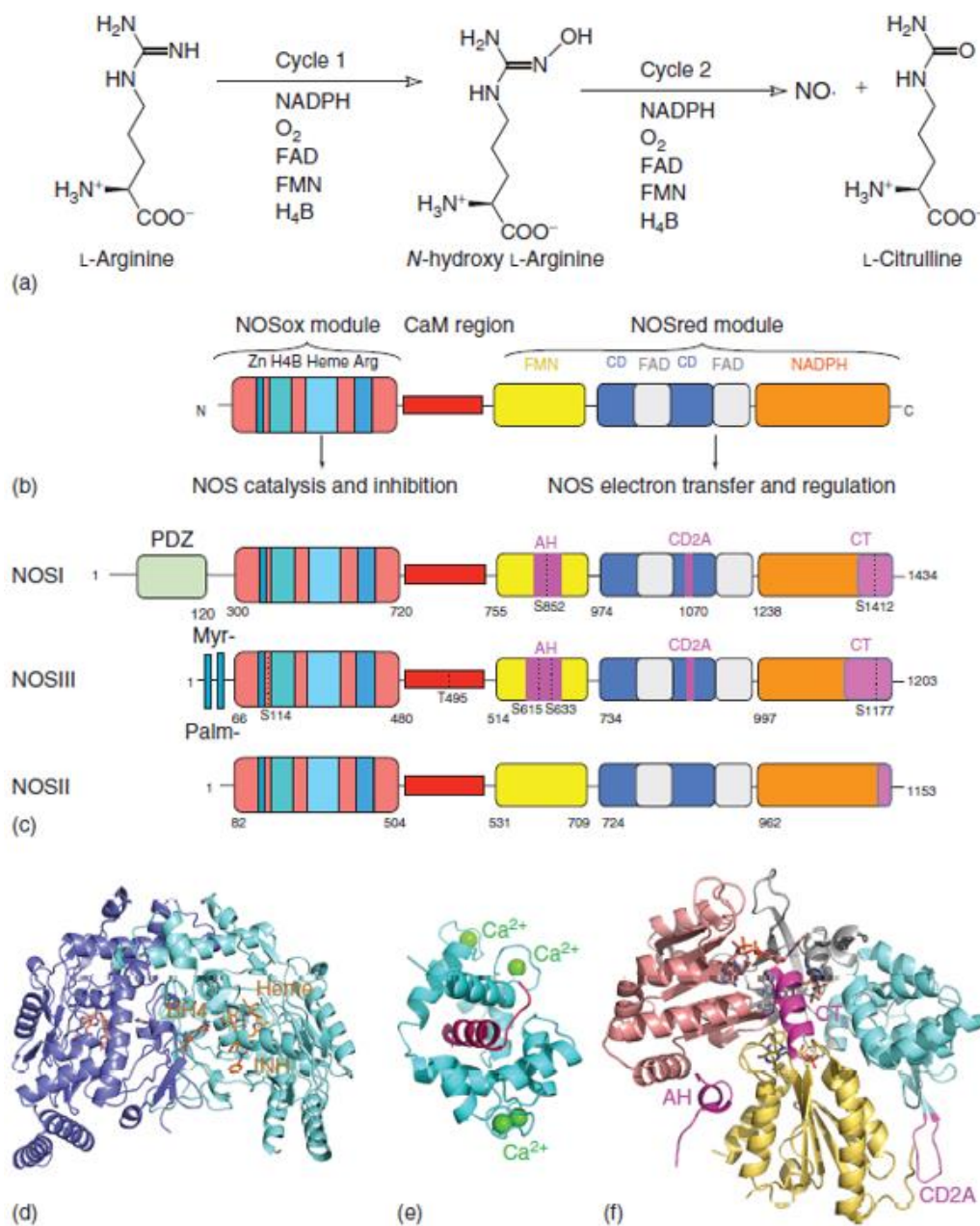


Figure 1.1. Overall mechanism and architecture of NOS enzymes. (a) General mechanism for NO production. (b) The overall architecture of NOS enzymes is very similar and contains an N-terminal NOS oxygenase module (NOSox), an intervening Ca²⁺/calmodulin binding region (CaM) and a C-terminal NOS reductase module (NOSred). (c) Specific features of each NOS isoform include a PDZ domain for NOSI, myristoylation and palmitoylation sites in NOSII. All three isoforms contain a C-terminal tail (CT). NOSI and NOSIII also contain an autoinhibitory helix (AH) and a CD2A inhibitory element, as well as various phosphorylation sites. (d) X-ray structure of the human NOSII oxygenase module. (e) X-ray structure of Ca²⁺/CaM bound to a NOSIII-derived peptide. (f) X-ray structure of the rat NOSI reductase module.

eNOS) was isolated from endothelial cells. Since their original discovery, NOS isozymes have been found in multiple other tissues, rendering their nomenclature based on cell type obsolete. It is also generally believed that NOSI and NOSIII are constitutively expressed, while NOSII is expressed in response to stimuli, including cytokines and lipopolysaccharides. However, levels of NOSI and NOSIII can vary depending on various stimuli (shear stress, hormones, reactive oxygen species (ROS), hypoxia and cytokines) and constitutive forms of NOSII have been found in slow-twitch skeletal muscle fibers. The three NOS isozymes differ in length (130–160 kDa), sequence (50–60% sequence identity among isozymes), tissue distribution, expression (constitutive versus induced), activation by Ca^{2+} /calmodulin (CaM) and activity level (low versus high NO production). Regardless, all NOS isozymes function as obligate homodimers and share similar domain architectures (**Figures 1.1b** and **1.1c**): an N-terminal oxygenase module (NOSox) and a C-terminal reductase module (NOSred) separated by a calmodulin-binding region (the identification of the different NOS domains and cofactors has been reviewed.⁵ NOS enzymes are unique as they require five cofactors for activity: iron protoporphyrin IX (heme), tetrahydrobiopterin (H4B, BH₄), FAD, and FMN, Ca^{2+} /calmodulin (CaM) and NADPH. The N-terminal catalytic NOSox module shares no homology to other proteins, contains structural elements involved in dimerization and binds heme, H4B, and substrate L-arginine. The C-terminal NOSred module is homologous to cytochrome P450 reductase, contains binding sites for NADPH, FAD, and FMN, and provides electrons for NO synthesis. Electrons flow from NADPH to FAD to FMN of NOSred in one polypeptide to heme in the NOSox module of the adjacent

polypeptide. In addition, the NOSred module contains numerous sequence elements involved in the regulation of NOS activity (see **section 1.3.2.5** below). Finally, Ca^{2+} /calmodulin binding to all three NOS isozymes facilitates electron transfer from NADPH to the flavins and from FMN to heme. Various studies have demonstrated differential calcium sensitivity among the NOS isozymes. Elevated Ca^{2+} allows CaM to bind to this region in NOSI and NOSIII, while NOSII is calcium-insensitive, due to its very high affinity for Ca^{2+} /CaM.⁶

1.3.1. Mechanism of NOS enzymes

The exact mechanism of NO synthesis by NOS is still unknown. Numerous studies have provided critical insights into this complex mechanism, and several competing models have been proposed (reviewed in ⁷). All agree that NOS enzymes catalyze the production of NO in two monooxygenation steps that consume 3 electrons and 2 oxygen molecules: the first step includes heme-based oxidation of the substrate L-arginine (L-arg) into the stable intermediate N-hydroxy-L-arginine (NOHA) and requires 2 electrons provided by NOSred and BH₄. The second step is the oxidation of NOHA into L-citrulline, a reaction that requires a single electron and generates one NO• molecule (**Figure 1.1a**). The first step is similar to the oxygen activation reaction catalyzed by cytochrome P450, while the second step is specific to NOS. In addition to its unique H4B cofactor, which also participates in the catalytic mechanism, NOS is unique in that it catalyzes two very different monooxygenation reactions within a single active site.

In conditions where H4B levels are limiting, NOS uncoupling occurs, and superoxide rather than NO is produced. Under oxidative stress, superoxide is also formed via NADPH oxidase and xanthine oxidase. Reaction with NO forms peroxynitrite, another potent oxidant. This pathological process limits NO bioavailability during CVD (see **section 1.7**).

1.3.2. Structure of NOS enzymes

High-resolution crystal structures for all NOS modules, as well as low resolution of holoenzymes determined by electron microscopy, are available. These structures have provided critical insights into the binding sites for cofactors and substrates, the structural determinants for activity and dimerization and the mechanisms by which NOS activity is regulated. In addition, a large number of crystal structures of the NOSox module in complex with inhibitors have revealed key isozyme-specific features crucial to selectively inhibit NOS for therapeutic applications.

1.3.2.1. NOS oxygenase module

The first crystal structures of the N-terminal murine inducible NOSox module were determined in the late 1990s and confirmed a novel fold for this enzyme family. The structure of the truncated NOSII oxygenase module⁸ shows a single α - β domain originally described as a left-hand baseball catcher's mitt with heme located in the palm of the mitt. The subsequent structure determination of dimeric NOSII oxygenase module showed the interconnectedness of the heme, substrate and H4B binding sites⁹.

The heme is buried in the core of the protein and is coordinated by a cysteine on the proximal side (**Figure 1.1d**). The distal heme side is connected to the solvent through a 30-Å-deep funnel-shaped tunnel created by NOSox dimerization, allowing diffusion of substrate L-arginine, oxygen, NO and NOS inhibitors. Subsequent X-ray structures of the NOSIII and NOSI oxygenase modules confirmed the conserved fold and active sites in the three isoforms.^{10–12} Since then, hundreds of structures of NOSox have been solved with various inhibitors and provided critical insights into enzyme-specific features that can be exploited for rational isozyme-specific inhibitors (reviewed in ^{13,14}).

1.3.2.2. NOS reductase modules

The first X-ray structure of a proteolytic fragment of the NOSI reductase module confirmed an overall fold similar to cytochrome P450 reductase (CYPOR), sulfite reductase and novel reductase 1.¹⁵ The complete structure of the rat NOSI reductase module further contained the missing FMN-binding domain, as well as key regulatory sequence elements.¹⁶ Notably, this structure provided a structural basis for the numerous mechanisms regulating NOSI and NOSIII activity (**Figure 1.1f**). In addition, the authors suggested for the first time that large motions of the FMN domain were required for electron transfer to the heme of the NOSox module.

1.3.2.3. Calmodulin-binding region

The X-ray structure of calmodulin bound to a NOSIII-derived CaM-binding peptide (**Figure 1.1f**) allowed unambiguous identification of key interactions between

NOS and CaM that were distinct from other CaM/peptide complexes.¹⁷ The structure provided several scenarios for the mechanism by which NOS phosphorylation decreases CaM binding in NOSIII. Recent nuclear magnetic resonance (NMR) studies supported two of the proposed mechanisms whereby phosphorylation would (1) destabilize the secondary structure of the NOSIII peptide and (2) decrease CaM binding via electrostatic repulsion. Finally, it implicated specific hydrophobic residues responsible for the apparent Ca^{2+} -independent high affinity of NOSII for CaM, later confirmed by NMR studies of both NOSIII- and NOSII-derived peptides with CaM.¹⁸ The X-ray structure of the NOSII region encompassing the FMN domain and the CaM-binding region in complex with CaM showed the high flexibility of the modular structure¹⁹ that supports the hypothesized large motions of the FMN domain required for electron transfer.¹⁶

1.3.2.4. Holoenzyme structure

In the absence of a high-resolution structure of full-length NOS with and without CaM, two questions remain to be addressed: (1) how do electrons shuttle from FMN to heme? and (2) how does CaM affect NOS activity? Recently, the low-resolution structures of all full-length NOS isozymes were determined by electron microscopy.^{20–22} All studies show that the full-length NOS isozymes display extended architectures and are characterized by remarkable conformational diversity, which likely explains the failure to crystallize them so far. In all structures, the individual modules are rather rigid and linked to each other by regions that display a wide range of conformations. The dimeric NOSox module represents a clear anchor point in all

isozymes. However, the three studies differ regarding the arrangement of other modules present in the NOS enzymes. In particular, Yokom *et al.* and Volkmann *et al.* found the architecture for NOSI and NOSIII to be strikingly symmetrical with the NOSred modules interacting with each other (albeit via different regions in the two studies), while Campbell *et al.* found no such symmetry in all three isozymes regardless of the presence of CaM. The reason for such discrepancy is not clear. Regardless, these studies suggest that NOS presents conformations that range from extended electron-accepting (closed, input state) to folded electron-donating (open, output state) structures present both in the absence and presence of CaM. While CaM does not seem to shift the conformational equilibrium between these different states, CaM binding seems to increase flexibility in the NOSred module to allow the FMN domain to reach the heme in the NOSox module.²³ In addition, these studies all support a model in which electrons are transferred in trans from one NOSred to one NOSox at a time.

1.3.2.5. Regulatory element in NOS isozymes

Several regulatory mechanisms have been described for NOS enzymes, including protein–protein interactions, cellular localization, phosphorylation at various sites, regulatory sequence elements in the NOSred module (C-terminal tail, autoinhibitory helix, and CD2A), and, of course, Ca²⁺/CaM binding (**Figure 1.1b**). NOSIII is (de)phosphorylated on at least five residues, including Ser114, Ser615, Ser633, Ser1177 and Thr495, while NOSI is (de)phosphorylated on three residues Ser741, Ser847, Ser1412 (**Tables 1.1** and **1.2**). In NOSI and NOSIII, a 40–50 amino-

acid autoinhibitory element in the FMN domain inhibits both intra- and interdomain electron transfer. In addition, all isoforms contain a 20–40 amino-acid C-terminal tail that inhibits electron transfer within the reductase module. In NOSI and NOSIII, the C-terminal tail acts in concert with an NADPH-induced lock and isozyme-specific Arg1400.¹⁶ Removal of either inhibitory element increases the electron flow within the reductase module, but $\text{Ca}^{2+}/\text{CaM}$ is still required for NO production. These regulation mechanisms in NOS have recently been reviewed.^{24,25}

Table 1.1. NOSI phosphorylation sites and roles

Residue	Effect on activity and kinase involved	Ref.
Ser741 (rat)	Blocks $\text{Ca}^{2+}/\text{CaM}$ binding CaMKI	26
Ser1412 (rat)	Activating NO synthesis Akt	27
Ser847 (rat)	Blocks $\text{Ca}^{2+}/\text{CaM}$ binding, inhibits NO synthesis CaMKII	28

Table 1.2. NOSIII phosphorylation sites and roles

Residue (human)	Effect on activity and kinase involved	Ref.
Ser1177	Activating electron flow and increased sensitivity to $\text{Ca}^{2+}/\text{CaM}$	29,30
Ser633	Akt, AMPK, CaM kinase2, PKA, Chk1, PKG Activating electron flow and increased sensitivity to $\text{Ca}^{2+}/\text{CaM}$	31,32
Ser615	Activating increased sensitivity to $\text{Ca}^{2+}/\text{CaM}$	31,32
Ser116	Inhibitory	31,33,34
Thr495	Inhibitory; reduced CaM binding PKC, ROCK, AMPK	35
Tyr81 (bovine)	Activating Src kinase	36
Tyr657 (bovine)	Inhibitory PYK	37

1.4. NO Pathways

1.4.1. NOSI and neurotransmission

NOSI is involved in multiple pathways, including neurogenesis, memory formation, and hypertension (**Figure 1.2a**). NOSI uniquely carries an N-terminal PDZ domain, which is commonly used for protein–protein interactions and subcellular localization. One such partner for NOSI is postsynaptic density protein-95 (PSD-95), which tethers NOSI to N-methyl-D-aspartate receptor (NMDAR) at synapses. Activation of NMDAR allows for the influx of calcium and leads to activation of NOSI. Sequential phosphorylations/dephosphorylations of NOSI at activating S1412 and deactivating S847 are regulated by NMDAR and provide tight control of NO production at synapses.²⁸

In addition to its role in controlling neuronal functions, NOSI has also been shown to play a cardioprotective role during CVD-related stress. In CVD, cells controlling blood flow undergo increased oxidative stress, which inhibits NOS activity. H4B and NOS heme cofactors can become oxidized resulting in uncoupling of NOS activity and decreased bioavailability of NO. While NOSIII is traditionally linked to its cardioprotective role in the endothelium, multiple groups have reported decreased NOSIII activity in CVD and increased NOSI expression and activity. Identification of downstream targets of NOSI during CVD-related stress will provide new targets for drug development.³⁸

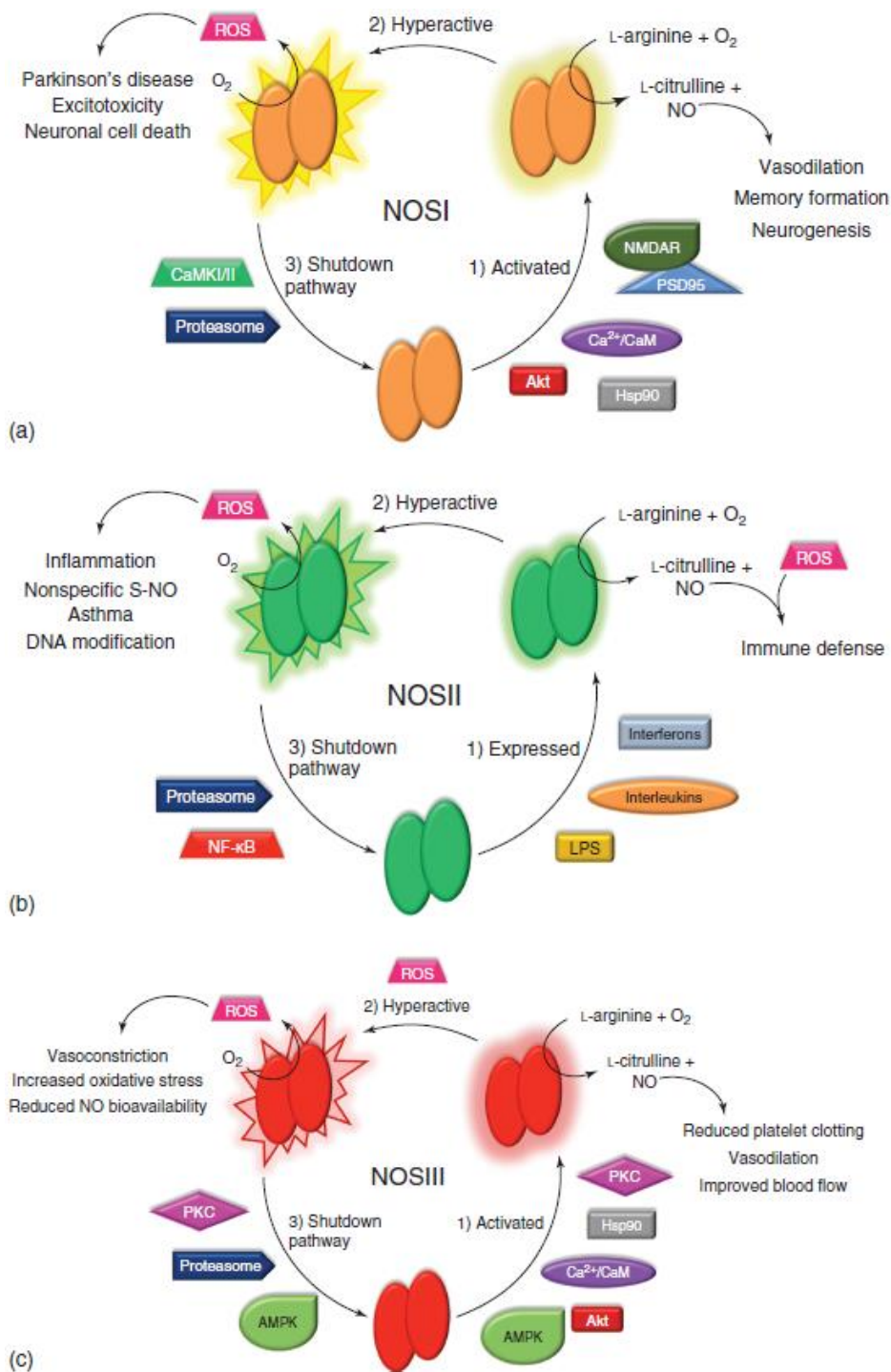


Figure 1.2. Overall NOS pathways and regulation. (a) NOSI becomes activated with increased Ca^{2+} concentrations, phosphorylation and protein–protein interactions. NOSI-derived NO improves blood flow and increases neuronal cell growth (1). Hyperactivated NOSI can lead to excitotoxicity and apoptosis (2). NOSI activity is shutdown through phosphorylation and proteasomal degradation (3). (b) NOSII expression is induced by various cytokines. Immune cells such as macrophages and

neutrophils use NOSII to generate cytotoxic levels of NO to kill invading pathogens (1). Excessive NOSII activity can damage healthy cells leading to inflammation and cell death (2). NOSII is neutralised through proteasomal degradation and a negative feedback loop with NF- κ B (3). (c) NOSIII is activated similarly to NOSI. A variety of kinases, protein–protein interactions and increased Ca^{2+} levels enhance NOSIII activity. NOSIII-derived NO inhibits platelet aggregation and dilates neighbouring blood vessels (1). Reactive oxygen species (ROS) and low BH4 levels can uncouple NOSIII activity and lead to superoxide formation, which in turn decreases available NO and exacerbates oxidative stress (2). Phosphorylation and proteasomal degradation turn this pathway off (3).

1.4.2. NOSII and high NO levels

NOSII is the only NOS isoform that is usually not constitutively expressed. Its induction is dependent on cytokines, bacterial lipopolysaccharides and other agents. These agents recruit transcription factors at the NOSII gene promoter to initiate transcription. Once NOSII is expressed in neutrophils and macrophages, cytotoxic levels of NO are produced to target invading pathogens (**Figure 1.2b**). Interestingly, the NO levels produced in response to cytokines are much lower than those produced in response to bacterial or viral products, thus differentially regulating whether the response will be cytotoxic or immunoregulatory. Mechanisms for NO-dependent cell death include nonspecific protein S-nitrosylation, reaction with superoxide to form peroxynitrite that will lead to protein nitration, high reactivity with metal- and iron-containing proteins, and deoxyribonucleic acid (DNA) mutation via deamination and modification of lipids. The high NO levels produced by NOSII can be lethal for bacteria, virus and tumor cells, but also to healthy cells, leading to a number of pathologies.³⁹ For example, excessive NOSII expression and activity in the human airway epithelium has been linked to asthma.⁴⁰

The role of NOSII in cancer is complex, as both pro- and anti-cancer functions have been proposed for NOSII, depending on the tumor microenvironment and other

factors, including the intrinsic chemical properties of NO. As the cell redox environment affects how NO will react with surrounding macromolecules, it has been proposed that the concentration of NO as well as its interactions with cellular targets can vary dramatically depending on the type of cancer (reviewed in ⁴¹).

1.4.3. NOSIII and vasodilation

NOSIII is the only NOS isozyme that undergoes N-terminal myristoylation and palmitoylation, which mediate its association to the plasma membrane in specialized compartments called caveolae. Various agonists, like bradykinin and shear stress, mediate NOSIII translocation from the caveolae to the cytoplasm (**Figure 1.2c**). In the caveolae, NOSIII interacts with caveolin, which inhibits its activity. Influx of Ca^{2+} and subsequent Ca^{2+} /CaM binding to NOSIII relieves this inhibitory interaction, leading to translocation of NOSIII to the cytoplasm and activation of the enzyme.⁴² In addition to Ca^{2+} /CaM and other known mechanisms (see **section 1.3.2.5**), NOSIII is heavily posttranslationally modified: acylation, acetylation, nitrosation, phosphorylation, glycosylation and glutathionylation have all been reported to finely tune NOSIII activity (reviewed in ⁴³).

In the vasculature, NOSIII is the primary source of NO responsible for vasodilation and inhibition of platelet aggregation in blood vessels. To do this, NOSIII relies on guanylyl cyclase 1 (GC1) in neighboring smooth muscle cells (**Figure 1.3**). GC1 converts guanosine-5'-triphosphate (GTP) into 3',5'-cyclic guanosine monophosphate (cGMP). The second messenger cGMP then targets cGMP-dependent kinase (PKG), which has a myriad of downstream targets including vasodilator-stimulated phospho- protein, myosin-light-chain phosphatase and

phosphodiesterase 5 (PDE5), a known inhibitor of this pathway that limits cGMP bioavailability.

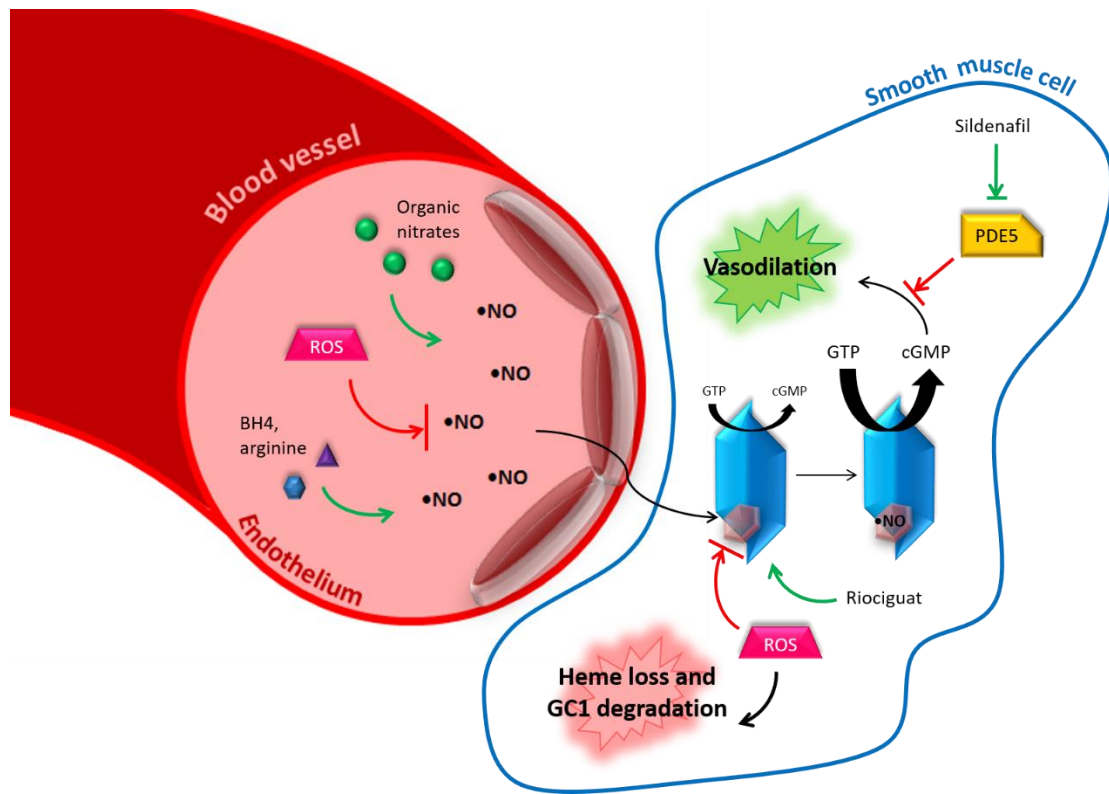


Figure 1.3. The NO–GC1–cGMP pathway and therapeutic targets. NO is generated in the endothelium and diffuses to smooth muscle cells. GC1 (blue) is the primary target for NO binding, which triggers an increase in cGMP generation. Second messenger cGMP activates PKG, which phosphorylates downstream targets for improved blood flow. Reactive oxygen species (ROS) and phosphodiesterase-5 (PDE5) can inhibit this pathway (red arrows). Several pharmacological targets for this pathway are shown with green arrows.

NO binding to the reduced heme in the GC1 sensor domain induces a several hundred-fold increase in GC1 activity. How this signal is transduced from the NO-binding N-terminus to the catalytic site at the C-terminus remains unknown. High-resolution structures of individual GC1 domains or bacterial homologues have been solved. However, a high-resolution structure of full-length GC1 remains elusive, most likely due to high flexibility of its domains. Small-angle X-ray scattering, cross-

linking, hydrogen-deuterium exchange mass spectrometry and electron microscopy studies have provided a low-resolution picture of the overall architecture of GC1 (reviewed in ⁴⁴). These studies suggest that GC1 may undergo a wide range of conformations, but that NO activation may only require small structural rearrangements. More research is needed to understand the activation mechanism of NO and provide a basis for the rational design of GC1 activators.

Recently, a third mechanism of action has been discovered for NO that is distinct from GC1 activation and protein modification: epigenetic regulation. NO has been shown to directly or indirectly mediate histone modifications (via modifications of histone-modifying enzymes), to be involved in DNA methylation (unknown mechanism) and to affect micro-ribonucleic acid (RNA) levels.⁴⁵ This would imply that the effects of NO could be further carried over via epigenetic modifications.

1.5. Bacterial NO

An abundance of research has identified NOS-like activity in different bacterial strains, leading many to wonder how bacteria and mammals compare in terms of NO synthesis. Early attempts to identify prokaryotic NOS homologues were confounded by the fact that bacteria can generate NO via several pathways ways, some of them completely independent of NOS-like activity. The first NOS-like bacterial enzymes were identified in gram-positive bacteria (*Bacillus*, *Deinococcus*), but have since been found in gram-negative bacteria, cyanobacteria and archaea as well. Structures of bacterial NOS resemble closely that of the mammalian NOS α module, except for the N-terminal hook and zinc-binding site that participate in H4B

binding in mammalian NOS. In addition, bacterial NOS bind not only H4B but also H4F, and the exact identity of the cofactor remains unknown. Similarly to mammalian NOS, bacterial NOS also require a heme cofactor to bind and activate oxygen to oxidize L-arginine to produce L-citrulline and NO via a NOHA intermediate. Activity can be increased in the presence of cofactors such as NADPH, FAD, FMN and H4B and can be abolished by known mammalian NOS inhibitors. However, there are several differences between the two kingdoms that should be noted. For example, many bacteria rely on a surrogate electron-donating NOSred-like protein that is not covalently attached to the NOSox protein. Finally, the rate of NO release in bacterial NOS is slower than that of mammalian NOS, which suggests that the end product in bacteria may not be NO but further oxidized NO_x species (reviewed in ⁴⁶).

In bacteria, the biological roles played by NO are just as diverse as in mammals, including Trp-nitrosylation for the production of toxins, tRNA-Trp charging, recovery from UV damage and protection against oxidative damage. Many bacteria also use Heme Nitric Oxide (HNOX) proteins to initiate two-component systems, which use transphosphorylation between sensor and effector proteins to carry out sophisticated signaling. Allowing HNOX proteins to sense NO, among other gaseous molecules, allows for the cell to sense its microenvironment and adjust accordingly via transcriptional control, biofilm formation and quorum sensing.

1.6. Nitrite/Nitrate and NO

It is now recognized that NO production in the human body does not rely solely on NOS activity, but can also result from cellular processes utilizing nitrate, nitrite, and other nitrogen intermediates.^{47,48} These latter processes closely resemble the nitrogen cycle. Nitrate is obtained by oxidation of NO that was produced by NOS and through dietary consumption of leafy greens. Bacteria in the oral cavity play a crucial role in the bioavailability of nitrite via reduction of nitrate. Nitrite can also be obtained via consumption of cured meats. Nitrite can be converted into NO by a number of enzymes in blood and tissues, including xanthine oxidase, deoxymyoglobin, deoxyhaemoglobin, cytochrome P450, carbonic anhydrase and aldehyde oxidase. These reactions are increased in hypoxic and low pH conditions, whereas NOS function is decreased in these same conditions (**Figure 1.4**). As a result, this alternative NO-producing pathway is now seen as an important pool of NO. Nitrate and nitrite have been shown to exert cardioprotective and anti-inflammatory effects, thus reverting the old belief that nitrate is toxic to humans. More studies will be needed to determine whether increasing daily nitrate intake is harmful or not to humans.

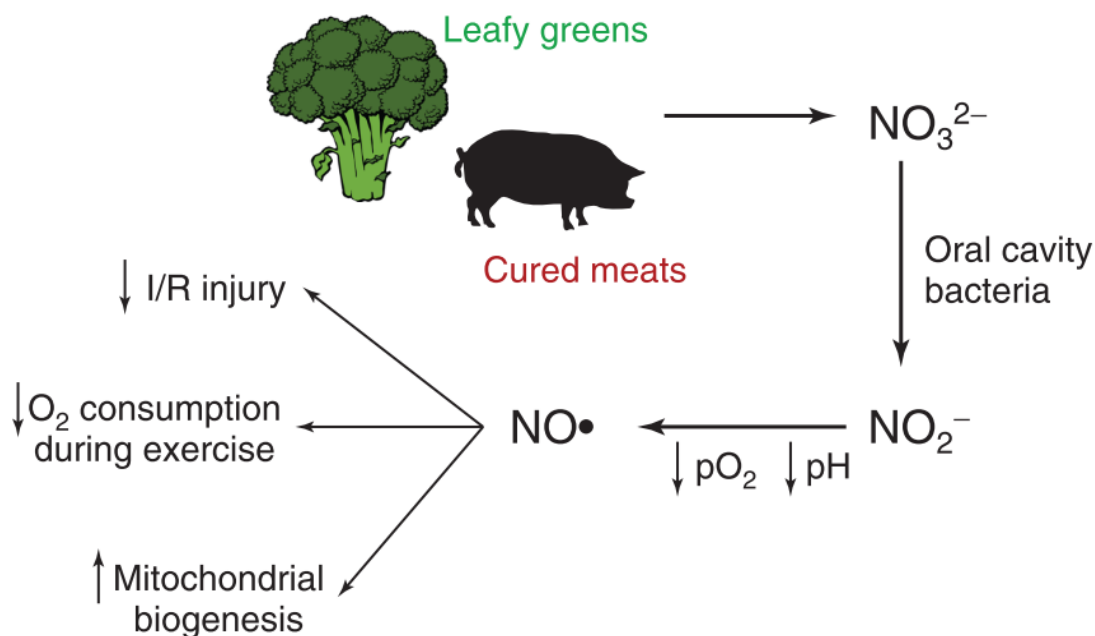


Figure 1.4. The nitrate/nitrite/NO pathway. Nitrate is obtained primarily in the diet from leafy greens and cured meats. Oral bacteria oxidise nitrate to nitrite, which acts as an important source of NO under hypoxic and acidic conditions.

1.7. Cardiovascular diseases and treatments

CVD is currently the leading cause of death in the world. Alterations in the NO–GC1–cGMP pathway signaling have been linked to CVD. Elevated ROS levels, decreased NOS expression, and decreased levels of NOS substrate (L-Arg) or cofactors (BH₄, NADPH) all decrease NO bioavailability, which affects downstream pathways leading to vasoconstriction, inflammation and increased platelet clotting. In addition, oxidation of the GC1 heme cofactor reduces cGMP levels, also affecting the NO–GC1–cGMP signaling pathway (**Figure 1.3**). While causes of CVD can vary, common denominators include a sedentary lifestyle, poor diet, age and family history. Attempts to target the NO–GC1–cGMP pathway focus on four main areas (reviewed in ⁴⁹):

1. *Increase NO bioavailability with NO donors.* Organic nitrates have been used for over a century to alleviate angina pectoris, a common symptom for atherosclerosis. While this method can relieve acute chest pains, a hallmark of nitroglycerin treatment is NO tolerance requiring increased dosage for the desired effect, thus limiting long-term usage. Other types of NO donors have been developed to overcome these limitations, including inhaled NO, NO-nonsteroidal anti-inflammatory drugs (NO-NSAIDs), inorganic nitrite and nitrate. Most of these are currently under evaluation for therapeutic uses.
2. *Increase NOS activity.* Supplementation of NOS substrate and cofactors has been explored to treat CVD. Methods include additional BH4 and arginine. However, several complications limit their use. An increased oxidative environment in CVD has been attributed to the oxidation of BH4 to BH2 and subsequent uncoupling of NOSIII. This leads to the increased generation of ROS and enhancement of oxidative damage. Supplementation of BH4 is limited in this respect. There are varying degrees of clinical success regarding arginine as a treatment for CVD. This has been attributed to several reasons including arginases that breakdown arginine and its requirement for general protein synthesis. In addition, the use of any cofactor or substrate to improve NOSIII activity in CVD is limited due to their use by all three NOS isoforms
3. *Decrease cGMP degradation by PDE5.* Sildenafil is a PDE5 inhibitor that only shows modest effects on reducing blood pressure. However, it was shown to potentiate the effects of NO. This drug has shown promise in

patients with pulmonary arterial hypertension (PAH), when the NO–GC1–cGMP pathway is stimulated as well.

4. *Stimulate cGMP production by GC1.* In 2013, the FDA approved the first drug that directly targets the NO–GC1–cGMP pathway for the treatment of PH. Riociguat (Adempas) is a GC1 stimulator that enhances GC1's response to NO and stimulates activity independently of NO.⁵⁰ While clinical data support its use to treat PH, hypotensive side effects have been reported. Patients prescribed with riociguat must be dosed three times per day, cannot be pregnant and cannot be on any blood thinning medications. As a result, more research is necessary to find other GC1 activators and stimulators for use as therapeutic agents.

1.8. Summary

NO plays a key role in the cardiovascular and neuronal system and in the immune response. Several pathways regulate NO bioavailability and downstream effects and are the target for therapeutic interventions. Dysfunction in NO signaling has been linked to a variety of diseases, most notably CVD. While considerable progress has been made in understanding the mechanism of action of NO, many questions remain: (1) the catalytic mechanism of NOS has not been fully elucidated as many proposed intermediate species remain to be identified experimentally. (2) What is the exact role of NO in bacteria and what is their mechanism for NO production? (3) What is the mechanism of allosteric NO activation of guanylyl cyclase? This information will be crucial for the design of novel therapeutic agents in

the treatment of CVDs. (4) How are the various mechanisms regulating NOS function orchestrated in cells and how do they affect health and disease? There is no doubt that answers to these questions will be provided in the years to come.

Chapter 2: Structure/Function of the Soluble Guanylyl Cyclase Catalytic Domain

Reproduced with permission from Kenneth C. Childers and Elsa D. Garcin. "Structure/Function of the Soluble Guanylyl Cyclase Catalytic Domain." Nitric Oxide, 77, doi: 10.1016/j.niox.2018.04.008 Copyright 2018 Elsevier

2.1. Abstract

Soluble guanylyl cyclase (GC-1) is the primary receptor of nitric oxide (NO) in smooth muscle cells and maintains vascular function by inducing vasorelaxation in nearby blood vessels. GC-1 converts guanosine 5'-triphosphate (GTP) into cyclic guanosine 3',5'-monophosphate (cGMP), which acts as a second messenger to improve blood flow. While much work has been done to characterize this pathway, we lack a mechanistic understanding of how NO binding to the heme domain leads to a large increase in activity at the C-terminal catalytic domain. Recent structural evidence and activity measurements from multiple groups have revealed a low-activity cyclase domain that requires additional GC-1 domains to promote a catalytically-competent conformation. How the catalytic domain structurally transitions into the active conformation requires further characterization. This review focuses on structure/function studies of the GC-1 catalytic domain and recent advances various groups have made in understanding how catalytic activity is regulated including small molecules interactions, Cys-S-NO modifications and potential interactions with the NO-sensor domain and other proteins.

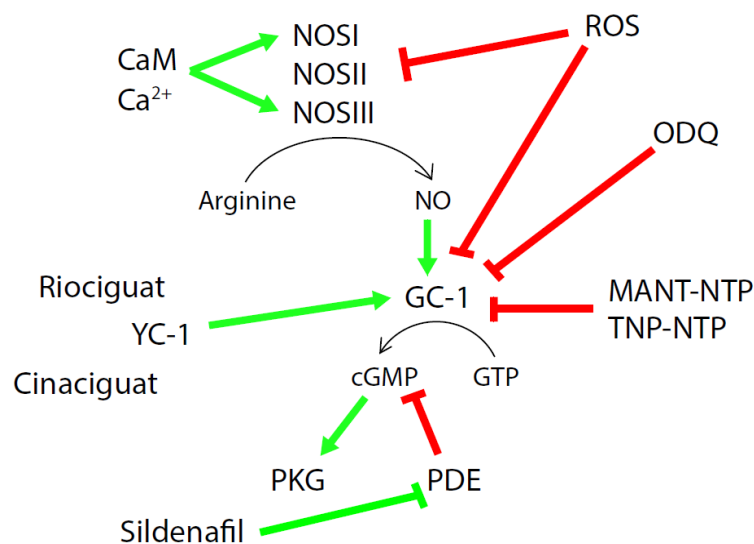


Figure 2.1. Overview of the NO/GC-1/cGMP pathway. The NO/GC-1/cGMP pathway mediates vasodilation and vasoconstriction and is regulated by a variety of inhibitors and activators. Green arrows indicate pathway activation/stimulation and red arrows indicate pathway inhibition. Abbreviations- CaM: calmodulin. NOSI/II/III: nitric oxide synthase-isoforms 1, 2, and 3. GC-1: soluble guanylyl cyclase. GTP: guanosine 5'-triphosphate. cGMP: cyclic guanosine 3',5'-monophosphate. PKG: protein kinase G. PDE: phosphodiesterase. ROS: reactive oxygen species. ODQ: 1H-(1,2,4)oxadiazolo(4,3-a)quinoxaline-1-one. MANT-NTP: 2',3'-O-(N-methylanthraniloyl) nucleotide 5'-triphosphate. TNP-NTP: 2',3'-O-(2,4,6-trinitrophenyl) nucleotide 5'-triphosphate.

2.2. Introduction

Soluble guanylyl cyclase (GC-1) maintains vascular function through the NO/GC-1/cGMP pathway^{44,51} by catalyzing the conversion of GTP into cGMP (**Figure 2.1**). The GC-1 heme prosthetic group binds NO with picomolar affinity, resulting in a 100- to 200-fold increase in catalytic activity. cGMP activates protein kinase G, which phosphorylates a myriad of targets to induce, among other effects, vasodilation and inhibition of platelet aggregation and adhesion to the arterial wall. Dysfunction in the NO/GC-1/cGMP pathway through reactive oxygen species (ROS) has been linked to a variety of vascular diseases.^{49,52} ROS can disrupt this pathway by reacting with free NO, thus reducing NO bioavailability, or oxidizing the ferrous

heme group in GC-1, causing it to lose its sensitivity toward NO. GC-1 has a significantly lower affinity for oxidized heme.⁵³ Once the heme is lost, apo-GC-1 is targeted for degradation.⁵⁴

Cardiovascular diseases are responsible for the highest mortality rate globally with approximately 1 in 3 deaths being attributed to a cardio-related illness. The role of GC-1 in maintaining vascular health makes it an ideal target to improve cardiovascular function. Pharmaceuticals that elevate GC-1 activity are classified as either heme-dependent (stimulators) or heme-independent (activators; reviewed in ⁵⁵). In 2013, riociguat became the first FDA-approved stimulator to target GC-1 for the treatment of pulmonary arterial hypertension and chronic thromboembolic pulmonary hypertension (CTEPH). Clinical trials in CTEPH patients showed treatment with riociguat improved 6-min walking distances and reduced pulmonary blood pressure over the placebo group.⁵⁶ Cinaciguat and ataciguat are known GC-1 activators. Structural evidence using a bacterial homolog of the NO-sensor domain with bound cinaciguat suggested the activator rescues GC-1 activity under oxidative stress by occupying the empty heme pocket and making key interactions with nearby residues while mimicking the NO-severed His ligand.⁵⁷ This hypothesis was supported by studies showing that cinaciguat improved cGMP production in endothelial cells after oxidative damage.⁵⁴ Further clinical trials with cinaciguat found hypotensive side-effects when treating patients for acute heart failure⁵⁸ and were ceased by the FDA in 2011. Treatment of rat aortic smooth muscle cells with ataciguat under oxidative stress improved basal and NO-stimulated GC-1 activity.⁵⁹ Ongoing clinical trials are using ataciguat as a treatment for aortic stenosis due to calcification. More recently,

studies using the biotinylated IWP-854 GC-1 stimulator helped to identify a conserved binding site for other GC-1 stimulators in the β HNOX NO-sensor domain.⁶⁰ Elucidating this binding region could provide the foundation for a class of novel GC-1 stimulators.

A dysfunctional NO/GC-1/cGMP pathway has been implicated in other vasculature disorders. Glaucoma is a leading cause of blindness in the United States with approximately 2 million people afflicted and is characterized by increased intraocular pressure (IOP) and damage to the optic nerve. Primary open-angle glaucoma (POAG) is a subtype of glaucoma and has no known underlying etiology. Treatment for POAG manages symptoms through beta-blockers to reduce aqueous humor inflow and eye surgery to relieve IOP.⁶¹ Multiple groups have identified a dysfunctional NO/GC-1/cGMP pathway as an alternate target for POAG treatment (reviewed in ⁵²). NO-donors and cGMP have been used in POAG animal studies to lower IOP.^{62,63} Older mice lacking the α GC-1 polypeptide had typical POAG symptoms including reduced aqueous humor outflow, increased IOP, and damage to the optic nerve,⁶⁴ directly implicating GC-1 in the disease. More recently, treatment of mouse eyes with elevated IOP and reduced aqueous humor outflow using a novel GC-1 stimulator improved ocular flow rate over the vehicle-treated group; similar results were observed using an NO-donor.⁶⁵ Targeting the NO/GC-1/cGMP pathway for improved optic blood flow may prove useful in the treatment of POAG.

Renal disease is characterized by aberrant fibrotic remodeling of renal tissue, elevated apoptosis in kidney tissue, and eventual organ failure. In addition, patients with renal disease are more likely to suffer from systemic hypertension due to

oxidative damage (reviewed in ⁶⁶). Treatment of rats with progressive renal fibrosis using GC-1 stimulator BAY 41-2272 elevated cGMP levels and reduced kidney fibrosis and systemic blood pressure.⁶⁷ Rat models of renal disease induced by a high-salt diet were given cinaciguat. After 21 weeks, increased cGMP levels were measured and renal function was improved over the placebo group.⁶⁸ NO supplementation has also been used to improve renal function. After 1 week of supplemented dietary arginine, the substrate for NO synthesis, increased cGMP levels were measured in urine, improved renal function and reduced renal fibrosis and apoptosis.⁶⁹

Because of the systemic role GC-1 has in vasculature-related illnesses and the fact that there is only one FDA-approved drug that targets GC-1, a complete understanding of how NO stimulates GC-1 activity is crucial. In this review, we provide a comprehensive overview of the GC-1 catalytic domain. We also discuss recent implications for Cys-S-NO modifications in the catalytic domain regulating GC-1 activity and interactions with the NO-sensor domain.

2.3. GC-1 domain architecture

GC-1 is a 150 kDa heterodimer and its $\alpha_1\beta_1$ isoform is found ubiquitously. While another isoform of the enzyme does exist (GC-2; $\alpha_2\beta_1$),⁷⁰ this review will focus on the predominant $\alpha_1\beta_1$ isoform. Each α/β polypeptide contains four domains from N- to C-terminus connected by short linkers: NO-sensor domain, PAS domain, coiled-coil domain, and catalytic domain (**Figure 2.2**). The N-terminal NO-sensor domain is predicted to adopt a structure similar to bacterial heme nitric oxide-oxygen binding (HNOX) proteins (**Figure 2.2**). These proteins are typically standalone

proteins and use a heme cofactor to sense gaseous ligands and activate response proteins to elicit the desired effect, usually through gene regulation.⁷¹ While α HNOX and β HNOX domains are predicted to share a similar HNOX-like fold, only the β HNOX domain of GC-1 carries a heme prosthetic group that binds NO; the role of α HNOX remains to be determined, however recent work suggests it regulates GC-1 activity by lowering the affinity of β HNOX for CO and NO.⁷² β HNOX uses a His ligand to bind the heme cofactor in its reduced Fe^{2+} redox state. NO binding to the distal heme side severs the His-iron bond, which is thought to play a crucial role in NO-induced stimulation of GC-1.^{73,74} In addition, several groups have found that excess NO is required to fully activate GC-1.^{75,76} The proximal side of the heme^{76,77} or Cys residues^{78,79} have been suggested as potential binding sites for the extra NO. However, recent spectroscopic data in *Shewanella oneidensis* HNOX shows that the distal site is preferred, thus questioning the biological significance of proximal heme-NO binding.⁸⁰

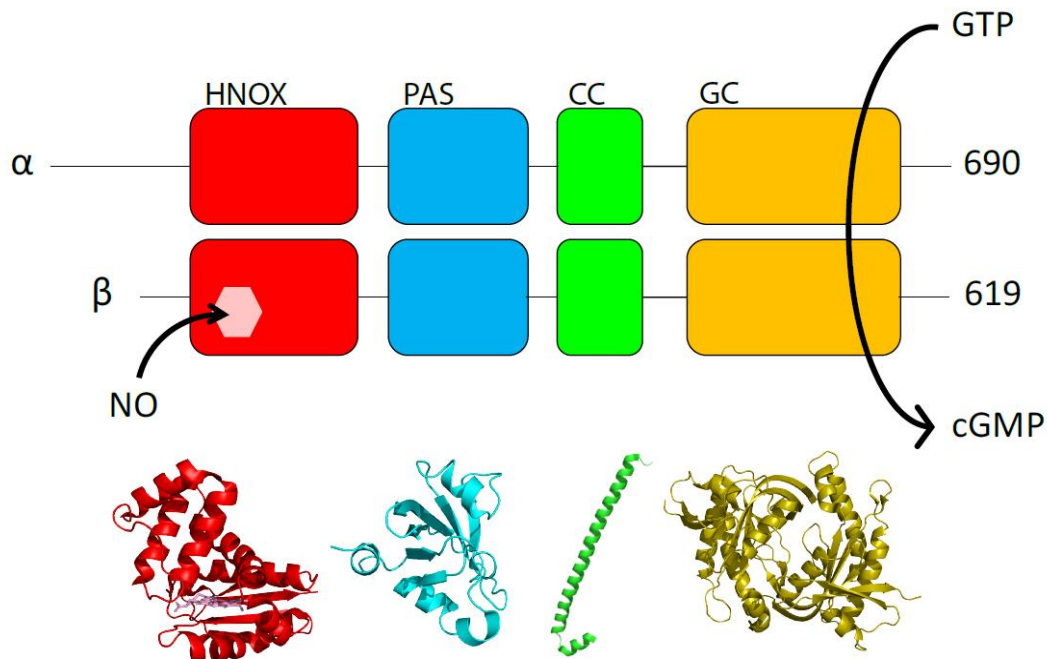


Figure 2.2. GC-1 is a multi-domain enzyme. General domain architecture of GC-1 (top) and crystal structures of homologous or wild-type GC-1 domains (below). HNOX: Heme Nitric oxide-OXYgen binding (PDB code 2O09, red, *Nostoc* PCC 7120 HNOX). PAS: Per-Arnt-Sim (PDB code 4GJ4, cyan, *Manduca sexta* GC-1). CC: Coiled-Coil (PDB code 3HLS, green, *Rattus norvegicus* β GC-1). GC: Guanylyl Cyclase (PDB code 4NI2, gold, *Homo sapiens* $\alpha\beta$ GC-1). Numbering for the α and β chains is from *Homo sapiens* GC-1.

The subsequent domain belongs to the Per-Arnt-Sim (PAS) family of proteins, typically used to transduce signals to effector domains through subtle conformational shifts. While some PAS domains use cofactors for signal transduction, the PAS domain in GC-1 has none. Crystal structures of a bacterial homolog⁸¹ and of the GC-1 α PAS domain⁸² have been solved and show the predicted fold consisting of six β -sheets surrounded by several short α helices (**Figure 2.2**). The GC-1 PAS domain has been suggested to play a key role in GC-1 dimerization.⁸¹ More recently, the PAS domain was shown to interact with heat-shock protein 90 and mediate heme insertion in the β HNOX domain.⁸³

Crystallographic studies showed that the coiled-coil (CC) domain folds as long α -helices (**Figure 2.2**) in an antiparallel orientation.⁸⁴ However cross-linking studies later demonstrated that the heterodimeric CC assembles in a parallel orientation.⁸⁵ The CC domain has been shown to play a key role in GC-1 heterodimerization,⁸⁶ and to act as a scaffold for other GC-1 domains.^{85,87}

The C-terminal catalytic domain ($\alpha\beta\text{GC}^{\text{cat}}$) contains the substrate-binding pocket located at the interface of the α and β subunits, which both contribute key residues for GTP binding (**Figure 2.2**). Several structures of apo inactive cyclase domains from bacteria, algae, fungus, and human have been solved, but a structure of the holo active form remains elusive.^{88–92} Several groups have reported a high propensity for $\beta\beta\text{GC}^{\text{cat}}$ homodimers to form both in solution and during crystallization attempts.^{90,91} Despite these structural characterizations, several key questions remain about the $\alpha\beta\text{GC}^{\text{cat}}$ domain: what is the mechanism by which $\alpha\beta\text{GC}^{\text{cat}}$ transitions from the inactive apo conformation to the catalytically-active conformation upon NO binding? What are the residues involved in the transition from inactive to active $\alpha\beta\text{GC}^{\text{cat}}$? How is the NO-activating signal transduced from the N-terminal NO-sensor domain to the C-terminal catalytic domain? Answering these questions will aid in the design of novel therapeutics that target GC-1 and promote NO-sensitization and cGMP generation.

2.4. Structural studies of the cyclase catalytic domains

2.4.1. The homologous adenylyl cyclase enzyme

Much of what we know about the $\alpha\beta\text{GC}^{\text{cat}}$ domain structure comes from studies of the homologous adenylyl cyclase (AC) catalytic domain. AC converts ATP

into cAMP and is composed of two membrane-bound helical domains and two cytosolic catalytic domains, termed C1 and C2. Sequence alignment identifies C1 as the $\alpha\text{GC}^{\text{cat}}$ counterpart and C2 as the $\beta\text{GC}^{\text{cat}}$ counterpart with ~30% sequence identity for both alignments. Much like the $\alpha\beta\text{GC}^{\text{cat}}$ domain, C1 and C2 must come together to form the ATP- binding cleft. AC maintains a low cAMP turnover rate, but two known stimulators increase its activity. G_{sa} , a subunit of the G-protein coupled receptor, increases AC activity 5-fold and forskolin, a small diterpene molecule isolated from the plant *C. forskohlii*, increases AC activity 9-fold.⁹³ The x-ray structure of an inactive C2/C2 homodimer was solved (**Figure 2.3a**) and showed forskolin bound to each monomer in a well-characterized hydrophobic pocket at the dimer interface.⁹⁴ Based on these results, it was hypothesized that forskolin activates AC via favorable burying of hydrophobic regions to stabilize the C1/C2 heterodimer. The structure of the C1/ C2 heterodimer was solved in the closed conformation (**Figure 2.3b**) with bound activators G_{sa} and forskolin, and a non-cyclizable ATP substrate.⁹⁵ This structure confirmed the identity of the residues important for catalysis and nucleobase specificity (**Table 2.1**). Binding of G_{sa} via insertion of its switch II helix into a groove of the C2 subunit is thought to reorient catalytic residues in the C1/C2 heterodimer into a competent conformation and bury additional exposed hydrophobic regions near the membrane. C1/C2 conformational changes also include a 7° rigid-body rotation of C1 around C2 and closure of the ATP-binding pocket. While there is no known allosteric activator for GC-1 that binds in the $\alpha\beta\text{GC}^{\text{cat}}$ domain, similar conformational transitions are predicted for its catalytic domain (see **sections 2.4.3 – 2.4.5**).

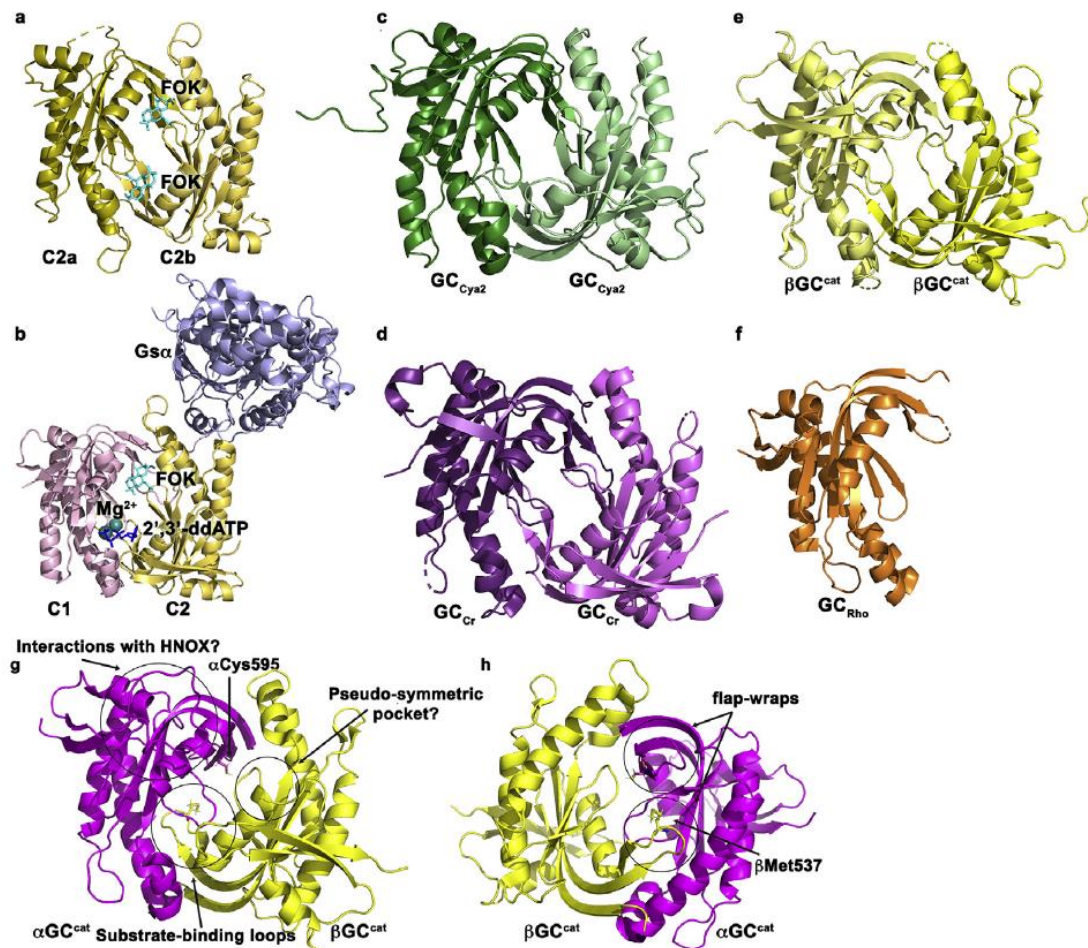


Figure 2.3. Structural overview of adenylyl and guanylyl cyclases. (a) C2/C2 homodimer (C2a, dark/C2b, light yellow) with two forskolin molecules (FOK, cyan) at the dimer interface (PDB code 1AB8). (b) C1/C2 heterodimer (light red/light yellow, respectively) with bound activators Gs α (light blue) and forskolin (FOK, cyan); substrate 2',3'-dideoxyadenosine 5'-triphosphate (2',3'-ddATP, dark blue) and two Mg²⁺ ions (green, PDB code 1CJU). (c) *Synechocystis* PCC 6803 Cya2 GC (GC_{Cya2}) homodimer (green, PDB code 2W01). (d) *Chlamydomonas reinhardtii* CYG12 GC (GC_{Cr}) homodimer (purple, PDB code 3ET6). (e) Human $\beta\beta$ GCcat homodimer (dark/ light yellow, PDB code 2WZ1). (f) *Blastocladia emersonii* RhoGC cyclase (GC_{Rho}) monomer (PDB code 6AO9). (g, h) Wild-type *Homo sapiens* $\alpha\beta$ GCcat heterodimer (α GCcat magenta, β GCcat yellow) and putative regions for domain activation (PDB code 4NI2) viewed on the ventral (g) and dorsal (h) side.

There exist nine isoforms of the membrane-bound AC and each have discrete physiological functions.⁹⁶ Because each isoform utilizes a conserved C1/C2 catalytic domain to cyclize ATP,⁹⁷ there is a need for isoform-specific activators and inhibitors. Derivatives of forskolin have been screened using computational docking

to find stimulators of isoform AC-VI,⁹⁸ which is thought to play a beneficial role in cardiac function. These forskolin-analogs are predicted to bind in the forskolin-binding pocket and make extended interactions outside of the conserved binding site for isoform-specificity.⁹⁹ Others have shown that adenine-based small molecules can promiscuously bind to and inhibit multiple AC isoforms.¹⁰⁰ Inhibitors utilizing a hydrophobic moiety bound to the 2',3'-positions of the NTP ribose have recently been shown to bind with nanomolar affinity at the substrate-binding groove, albeit non-isoform specifically (see **section 2.5.4**).

Table 2.1. Key catalytic residues in adenylyl cyclase and guanylyl cyclases

	Metal (1)	Base (2)	Metal (3)	Phosphate (4)	Base (5)	Ribose (6)	Phosphate (7)	Phosphate (8)
AC-V C1**	Asp396	(Lys436)	Asp440	Arg585	(Asp505)	-	-	-
AC-II C2	-	Lys938		-	Asp1018	Asn1025	Arg1029	Lys1065
α GC	Asp486	(Glu526)	Asp530	Arg574	(Cys595)	-	-	-
β GC	-	Glu473	(Asp477)	-	Cys541	Asn548	Arg552	Lys593
GC _{Cr}	Asp482	Glu520	Asp525	Arg571	Cys592	Asn599	Arg603	Lys540
GC _{Rho}	Asp457	Glu497	Asp501	Arg545	Cys566	Asn573	Arg577	Lys612
GC _{Cya2}	Asp448	Glu488	Asp492	Arg450*	Gly562	Asn569	Arg573	Lys608

AC-V C1: C1 domain of *Canis lupus familiaris* adenylyl cyclase V; AC-II C2: C2 domain of *Rattus norvegicus* adenylyl cyclase II; α GC and β GC: catalytic subunits of *Homo sapiens* GC-1; GC_{Cr}: *C. reinhardtii* CYG12 catalytic domain; GC_{Rho}: *Blastocladiella emersonii* RhoGC catalytic domain; GC_{Cya2}: *Synechocystis* PCC 6803 Cya2 cyclase; Residues in parenthesis do not participate in the active site but are part of the pseudo-symmetric site in adenylyl cyclase, and have been shown to be important for activity in GC-1.¹⁰¹ Numbers (1)–(8) refer to amino acids highlighted in **Figure 2.4**. * Arg450 in GC_{Cya2} is structurally equivalent to Arg574 in α GC. ** The

AC-V sequence used here and in literature is shifted by -81 in comparison with the reported sequence in Uniprot. The sequence numbers reported here match those reported in literature.

2.4.2. Bacterial guanylyl cyclase

Rauch *et al.* solved the first structure of a prokaryotic guanylyl cyclase domain from the cyanobacterium *Synechocystis PCC 6803*.⁸⁸ This protein contains an N-terminal extracellular sensory CHASE2 domain linked to a C-terminal cyclase Cya2 catalytic domain (GC_{cya2}) via transmembrane segments¹⁰². The cyclase domain shares 27.7% and 23.9% sequence identity with human β GC^{cat} and α GC^{cat}, respectively (**Figure 2.4**). The protein homodimerizes and contains a Glu-Gly residue pair for nucleobase specificity that sets it apart from its mammalian guanylyl cyclase (Glu-Cys/Ser pair) and adenylyl cyclase (Lys-Asp/Thr pair) counterparts (**Table 2.1**). The authors showed that Cya2 has a strong preference and specificity for GTP over ATP, allowing for its classification as the first bacterial guanylyl cyclase. Homodimer formation of Cya2 is strongly dependent on ionic strength, with a K_D of 8 μ M for dimer formation. The structure of the Cya2 homodimer confirms a conserved overall fold with class III adenylyl cyclase, despite limited sequence identity (**Figure 2.3c**). Residues from both subunits contribute to formation of the active site(s) at the dimer interface. While two active sites are present in the symmetrical dimer, mutagenesis and activity assays show that a single active site is sufficient. In addition, these studies suggest that the unusual Glu-Gly pair exquisitely modulates the increased GTP specificity of Cya2 over ATP. While the Glu residue plays a major role in selectivity of the base via hydrogen bonding assisted by a supporting Lys residue, the role of the Gly residue may be to provide steric selectivity in concert with a Tyr

residue, instead of a role in hydrogen bonding as is observed in AC and possibly other GCs.

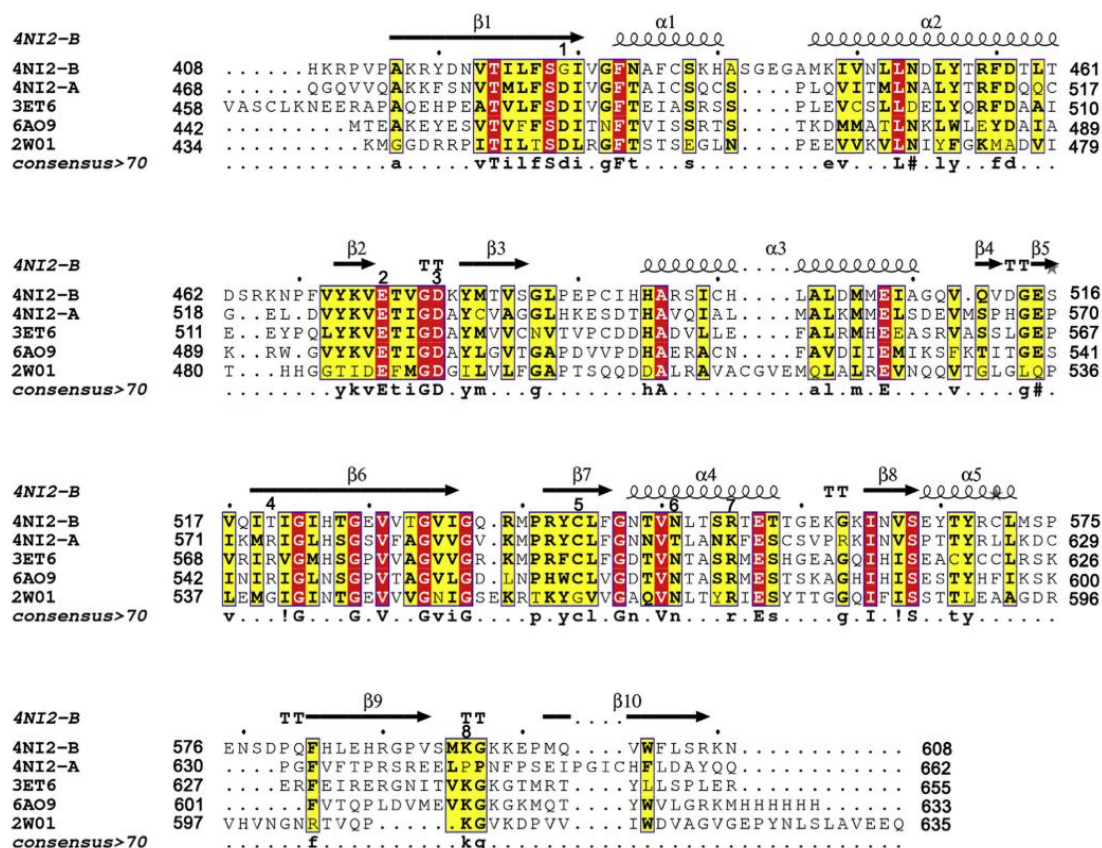


Figure 2.4. Alignment of amino acid sequences of cyclase domains. The multi sequence alignment of guanylyl cyclase domains with available x-ray structures was performed with CLUSTAL Omega and displayed using ESript [113,114]. The sequences used are *Homo sapiens* wild-type GC-1 α GC^{cat} and β GC^{cat} (4NI2-A and 4NI2-B, respectively), *C. reinhardtii* CYG12 GC_{Cr} cyclase (3ET6), *Blastocladia emersonii* GC_{Rho} cyclase (6AO9), and *Synechotistis* PCC6803 GC_{Cya2} cyclase (2W01). The secondary structure elements (α helices: α 1- α 5, β strands: β 1- β 10, TT: β -turns) represented above the sequence belong to β GC^{cat}. Numbering is indicated for all sequences. Residues important for catalysis are highlighted 1-8 above the sequence alignment as in Table 2.1. Invariant residues are highlighted in red boxes while similar residues across all sequences are highlighted in yellow boxes. The consensus sequence (identity > 70%) is shown below the alignment. Upper case represents identity; lower case represents consensus level>0.5; ! is anyone of IV residues, # is anyone of NDQEBZ (from BloSUM32 table), dots are residues that are not conserved. Stars above the sequence represents residues with alternate positions.

Finally, a sequence alignment with other bacterial cyclases suggests that Cya2 may be representative of a bacterial guanylyl cyclase sub-group, raising the interesting question about the exact role played by cGMP in these organisms.

2.4.3. Eukaryotic guanylyl cyclase

Winger *et al.* solved the crystal structure of the catalytic domain of the soluble guanylyl cyclase (CYG12) from the eukaryotic green algae *Chlamydomonas reinhardtii*.⁸⁹ CYG12 functions as a homodimer and the guanylyl cyclase domain (termed GC_{Cr}) adopts a Chinese yin-yang fold similar to C1/C2 in AC, as expected (**Figure 2.3d**). The homodimer contains two symmetric active sites at the dimer interface. Contrary to the Cya2 guanylyl cyclase,⁸⁸ CYG12-GC_{Cr} showed positive cooperativity, implying communication between the two sites.

Based on sequence alignments (**Figure 2.4**), superposition with the structure of AC catalytic domain as well as structure modeling,¹⁰³ the residues involved in GTP binding and catalysis were inferred. While the GC_{Cr} structure was solved in the absence of metal or substrate, key conserved residues include Asp residues binding the metal ions, Asn binding the ribose moiety of GTP, Lys and Arg stabilizing the phosphate moieties, and a canonical Glu-Cys pair for nucleobase specificity (**Table 2.1**). Most of these residues were found in locations close to their AC counterparts, highlighting the likely conservation of catalytic mechanisms in both enzymes. Dimethyl-arsenic modification of Cys residues promoted local distortions in structural elements forming the active site, and was cited as a possible cause for failing to observe metal and substrate in the crystal structure. Comparison of this inactive open structure with that of the closed AC structure with metals and substrate

analogs (PDB code 1CJU) suggested a possible activation mechanism for CYG12. Tesmer *et al.* proposed that movements of helices $\alpha 1$ and $\alpha 4$ were key hallmarks of activation in adenylyl cyclases.⁹⁵ In the GC_{Cr} structure, both helices adopt conformations also observed in the AC inactive structure, reinforcing the idea that the structure corresponds to the inactive state. Finally, the authors speculated that a groove found at the surface of the monomer B (equivalent to C2 subunit in AC) could provide a docking site for regulators like the HNOX domain, similarly to the G_{s α} binding pocket in AC. GC_{Cr} shares 44.2% and 40.3% sequence identity with human β GC^{cat} and α GC^{cat} subunits, respectively (**Figure 2.4**). Thus, this structure represented the best model for the human catalytic domain at the time.

2.4.4. Human mutant guanylyl cyclase

It took almost 5 years for the first structure of human $\alpha\beta$ GC^{cat} to become available⁹⁰ and confirm most predictions based on homologous structures and sequence alignments. While crystallizing the $\beta\beta$ GC^{cat} homodimer was straightforward (**Figure 2.3e**), obtaining the heterodimer structure required engineering of an interfacial disulfide bridge, while mutating out one of the natural Cys in β GC^{cat} to avoid favoring $\beta\beta$ GC^{cat} homodimers. Unfortunately, this mutation is inactivating,^{104,105} and catalytic activity could not be detected for the mutant heterodimer in the presence of Mg²⁺ (**Table 2.2**). The human catalytic domains adopt the head-to-tail wreath fold observed in other class III cyclases. The active site is located at the dimer interface and each subunit contributes key residues. While the structure is in the inactive open state, comparison with the C1/C2 AC heterodimer bound to substrate analog ddATP and Mg²⁺ confirms residues important for catalysis:

α Asp530 and α Asp486 for Mg^{2+} coordination, α Arg574, β Arg552, and β Lys593 for phosphate tail stabilization, β Asn548 for ribose binding, and the pair β Glu473- β Cys541 for nucleobase specificity (**Table 2.1**). The Glu-Cys pair has been heralded as the hallmark for GTP specificity. However, GC-1 has been shown to be quite promiscuous compared to other cyclases, and can also generate cAMP, cIMP, and cXMP.¹⁰⁶ A superimposition of the open apo $\alpha\beta GC^{cat}$ structure on the closed ligand-bound C1/C2 AC structure (PDB code 1CJU) suggested that a much larger conformational change (26° rotation) of the αGC^{cat} subunit would be necessary for activation, as suggested earlier.⁸⁹ Finally, a pseudo-symmetric active site is created, but its size is much smaller than in AC, and it remains to be seen whether it can accommodate small molecule activators (**Figure 2.5**).

Table 2.2. Basal guanylyl cyclase activities. Comparison of reported specific activities (nmol cGMP/min/mg protein) and calculated specific activities adjusted for amounts of heterodimers (100% for GC-1) and normalized to pmol of protein (fmol cGMP/min/pmol heterodimer). @: activity measured in cell lysate. #: calculated activity assuming 100% heterodimeric $\alpha\beta\text{GC}^{\text{cat}}$. \$: activity measured using $\alpha 661\text{-}\beta\text{GC}^{\text{cat}}$ with 82.5% heterodimers as measured (30 residues truncated from $\alpha\text{GC}^{\text{cat}}$ C-terminus). N/D: not determined. All assays performed at 37 °C except where noted (*).

	Reported specific activity (nmol cGMP/min/mg)		Adjusted specific activity (fmol cGMP/min/pmol heterodimer)		Ref.
	Mg^{2+}	Mn^{2+}	Mg^{2+}	Mn^{2+}	
Full-length GC-1	114	610	16,876	90,301	107
	12.1	96	1,791	14,211	108
	50@	400@	N/D	N/D	109
	22.6	N/D	3,391	N/D	110* (?)
	46.4-153	1,259	6,869-22,649	186,376	111
	0.397@	N/D	N/D	N/D	112
	0.046	N/D	6.86	N/D	113
	152	N/D	22,501	N/D	114
	28	662	4,145	97,955	106
	4,300	N/D	636,551	N/D	90
	0.10@	N/D	N/D	N/D	78* (30 °C)
	2	15	296	2,220	115
	67.7	138.3	10,075.5	20,578.5	91* (15 °C)
	N/D	60@	N/D	N/D	109
	0.56	11-72	27.6#	547-3,582#	116
	N/D	48	N/D	2,388#	114
	N/D	25-300	N/D	1,244-14,926#	90
	62	N/D	3,085#	N/D	117
	1	N/D	49.5#	N/D	118
	35.4	N/D	2.2	N/D	91* (15 °C)
	25\$	19,394\$	1.4\$	1,091\$	91* (15 °C)
$\alpha\beta\text{GC}^{\text{cat}}$					

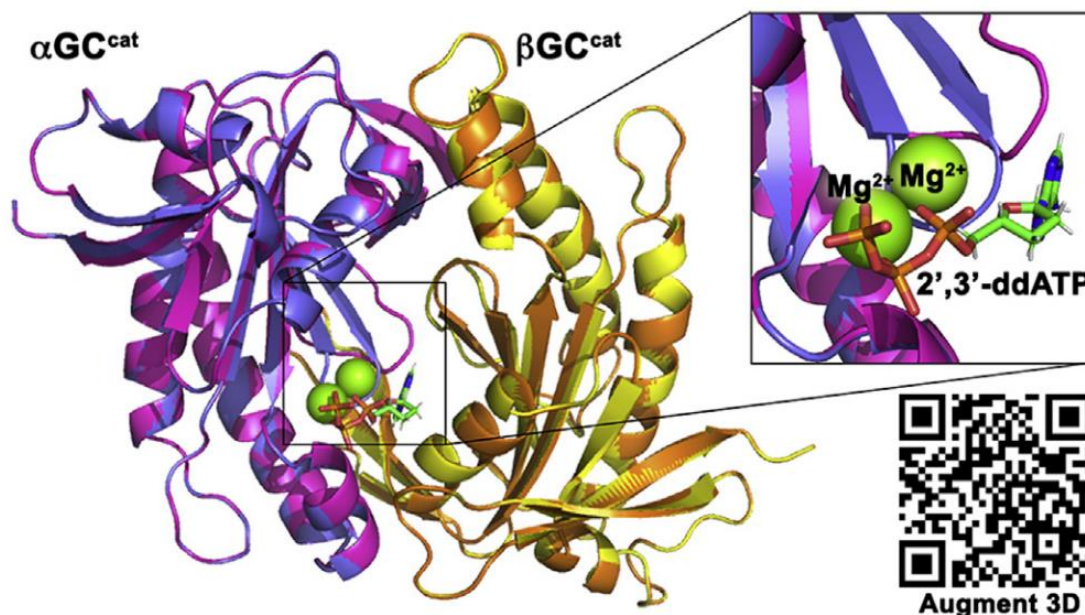


Figure 2.5. Model of activated $\alpha\beta\text{GC}^{\text{cat}}$. Theoretical model of activated $\alpha\beta\text{GC}^{\text{cat}}$ bound to Mg^{2+} and 2,3'-ddATP. The model was obtained by superimposition of inactive $\alpha\beta\text{GC}^{\text{cat}}$ (PDB code 4NI2) on “active” adenylyl cyclase structure (PDB code 1CJU). Superposition of the inactive and active GC^{cat} subunits independently shows that the 26° rigid body rotation of the $\alpha\text{GC}^{\text{cat}}$ subunit around $\beta\text{GC}^{\text{cat}}$ allows structural elements of both subunits to close the active site. In addition, the substrate binding loop become more structured in the active model. Inset depicts structural rearrangement at the substrate binding pocket containing two Mg^{2+} ions (green) and 2',3'-dideoxyadenosine 5'-triphosphate (2,3-ddATP). $\alpha\text{GC}^{\text{cat}}$ (magenta-inactive, violet-active) and $\beta\text{GC}^{\text{cat}}$ (yellow-inactive, orange-active).

2.4.5. Human wild-type guanylyl cyclase

Our lab was the first to solve the structure of the human wild-type $\alpha\beta\text{GC}^{\text{cat}}$ domain (**Figures 2.3g** and **2.3h**) in its apo inactive state.⁹¹ Comparison with the mutant heterodimer structure⁹⁰ reveals how subtle conformational changes at the dimer interface can affect catalytic activity. In agreement with biochemical and biophysical data, we identified three main regions with the highest degree of sequence conservation: (i) the substrate channel; (ii) the C-terminal subdomain of the $\alpha\text{GC}^{\text{cat}}$ subunit, which could serve as a docking site to the regulatory HNOX domain, and in agreement with HDXMS studies;¹¹⁷ and (iii) the dorsal face of the heterodimer

containing both N-termini that could serve as the docking site for the coiled-coil domain, again in agreement with HDXMS studies.¹¹⁷ We identified two structural motifs that likely modulate the orientation of the two subunits with each other and catalytic activity (**Figures 2.3g** and **2.3h**). The first one is a conserved β -hairpin in the $\beta\text{GC}^{\text{cat}}$ subunit (flap-wrap) that wraps onto the $\alpha\text{GC}^{\text{cat}}$ subunit. In particular, the $\beta\text{Met537Asn}$ mutation in this flap was shown to increase constitutive GC-1 activity and enhance the response to NO/YC-1.¹⁰¹ A similar mutation in AC increased both activity and affinity of the C1 and C2 subunits without activators.¹¹⁹ We proposed that the mutation would promote interactions between the two subunits that may help promote realignment of the catalytic residues for optimal activity. The second structural motif is an interfacial hydrogen-bond network between αGlu526 , αCys595 , and βThr474 , similarly to what was observed in AC. Mutations in this triad that abrogate hydrogen bonds lead to severely impaired catalytic activity in GC-1^{101,120} and AC^{119,121}, while a conservative mutation ($\alpha\text{Cys595Ser}$) lead to increased basal activity in GC-1¹⁰⁵.

We were the first to show unambiguously that co-purified $\alpha\text{GC}^{\text{cat}}$ and $\beta\text{GC}^{\text{cat}}$ subunits assemble in solution as a complex mixture of monomers, homodimers, and heterodimers.⁹¹ Using size exclusion coupled to multi-angle x-ray scattering, nano-ESI/MS and nano-ESI/ MS/MS, we were able to quantitatively determine for the first time dimerization K_D for $\beta\beta\text{GC}^{\text{cat}}$ homodimers ($< 2\ \mu\text{M}$), $\alpha\beta\text{GC}^{\text{cat}}$ heterodimers ($\sim 6.9\ \mu\text{M}$), and $\alpha\alpha\text{GC}^{\text{cat}}$ homodimers ($30\ \mu\text{M}$). These results are in contrast with previous studies that suggested that the K_D of homodimers was much higher than that of heterodimers,¹¹⁶ most likely because of the difference in the methods used in each

study. In addition, salt concentrations may play a role in the rate of dimerization, as discussed in **section 2.4.2**. Because mass spectrometry is sensitive to salt, our experiments were performed using non-physiological volatile salt buffers. Regardless, our results are in agreement with our analyses of the dimer interfaces that show that the buried area and number of hydrogen bonds, salt bridges, and hydrophobic interactions are greater in the $\beta\beta\text{GC}^{\text{cat}}$ homodimers compared to the $\alpha\beta\text{GC}^{\text{cat}}$ heterodimers. Finally, our results had important implications: when measuring activity of the catalytic domains, choosing a concentration that enables heterodimer formation is critical (i.e. $> 10 \mu\text{M}$). While doing so will not reduce the amount of $\beta\beta\text{GC}^{\text{cat}}$ homodimers, higher protein concentrations will increase the amount of $\alpha\beta\text{GC}^{\text{cat}}$ heterodimers.

Taking this into account, our activity measurements adjusted to the amount of heterodimer revealed that the $\alpha\beta\text{GC}^{\text{cat}}$ only possess $\sim 0.01\%$ of basal full-length GC-1 activity using Mg^{2+} . The activity of $\alpha\beta\text{GC}^{\text{cat}}$ increased 779-fold when using Mn^{2+} as a cofactor while full-length GC-1 activity increased by ~ 2 -fold, but $\alpha\beta\text{GC}^{\text{cat}}$ still showed less than 6% of GC-1 activity (**Table 2**). Few studies directly compare specific activity of full-length GC-1 and truncated constructs. The published values of specific activity for full-length GC-1 and truncated constructs show great variation (**Table 2**), even after adjusting for heterodimer amounts and calculating specific activity in fmol/min/pmol of protein (instead of pmol/min/mg of protein). Possible reasons for discrepancy include protein concentrations, temperature, sample purity, heme content of the full-length constructs, and amount of heterodimers for the catalytic constructs. Our results showed that the isolated $\alpha\beta\text{GC}^{\text{cat}}$ domains are not

catalytically competent despite their ability to dimerize. We thus proposed that other GC-1 domains (including the coiled-coil domain) modulate the relative orientation of the catalytic domains and are necessary to promote an optimal conformation of the catalytic domains via structural changes.

2.4.6 The guanylyl cyclase of the fusion protein RhoGC

Very recently, the structure of the catalytic guanylyl cyclase domain of the fusion protein RhoGC from the aquatic fungus *Blastocladiella emersonii* was solved.⁹² The homodimeric transmembrane protein senses light through a rhodopsin domain (residues 176-388) and transduces the signal via a coiled-coil domain to the cytosolic catalytic GC_{Rho} domain (residues 443-626) where GTP can be cyclized for phototaxis.^{122,123} Kumar *et al.* expressed and purified two constructs containing the catalytic domain: GC_{Rho} and GCwCC_{Rho} (with coiled-coil domain), which are monomeric in solution and surprisingly both catalytically active. Substituting Mg²⁺ for Mn²⁺ significantly increased activity for GC_{Rho} (330-fold), but not GCwCC_{Rho} (1.4-fold). In addition, the presence of the coiled-coil domain decreased overall activity (21-fold) in the presence of Mn²⁺, but increased overall activity (11-fold) in the presence of Mg²⁺. This is in agreement with earlier studies¹²³ suggesting that other domains of RhoGC modulate the activity of the cyclase domain, and has also been proposed for human GC-1.^{90,91,116} The structure of monomeric GC_{Rho} (**Figure 3f**) is very similar to that of other guanylyl cyclase domains,⁸⁸⁻⁹¹ as expected based on sequence identity (36–37% with human $\alpha\beta$ GC^{cat}, **Figure 2.4**). Crystallization trials in the presence of substrate analog ddGTP and Mn²⁺ yielded a homodimeric structure. Yet, ddGTP was not observed in the electron density and a disulfide bridge between

the two subunits forced a non-canonical head-to-head conformation of the homodimer that is likely not biologically relevant. Interestingly, the GCwCC_{Rho} protein did not show significant disulfide formation, suggesting that the presence of the coiled coil may promote a different conformation. This result is in agreement with previous studies⁸¹ that showed that the coiled-coil domain plays a preponderant role in GC-1 dimer formation. Analytical ultracentrifugation and size exclusion chromatography showed the presence of monomeric and dimeric GC_{Rho} in solution when ddGTP and Mn²⁺ were added. However, in the absence of substrate analog and metal, both GC_{Rho} and GCwCC_{Rho} were exclusively monomeric. The cyclase activity of GC_{Rho} was shown to be dependent on enzyme concentration, as observed previously,⁸⁸ providing indirect evidence for transient catalytically active homodimers. However, contrary to what was reported for Cya2,⁸⁸ the activity of GC_{Rho} does not reach a maximum, even at an enzyme concentration of 60 μ M. We noted that the activity assays were performed in low salt, while the size exclusion chromatography, AUC, and crystallization experiments were performed at higher salt concentration. While this may seem a trivial difference, Rauch *et al.* had showed that Cya2 was monomeric at higher salt concentration, and dimeric at lower salt concentrations.⁸⁸ Therefore, we propose that the activity and oligomerization of GC_{Rho} are likely dependent on salt concentration. Experiments to verify this hypothesis are necessary. Regardless, from the data presented, the authors propose that GC_{Rho} has a much weaker dimerization affinity (60–80 μ M) than other cyclases, including human $\alpha\beta$ GC^{cat}. While Winger *et al.* had suggested a dimerization K_D of ~ 0.45 μ M for $\alpha\beta$ GC^{cat},¹¹⁶ we found that human catalytic domains are purified as a mixture of monomers, homodimers, and

heterodimers.⁹¹ Our extensive mass spectrometry studies, unfortunately not taken into account in Kumar *et al.*, showed that the catalytic domain heterodimerization K_D is much higher than previously thought (see **section 2.4.5**), and likely causes the difficulties in obtaining $\alpha\beta\text{GC}^{\text{cat}}$ crystals.

2.5. Structural determinants for catalytic activity

The structure of the active $\alpha\beta\text{GC}^{\text{cat}}$ structure has remained elusive. However, several studies have suggested how specific structural elements are involved in $\alpha\beta\text{GC}^{\text{cat}}$ transitioning from the open inactive conformation to the closed active state (**Figure 2.5**).

2.5.1. Activating mutations

Only two mutations have been reported to significantly increase basal GC-1 activity and both are located at or near the $\alpha\beta\text{GC}^{\text{cat}}$ dimer interface.^{101,104,105} First, the $\alpha\text{Cys595Ser}$ mutation showed a 3.8-fold increased basal activity over wild-type,¹⁰⁴ mainly due to increased GTP affinity (10-fold lower K_m).¹⁰⁵ The authors suggested that the mutation allowed GC-1 to increase catalytic activity through a conformational rearrangement similar to that induced by Mn^{2+} substitution. Based on our structure of wild-type $\alpha\beta\text{GC}^{\text{cat}}$ and activity measurements with Mg^{2+} and Mn^{2+} ,⁹¹ we postulated that the thiol-to-hydroxyl substitution in the $\alpha\text{Cys595Ser}$ mutant enhances hydrogen bonding with nearby residues αGlu526 and βThr474 , promoting a reorientation of the residues at the dimer interface leading to an increase in basal cGMP output (**Figure 2.3g**). This hypothesis is supported by earlier studies showing that $\alpha\text{Cys595Asp}$, $\alpha\text{Cys595Tyr}$, and $\alpha\text{Glu526Ala}$ mutations all resulted into

significantly reduced basal and NO-stimulated activity^{101,120} (see **section 2.5.2**), suggesting these residues may be involved in crucial inter-subunit contact. However, in the case of the α Cys595 residue, we cannot rule out the role of Cys oxidation or potential Cys-S-NO modifications (see **section 2.5.3**). Finally, other studies have also proposed that the α Cys595 residue could participate in YC-1 stimulator¹⁰¹ or ATP binding in the pseudo-symmetry site of the catalytic domain.^{124,125} However, recent studies have unambiguously showed that stimulators bind to the β HNOX domain of GC-1.⁶⁰

Second, the β Met537Asn mutation was designed based on the homologous mutation in AC (C2-Lys1014Asn). While the K_m value was unchanged, basal Vmax increased 6.8-fold in the mutant enzyme.¹¹⁹ In addition, stimulation by NO and YC-1 increased activity of the mutant enzyme 48.4-fold and 4.5-fold, respectively. Consequently, for the mutant enzyme, both basal and NO-stimulated activity are significantly greater than those in wild-type GC-1 (5.9-fold and 3.7-fold, respectively). Similar to the aforementioned α Cys595Ser mutation, Lamothe *et al.* postulated that the β Met537Asn mutation enhances interfacial interactions at the catalytic domain for improved basal activity (**Figure 2.4**). Based on our structure of the human wild-type $\alpha\beta$ GC^{cat} (**Figure 2.3h**), we speculated that the β Met537Asn mutated residue could potentially interact with α Lys524 and α Thr527.⁹¹ Other studies showed that the α Lys524Ala mutation (see **section 2.5.3**) reduced heterodimerization (3-fold), as well as basal GC-1 activity (38-fold),¹²⁰ thus supporting our hypothesis regarding potential intersubunit contacts involving α Lys524.

2.5.2. Inactivating mutations

Mutations in the catalytic domain that reduce basal and/or NO-stimulated activity have also aided in identifying regions in $\alpha\beta\text{GC}^{\text{cat}}$ crucial for cGMP turnover. These mutations are located in three main regions: (i) the active site, (ii) the inter-subunit interface near the β -flap, and (iii) the inter-subunit interface near the active site.

2.5.2.1. Mutations in the active site

The $\alpha\text{Asp530Ala}$ mutant had no detectable basal or NO-stimulated activity.¹²⁰ This is not surprising since αAsp530 is located on the $\beta 2$ - $\beta 3$ substrate binding loop and is predicted to coordinate the Mg^{2+} ion based on sequence alignment with adenylyl cyclase (**Table 2.1**) and structural modeling based on metal-containing AC.⁹⁰ Another mutation in the active site showed decreased basal activity. Residue βCys541 has been implicated in substrate specificity.¹⁰³ Substitution with Ser decreased activity in the presence of Mg^{2+} ;^{104,105} however, in the presence of Mn^{2+} , $\beta\text{Cys541Ser}$ retained low catalytic activity and was responsive to NO similarly to wild-type GC-1.¹⁰⁴ To test the putative role of this residue in substrate specificity, the $\beta\text{Glu473}/\beta\text{Cys541}$ pair was mutated into the AC homologous Lys/Asp pair, resulting in conversion of GC-1 into an NO-responsive adenylyl cyclase with abolished GTP cyclase activity.¹⁰³ Finally, the double mutant $\beta\text{Gly476Cys}/\beta\text{Cys541Ser}$ catalytic domain also showed little to no activity in the presence of Mg^{2+} ,⁹⁰ likely due to the $\beta\text{Cys541Ser}$ mutation.

2.5.2.2. The dimer interface near the β -flap

Two mutations near the β -flap showed impaired activity. The α Asp514Ala mutant had no detectable basal or NO-stimulated activity and showed significantly decreased heterodimerization.¹²⁰ The α Lys524Ala mutation resulted in significantly decreased basal cyclase activity and NO-stimulated activity compared to wild type (38-fold and 13.3-fold lower, respectively). However, this mutant was still responsive to NO; while wild-type GC-1 was stimulated by NO 118-fold, the α Lys524Ala mutant activity was increased 338-fold. These two residues are located on the dorsal side of $\alpha\beta$ GC^{cat}, near β Met537 (see **section 2.5.2**) and were predicted to interact with the β GC flap-wrap.⁹¹ A third mutation was recently identified in one individual diagnosed with achalasia, hypertension and Moyamoya disease.¹²⁶ The purified α Cys517Tyr mutant showed decreased basal and NO-stimulated activities (see **section 2.5.3** for details). The bulky Tyr could lead to structural disruption in the α GC^{cat} subunit near the interfacial β GC flap-wrap. Collectively, these studies suggest a crucial role for the β GC flap-wrap not just for heterodimerization and proper orientation of the catalytic subunits crucial for basal activity, but also for NO signal transduction.

2.5.2.3. Mutations in the interfacial region near the active site

Several mutations located near the active site have also been shown to decrease GC-1 activity. First, the α Glu526Ala mutation resulted in significantly decreased basal and NO-stimulated cyclase activity (16-fold and 7-fold, respectively) compared to wild type.¹²⁰ The α Glu526 residue is located at the intersubunit interface near the putative pseudo- symmetric pocket. It has been implicated in binding of

inhibitors in the pseudo-symmetric site of GC-1.¹²⁴ We had proposed that this residue is part of a triad of residues important for orienting the two subunits to promote optimal activity.⁹¹ Residues α Glu526, α Cys595, and β Thr474 could form a network of hydrogen bonds at the dimer interface, similar to the C1a-Lys436/C1a-Asp505/C2a-Thr939 triad in adenylyl cyclase.¹²⁷ This hypothesis is supported by previous mutagenesis studies that abrogate potential hydrogen bonds, including α Cys595Asp, α Cys595Tyr, and α Cys595Asp/ α Glu526Ala.¹⁰¹ More recently, Agullo *et al.* recently proposed that α Glu526 interacts with α Arg593 and β -flap residue β Met537.¹²⁸

Second, the β Asp477Ala mutation showed lower NO- and YC-1-stimulated activity compared to wild-type GC-1, but a higher level of synergy between the two stimulators.¹⁰¹ This residue is located near the putative pseudo-symmetric pocket that lacks key catalytic residues.^{90,129} This site was proposed to bind nucleotides that would regulate the activity of the catalytic site.¹²⁴ A subsequent study suggested that this residue may be important for binding metal ions in the pseudo-symmetric site of GC-1.¹²⁴ In contrast, the double mutant α Cys595Ala/ β Asp477Ala showed similar or slightly higher activity compared to wild-type GC-1.¹²⁵ It was proposed that these residues play a key role in the communication between the two sites, specifically in the presence of excess NO, suggesting a link between NO and nucleotide regulation of GC-1 activity.

Third, mutation of α Cys595 into Tyr significantly decreased basal and stimulated activity (2.8-fold and 2.1-fold, respectively). However, the α Cys595Tyr mutant protein was synergistically activated by NO and YC-1 to a greater extent than

wild type (1.8-fold more). Decreased activity stems from both an increase in K_m and a decrease in V_{max} .¹⁰¹ The remarkable opposite effects of the α Cys595Ser (see **section 2.5.1**) and α Cys595Tyr mutations on basal activity suggested that this residue is important for catalysis, despite not being part of the catalytic site. It was originally proposed that this residue is involved in YC-1 binding, but recent studies have shown that stimulators bind to the β HNOX sensor domain instead.⁶⁰ Instead, we proposed that α Cys595 is part of a network of interfacial hydrogen bonds that promote an optimal orientation of both subunits for high catalytic activity.⁹¹

2.5.3. Cys-NO Modification in GC-1 Desensitizes the Enzyme to NO

S-nitrosation (S-NO) is a well-recognized post-translational modification of Cys residues that regulates a myriad of pathways.¹³⁰ Approximately 3% of GC-1 amino acids are Cys, almost twice the average amount found in globular proteins.¹³¹ Multiple roles for S-NO modified GC-1 have been speculated, including enhanced NO-stimulation^{75,76} or reduced cGMP output, possibly representing a state of oxidative stress. However, the stability of nitrosothiols has also been questioned given the millimolar concentrations of cellular reductants such as glutathione,^{132–134} calling into question the significance of S-NO modified GC-1. While the precise role of this posttranslational modification remains under debate, there are several functions that S-NO may have in tuning GC-1 activity and how $\alpha\beta$ GC^{cat} may be affected.

NO desensitization of GC-1 is characterized by a loss of sensitivity for NO and was shown to occur via S-NO modification of GC-1 Cys residues in primary artery smooth muscle cells treated with S-nitrosocysteine.¹³⁵ Pre-treatment of smooth

muscle cells with a glutathione precursor reduced levels of S-NO modified GC-1 and restored NO-sensitivity. Two Cys residues were found to be posttranslationally S- NO modified, α Cys243 and β Cys122.¹³⁵ Fernhoff *et al.* reported S-NO to be involved in reductive nitrosylation of ferric heme and identified two Cys residues, β Cys78 or β Cys122, acting as nucleophiles in the reaction. Reductive nitrosylation reduces oxidized heme iron using one NO molecule and a nucleophilic base to regenerate the NO-sensitive ferrous heme. Finally, thiol alkylation prevented recovery of NO-sensitivity while DTT treatment rescued ferrous heme, suggesting that reduced Cys residues are crucial for maintaining NO-sensitive GC-1.^{79,136} However, it has been reported that the NO-modified GC-1 Cys residues are not canonical S-NO modifications.⁷⁹ Instead, the authors suggested a radicalized S-NO with the loss of a single electron.

Additional Cys residues modified by S-nitrosation have recently been identified.¹³⁷ Using a combination of the biotin switch assay (BST) and Orbitrap tandem mass spectrometry, Beuve *et al.* enhanced the detection limit of S-NO modifications and identified ten conserved Cys residues as S-NO targets, including six Cys localized to the $\alpha\beta$ GC^{cat} catalytic domains: α Cys517, α Cys595, α Cys610, α Cys629, β Cys541, and β Cys571. These results suggest a potential role for S-NO posttranslational modifications in regulating catalytic activity. The α Cys595 and β Cys541 residues have been shown to play major roles in catalytic activity (see **sections 2.5.1** and **2.5.2**). Residues α Cys629 and β Cys571 are located away from the active site and subunit interface, and their role is not clear. Residue α Cys609, was reported to be involved in a direct interaction between GC-1 and thioredoxin (Trx;

see **section 2.6.2**).⁷⁹ Finally, the α Cys517 residue has been reported by two separate groups to be involved in GC-1 activity and NO-sensitivity. Crassous *et al.* first reported that α Cys517 mediates GC-1 desensitization to NO in angiotensin II-induced hypertension.¹³⁸ Another study revealed the presence of an α Cys517 mutant in a subject presenting Moyamoya disease (MMD). MMD is characterized by aberrant arterial remodeling in the brain leading to thrombosis and hemorrhage and has been associated with a dysfunctional GC-1.¹³⁹ Wallace *et al.* identified the α Cys517Tyr variant in a subject with diagnosed MMD.¹²⁶ *In vitro* NO response curves of the GC-1 α Cys517Tyr mutant indicated a 60% loss of NO-sensitivity, in good agreement with results from Crassous *et al.* Collectively, these results suggest that S-NO modifications of Cys residues could lead to dramatic reduction in GC-1 activity and activation. While the stability and relevance of S-NO modifications is controversial due to the reducing environment in cells, it has been shown that these modifications are specific and controlled mainly by cysteine reactivity and their surrounding microenvironment.^{132,134} These results suggest that S-NO modifications of GC-1 Cys residues are biologically relevant, but that the exact function of these Cys modifications remain to be determined (reviewed in ¹³¹).

2.5.4. Small Molecules Targeting the Catalytic Domain

Identification of small molecules that bind to and activate $\alpha\beta$ GC^{cat} could lead to a novel class of heme-independent GC-1 activators. Cobinamide, a precursor to the biosynthesis of vitamin B₁₂, was found to activate GC-1 independent of heme oxidation.¹¹⁵ With known GC-1 stimulator BAY 41-2272, cobinamide synergistically enhanced cGMP output and approached maximum NO-stimulated activity. Deletion

of the $\alpha\beta$ HNOX domains had no effect on cobinamide sensitivity, supporting the hypothesis that binding could occur in the catalytic domain. Further structural studies and activity measurements using the isolated catalytic domain are necessary to define the binding site for cobinamide and how it could promote activity. Derivatives of YC-1 have been synthesized and screened using surface plasmon resonance (SPR) to determine binding to immobilized $\alpha\beta$ GC^{cat}.¹⁴⁰ SPR measurements identified several small molecules with YC-1 modifications that could bind to the catalytic domain and increase activity. However, because purified $\alpha\beta$ GC^{cat} consists of a mixture of monomers, heterodimers, and homodimers,⁹¹ it is unclear whether the reported small molecules do indeed target the catalytically-competent heterodimer.

Inhibition of GC-1 may seem counterintuitive, but several groups have targeted GC-1 in cases of migraines,¹⁴¹ septic shock,¹⁴² cancer,^{143,144} and neurological disorders such as Parkinson's Disease.¹⁴⁵ Structural characterization of the inhibited C1/C2 adenylyl cyclase domain has alluded to key structural elements involved in domain activation, which could be applied to $\alpha\beta$ GC^{cat}. Nucleotide-based small molecules with 2',3'-O-(2,4,6-trinitrophenyl) (TNP)- or 2',3'-O-(N-methylanthraniloyl) (MANT)-substitutions at the NTP ribosyl ring display nanomolar affinity for GC-1^{146–149} and are predicted to bind in the GTP-binding cleft in $\alpha\beta$ GC^{cat}. Crystal structures of C1/C2 bound to either TNP-ATP, MANT-ATP or MANT-GTP were subsequently solved and used to identify key interactions between the inhibitor and cyclase subunits.¹⁵⁰ These results confirmed that MANT/TNP binding occurred in the hydrophobic pocket and showed several ionic interactions between the NO₂ groups of TNP and Asn1022 and Asn1025 from the C2 subunit. Structural

comparison between the three inhibitors also highlighted a highly plastic dimer interface that can accommodate different nucleobases. These studies suggested that inhibitor binding traps the catalytic domain in a competent, but inhibited, conformation.

Dove *et al.* expanded on how this class of competitive inhibitors could be used to target the active $\alpha\beta\text{GC}^{\text{cat}}$ domain.¹⁴⁹ TNP-ATP, TNP-GTP, and 2'-MANT-3'-dATP were shown to potently inhibit GC-1 with K_i of 7.3 nM, 8.6 nM, and 16.7 nM respectively. Molecular modeling using the mutant $\alpha\beta\text{GC}^{\text{cat}}$ crystal structure (PDB code 3UVJ) and docking with 2'-MANT-3'- dATP supported the theory that inhibitor binding could induce partial domain closure including a 27° rotation of αGC around βGC as previously proposed.^{89–91} While complete domain closure is not possible due to the bulky MANT/TNP moiety, these inhibitors could be ideal for targeting the activated $\alpha\beta\text{GC}^{\text{cat}}$ domain due to their high affinity and increased fluorescence upon binding.

Recently, several groups have synthesized non-nucleotide-based small molecules that reportedly bind to $\alpha\beta\text{GC}^{\text{cat}}$ with μM affinity. Mota *et al.* identified quinoxaline-based small molecules with a K_D of 11 μM .¹⁵¹ Activity assays using GC-1, GTP and activator cinaciguat suggested these molecules inhibit active GC-1, but do not compete with substrate binding. Molecular modeling suggested binding to the supposed pseudo-symmetric site. However, earlier studies by the same group proposed binding of YC-1 to the catalytic domain,¹⁴⁰ in contrast to the recent studies showing that these stimulators bind to the βHNOX domain.⁶⁰ Therefore, the exact binding site of these inhibitors remains elusive.

In silico screening was performed using the $\alpha\beta\text{GC}^{\text{cat}}$ crystal structure (PDB code 3UVJ) to discover inhibitors that bind in the pseudo-symmetric pocket.¹¹⁸ Two molecules were shown to inhibit basal and NO- stimulated GC-1 with K_i of $\sim 20\text{--}30\ \mu\text{M}$. Only one of the two compounds was capable of inhibiting the isolated catalytic domains, albeit with severely diminished potency; $100\ \mu\text{M}$ was used to inhibit 99% GC-1 activity while $400\ \mu\text{M}$ inhibited $>50\%$ of activity using $\alpha\beta\text{GC}^{\text{cat}}$. Regardless, the determination of the exact binding site of these molecules awaits structural characterization.

2.6. Protein-protein interactions regulating GC-1 activity

2.6.1. βHNOX - $\alpha\beta\text{GC}^{\text{cat}}$ interactions

Despite the determination of low-resolution electron-microscopy structures of GC-1,⁸⁷ the mechanism by which NO regulates its activity remains unknown. One hypothesis is that direct interaction between $\alpha\beta\text{GC}^{\text{cat}}$ and βHNOX transduces the signal of NO-stimulation. Several groups aimed to test this mechanism. This hypothesis was first suggested by Winger *et al.*,¹¹⁶ who showed that increasing molar equivalents of βHNOX or βHNOX -PAS and most of the CC domain ($\beta 385$) added to $\alpha\beta\text{GC}^{\text{cat}}$ yielded stepwise decreases in catalytic activity.¹¹⁶ However, two observations raised questions about a possible interaction between the two domains: a large molar excess of βHNOX -PAS compared to $\alpha\beta\text{GC}^{\text{cat}}$ (15:1) was necessary to elicit a $\sim 55\%$ decrease in activity, and adding NO had no effect on inhibition. Regardless, the authors suggested that βHNOX could act as an autoinhibitory element on GC-1 activity. Another study further supported a possible interaction between the

N-terminal domains and the C-terminal catalytic domains. Förster resonance energy transfer (FRET) analysis of fluorescent fusion proteins showed the proximity of the HNOX domains and the catalytic domain.¹⁵² Importantly, fusion of the large fluorescent proteins (YFP and CFP) to GC-1 did not affect its basal or stimulated activity. However, NO binding had no effect on FRET efficiency, as observed previously, suggesting that this potential interaction between β HNOX and $\alpha\beta$ GC^{cat} is independent of NO binding. A recent study using C-terminally tagged CFP-tagged α GC-1 and YFP-tagged β GC-1 polypeptides showed a modest increase in FRET efficiency (~10%) upon NO-donor addition, which would support domain closure and tighter interactions between α GC^{cat} and β GC^{cat}. Adding GTP slightly reduced FRET efficiency by ~7%, which could indicate opening of the substrate binding pocket. However, none of the in vitro or in vivo fluorescence measurements recorded by Pan *et al.* were correlated to GC-1 activity.¹⁵³ Adding NO had no effect on FRET efficiency when using CFP- α GC-1 (N-terminally tagged) and β GC-1-YFP (C-terminally tagged), in agreement with previous studies.¹⁵²

Busker *et al.* were the first to report NO-induced alterations in interactions between β HNOX and $\alpha\beta$ GC^{cat}. Endogenous Trp residues located in β HNOX (Trp22), β GCcat (Trp602), α PAS (Trp352), α CC (Trp466), and α GCcat (Trp669) were used as FRET donors, and MANT- dGTP bound to the catalytic domain was used as a FRET acceptor.¹⁵⁴ While the low quantum yield of Trp residues make them suboptimal FRET partners,¹⁵⁵ changes in FRET efficiency were observed in this study. In wild-type GC-1, FRET efficiency increased 155% upon NO stimulation, while the α CC Trp466Phe mutation reduced FRET efficiency compared to wild-type GC-1. This

suggests that Trp466 may be involved in NO-induced signal transduction. By retaining Trp22 in β HNOX and Trp466 as the only FRET donors, FRET efficiency increased to 200% upon addition of NO, suggesting that these two Trp moved closer to the MANT-GTP molecule. Busker *et al.* concluded that domains docking onto $\alpha\beta$ GC^{cat} lead to low activity. NO binding induces a conformational rearrangement in the heme pocket that is carried directly to $\alpha\beta$ GC^{cat} via Trp22 in β HNOX as well as indirectly through the PAS and CC domains via Trp466 in α CC to promote an active conformation of the catalytic domain.

Hydrogen-Deuterium Exchange Mass Spectrometry (HDXMS) studies have further supported a model where β HNOX interacts directly with the $\alpha\beta$ GC^{cat} domain. The first study mapped interactions between the β HNOX- PAS construct and the $\alpha\beta$ GC^{cat} domain.¹¹⁷ The $\alpha\beta$ GC^{cat} domain exhibit decreased deuterium incorporation mostly in the C-terminal lobe (residues 601-655) of α GC^{cat} in the presence of β HNOX-PAS compared to the catalytic domain alone. The decreased deuterium incorporation in that region of $\alpha\beta$ GC^{cat} was also observed in the context of full-length GC-1, suggesting that this region could be involved in interactions with β HNOX-PAS. The C-terminal region of β GC^{cat} (residues 568-604) also showed decreased deuterium incorporation in the presence of β HNOX-PAS, but this was not observed in the context of full-length GC-1. These results suggest that the C-terminal region of α GC^{cat} could be involved in direct interactions with the N-terminal sensor domain of GC-1 (**Figure 2.4**). This model is supported by the fact that this region presents high sequence conservation,⁹¹ and studies showing that the α Arg624Ala mutation in that region drastically reduced GC-1 activity.¹²⁰ Another study by the same group showed

that NO addition to full-length GC-1 resulted in changes in H/D exchange rates in all domains of GC-1.¹⁵⁶ In the catalytic domains, the substrate-binding loop of $\alpha\text{GC}^{\text{cat}}$ (region 522-532) and the β -flap wrap (region 586-593) showed decreased exchange, while the substrate-binding loop of $\beta\text{GC}^{\text{cat}}$ (residues 469-482) showed increased exchange. The α -helices that “cap” the active site in both subunits ($\alpha 599$ -610 and $\beta 545$ -556) showed decreased deuterium incorporation, suggesting an overall “closing” of the active site. In addition, subtle decreased exchange in the C-terminal lobe of $\alpha\text{GC}^{\text{cat}}$ and $\beta\text{GC}^{\text{cat}}$ was also observed. Ultimately, these studies show that subtle rather than large conformational changes distributed along the GC-1 polypeptide seem to be part of the activation mechanism by NO (**Figure 2.5**). This mechanism was further supported by electron microscopy studies that showed that GC-1 shows a high degree of flexibility.⁸⁷ This study confirmed previous results suggesting that the coiled-coil domains act as a scaffold and provide two pivot points for other GC-1 domains to move.⁸⁵ GC-1 assembles in a continuous range of conformations, with the two extremes corresponding to an extended conformation and a collapsed conformation. In the extended conformation, the $\alpha\beta\text{GC}^{\text{cat}}$ and the $\alpha\beta\text{HNOX-PAS}$ domains are located on either end of the extended coiled-coil domain. In the collapsed conformation, the $\alpha\beta\text{HNOX-PAS}$ is folded on the coiled-coil domain with the βHNOX in close proximity to the catalytic domain. Interestingly, adding NO, a non-cyclizable GTP analog, or both did not significantly alter the range of conformations adopted by GC-1.

Taken together, results from these complementary studies suggest that NO-stimulation of GC-1 is not a simple on-off switch where, in the absence of NO,

β HNOX maintains $\alpha\beta$ GC^{cat} in an inactive conformation through a direct interaction and, upon NO binding to heme, β HNOX is released and optimal catalytic activity can occur. Instead, NO-stimulation may trigger subtle changes in conformations and interactions across each domain that orient $\alpha\beta$ GC^{cat} in an optimal conformation for catalysis (**Figure 2.5**).

2.6.2. Interactions with thioredoxin (Trx)

Trx is typically known to mediate disulfide bonds but can also de-nitrosylate S-NO residues, suggesting Trx may act as a switch in sensitizing and desensitizing GC-1 to NO. Co-expression of GC-1 and Trx improved NO-stimulated GC-1 activity (~2-fold) while inhibition of activated Trx led to an increased amount of S-NO modified GC-1 and significantly decreased NO-sensitivity.⁷⁸ Using a proximity ligation assay and immunoprecipitation, Trx was found to associate primarily with α GC-1 via a disulfide linkage with α Cys609. Molecular docking using structures of Trx and $\alpha\beta$ GC^{cat} (PDB code 4NI2) suggested Trx docks onto the C-terminal lobe of α GC^{cat}, very close to the substrate-binding groove, to mediate S-NO modifications on GC-1. The authors proposed that Trx binding could compete with HNOX binding to the catalytic domain or de-nitrosate other GC-1 residues. The mechanism of Trx-induced protection of GC-1 activity remains to be determined.

2.6.3 Interactions with protein-disulfide isomerase (PDI)

Protein-disulfide isomerase (PDI) assists in protein folding by catalyzing disulfide bond formation and breakage using a Cys-X-X-Cys motif in its active site. An interaction between PDI and GC-1 was reported using a GC-1 affinity matrix.¹⁵⁷

Non-reducing gel electrophoresis and immunoprecipitation indicated this interaction is redox-controlled.¹⁵⁸ Comparing basal and NO-stimulated GC-1 activities in the presence of PDI found that PDI primarily targets NO-stimulated GC-1, reducing NO-stimulated activity by 41%. Using amine linkage and tandem mass spectrometry previously employed to cross-link Lys residues in GC-1 and identify domain-domain interactions,⁸⁵ Heckler *et al.* found cross-links between PDI and GC-1 residues α Lys672 and β Lys615, both located on disordered C-terminal regions not visible in the crystal structures of $\alpha\beta$ GC^{cat}.¹⁵⁹ Truncations of GC-1 indicated PDI preferentially interacts with the α GC^{cat} subunit. Molecular dynamics studies suggested that PDI could interact with α GC^{cat} to prevent NO-activation in a fashion similar to β HNOX. Together, these results hint at a redox-dependent interaction between the catalytic domain of GC-1 and PDI through a disulfide linkage.

2.7. Conclusions

Much progress has been made toward characterizing NO-stimulated GC-1, but we still lack a mechanistic understanding of how $\alpha\beta$ GC^{cat} transitions between inactive and active forms in the full-length enzyme. Structural studies of GC catalytic domains from different organisms and the C1/C2 domain from AC have aided in identifying catalytic residues, potential allosteric sites for small molecules, and regions in the catalytic domain possibly involved in protein-protein interactions either with other GC-1 domains or other protein partners. Determination of the activated $\alpha\beta$ GC^{cat} conformation will expand on small molecules that can target $\alpha\beta$ GC^{cat}. These small molecules will aid, not only in structural studies aimed at characterizing the catalytic domain, but in creating a novel class of pharmaceuticals to target GC-1 independent

of the NO-sensor domain. Further studies are required to determine what role β HNOX plays in regulating $\alpha\beta$ GC^{cat} and to identify additional protein-protein interaction partners that assist GC-1. While we still lack a high-resolution structure of GC-1, this should not impede progress in the field, but rather drive researchers to utilize alternative methods toward understanding and targeting dysfunctional GC-1 in a variety of diseases.

2.8 Dissertation Outline

The goal of this project was to determine structural elements that are involved in coordinating GC-1 activation and to structurally characterize the activated $\alpha\beta\text{GC}^{\text{cat}}$. Current literature suggests that a series of amino acids propagates the NO-binding event to orient the catalytic domain into a catalytically-competent conformation. Elucidation of these amino acids will aid in a structure-based drug design targeting GC-1 for improved activity. To accomplish this, we set out the following aims:

2.8.1 Specific Aims

2.8.1.1. Aim 1: Identify the amino acids that orient the catalytic domain and promote full catalytic activity

We hypothesize that GC-1 catalysis relies on a network of amino acids across the full-length enzyme. To test this hypothesis, we employed a luciferase reporter assay, extracellular cGMP and cAMP measurements, and molecular dynamic simulations.

2.8.1.2. Aim 2: Structurally characterize the activated $\alpha\beta\text{GC}^{\text{cat}}$ domain

This aim outlines the extensive attempts made to determine the activated $\alpha\beta\text{GC}^{\text{cat}}$ structure. First, we present the crystal structure of the catalytically-inactive Met537Asn $\beta\beta\text{GC}^{\text{cat}}$ homodimeric mutant. We then describe various attempts to overcome $\beta\beta\text{GC}^{\text{cat}}$ homodimerization and biophysically characterize the active heterodimer including designing a “linked” construct, which fuses the C-terminus of

$\alpha\text{GC}^{\text{cat}}$ to the N-terminus of $\beta\text{GC}^{\text{cat}}$, bio-layer interferometry (BLI), and activity assays on wild-type and mutant $\alpha\beta\text{GC}^{\text{cat}}$.

Chapter 3: Novel Synergistic Mutations in Soluble Guanylyl Cyclase Reveal a Key Role for Interfacial Dorsal Flaps in the Activation Mechanism

This work is being prepared as a manuscript to be submitted to the *Journal of Molecular Biology*. **Childers, KC.**, Giannakoulis, S., Amason, J., and Garcin, ED. “Novel Synergistic Mutations in Soluble Guanylyl Cyclase Reveal a Key Role for Interfacial Dorsal Flaps in the Activation Mechanism.”

3.1. Abstract

Soluble guanylyl cyclase (GC-1), the main receptor for nitric oxide (NO), is a central component of the NO-cGMP pathway, critical to cardiovascular system function. NO binding to the N-terminal sensor domain of GC-1 enhances the cyclase activity of the C-terminal catalytic domain. Our understanding of the structural elements that are involved in this signaling cascade is limited, hindering structure-based drug design efforts to target GC-1 for the treatment of cardiovascular diseases. Subtle conformational changes are thought to propagate the NO-binding signal throughout the entire GC-1 heterodimer via the coiled-coil domain to re-orient the catalytic domain into an active conformation. To identify the structural elements involved in this signal transduction cascade, we optimized a cGMP-based luciferase assay that reports on heterologous GC-1 activity in *E. coli* and identified novel activating GC-1 mutations. These mutations belong to the dorsal flaps, dimer interface, and GTP-binding regions of the catalytic domain. We show that combinations of mutations from these different elements synergize to promote even greater activity. Our results suggest that the dorsal flaps play a central role in the activation mechanism by coupling the coiled-coil domain to the active site via a series of hot spots. Our results provide new mechanistic insights not only into the molecular

pathway for GC-1 activation but also for other members of the nucleotidyl cyclase family in general.

3.2. Introduction

Soluble guanylyl cyclase (GC-1) cyclizes guanosine 5'-triphosphate (GTP) into cyclic guanosine 3',5'-monophosphate (cGMP) which controls vasodilation and platelet activity.⁴⁴ Nitric oxide (NO) binding to the N-terminal heme cofactor increases cGMP production 100-200-fold, acting as a second messenger to regulate cardiovascular function. The predominant isoform of GC-1 is the $\alpha_1\beta_1$ heterodimer with each subunit composed of four domains: an N-terminal domain regulatory heme-nitric oxide/oxygen binding (HNOX) domain, followed by a Per-Arnt-Sim (PAS) domain, an extended coiled-coil (CC) domain, and a C-terminal guanylyl cyclase ($\alpha\beta\text{GC}^{\text{cat}}$) domain.¹⁶⁰ How the NO-binding event is transmitted from the N-terminal sensor domain to the catalytic domain remains unknown.

While there are several structures of domains homologous to those present in GC-1,^{57,81,82,84,161–163} only two structures of human $\alpha\beta\text{GC}^{\text{cat}}$ have been solved so far, both of which are in an inactive conformation.^{90,91} Despite extensive efforts to obtain an active $\alpha\beta\text{GC}^{\text{cat}}$ structure, our understanding of the mechanisms by which $\alpha\beta\text{GC}^{\text{cat}}$ transitions to an active conformation relies principally on comparisons with the homologous adenylyl cyclase catalytic domain (C1/C2) for which a wealth of structural and mutagenesis data is available.^{95,127,147,164–169} The activating events triggered by NO binding likely include a rearrangement of the two subunits to close the GTP-binding cleft.⁹⁰ Mass spectrometry, Small-Angle X-ray Scattering, and electron microscopy studies have suggested a possible assembly for the full-length

enzyme and generated new hypotheses regarding the mechanisms by which the NO signal is transmitted to the active site.^{85,87,117,156}

Contrary to adenylyl cyclase, only two activating mutations have been reported thus far in GC-1 and both are located in the catalytic domain. The α Cys595Ser mutation, located at the dimer interface, decreases K_m 10-fold compared to wild-type GC-1¹⁰⁵ and the β Met537Asn mutation, located on the dorsal flap, increases V_{max} 7-fold.¹⁰¹ Although the mechanism by which these mutations activate GC-1 remains unknown, we previously proposed that they modulate interfacial contacts to promote an optimal conformation of $\alpha\beta$ GC^{cat} for catalysis.⁹¹

Identification of novel additional activating mutations in the catalytic domain will allow us to determine amino acids and structural elements important for GC-1 activation. Here, we describe the design, optimization, and testing of a cGMP-based luciferase reporter assay to identify activating GC-1 mutations. This is the first time that such an assay has been designed to report on heterologous GC-1 activity in *E. coli*. By combining measurements of luciferase activity and extracellular cGMP/cAMP levels, we identified several novel activating mutations in the catalytic domain. Combination of some of these mutations leads to synergism or antagonism, suggesting cross talk between various structural elements in the catalytic domain. Interestingly, our assay allows us to identify mutants that affect not only cGMP synthesis, but also the ATP cyclase activity of GC-1, and its substrate specificity. Based on our results, we propose that the NO signaling event is eventually communicated to the catalytic domain via hot spots that link the final helix-turn-helix motif of the coiled-coil domain to the active site. Importantly, targeting these hot

spots with small molecules may provide new strategies to rationally design novel GC-1 activators.

3.3. Materials and Methods

3.3.1. Materials

BL21(DE3) cells were purchased from Life Technologies. BL21(DE3) *cyaA*-cells were a kind gift from Dr. Mark Gomelsky (Univ. Wyoming). The pOPTXcGMPRE:LUC plasmid was a kind gift from Dr. Helen R. Irving (Monash Univ.). Antibiotics were used at the following final concentrations: ampicillin (Amp)- 35 µg/mL, kanamycin (Kan)- 50 µg/mL, chloramphenicol (Chlor)- 35 µg/mL, spectinomycin (Spect)- 50 µg/mL.

3.3.2. Plasmids and Gene Construction

Codon-optimized human α GC-1 (Uniprot accession code Q02108, residues 1-690) and β GC-1 (Uniprot accession code Q02153, residues 1-619) DNAs were purchased from BioBasic. The α GC-1 polypeptide is N-terminally tagged with 6xHis-thioredoxin-6xHis-SUMO and cloned into pCDF-Duet (Spect^r, Novagen) MCS-1 using restriction sites NcoI and EcoRI; the β GC-1 polypeptide is N-terminally tagged with monomeric OCR (Mocr)¹⁷⁰ and cloned into pCDF-Duet MCS-2 using restriction sites NdeI and XhoI. Because the BL21(DE3) *cyaA*-cells are also spectinomycin resistant, we replaced the Spect^r gene present in the pCDF-Duet vector with the Amp^r gene from the pET-21a vector. To accomplish this, we introduced flanking BmtI and BsaAI restriction sites to the Amp^r gene in the pET21a vector by

site-directed mutagenesis. BmtI and BsaAI restriction enzymes and a Rapid DNA Ligation Kit (Sigma-Aldrich) were used to remove the Spect^r gene from pCDF-Duet and insert the Amp^r gene. The final plasmid, which contains both GC-1 polypeptide chains, is denoted pCDF- $\alpha\beta$ GC1 (Amp^r). We also generated the pCDF- α GC1 (Amp^r) plasmid, which only contains the α GC-1 polypeptide in MCS-1, as a negative control. Mutations were introduced using site-directed mutagenesis (Agilent). All sequences were confirmed by sequencing (GENEWIZ).

3.3.3. Cell Growth Conditions

Our first trials were done with BL21(DE3) cells. These cells were co-transformed with pOPTXcGMPRE:LUC, pGro7 (Takara Inc.), and pCDF- $\alpha\beta$ GC1 (Table 1) in a single transformation reaction, but failed to reproducibly yield colonies. Transforming BL21(DE3) *cyaA*- cells under these conditions failed to produce colonies altogether. To reproducibly obtain colonies, BL21(DE3) *cyaA*- cells (Spect^r) were first transformed with pOPTXcGMPRE:LUC, plated on LB agar plates supplemented with Kan, and made chemically-competent. We then co-transformed these cells with the compatible vectors pGro7 (Takara Inc.) and pCDF- $\alpha\beta$ GC1 (Table 1) and plated on LB agar plates supplemented with Kan, Chlor, and Amp. Overnight cultures grew at 37 °C, 225 RPM in Luria Broth (LB). The next day, 100 mL of Terrific Broth (TB) media were inoculated with 3 mL of overnight culture and grown at 37 °C, 225 RPM until Abs₆₀₀ reached ~0.2-0.4. Cells were cold shocked for 1 hour on ice and induced with 100 μ M isopropyl β -D-1-thiogalactopyranoside (IPTG) and 0.2% (w/v) arabinose and supplemented with 0.45 mM δ -aminolevulinic acid and 30 μ M ferric citrate. Induced cultures grew at 15 °C, 90 RPM for up to 72 hours.

Samples (1.5 mL) were collected and pelleted (4,000xg, 10 minutes, 4 °C) at various time points, and stored at -80 °C until further use.

3.3.4. Western Blot

We resuspended 1.5 mL cell pellets in a volume of SDS-PAGE loading buffer (60 mM Tris pH 6.8, 25% (v/v) glycerol, 2% (w/v) SDS, 5% (v/v) BME, and 0.2% (w/v) bromophenol blue) normalized to the Abs₆₀₀. Samples were incubated at 70 °C for 8 minutes and spun down (10,000xg, 10 minutes, 4 °C). We loaded 5 µL onto a 13% acrylamide gel along with 5 µL of Precision Plus Protein Standards (BioRad). Proteins were transferred to a nitrocellulose membrane (BioRad) and detected using Ponceau Red. Membranes were blocked using a 4% (w/v) milk solution and exposed to either rabbit anti-αGC-1 (residues 673-690, Sigma-Aldrich) or rabbit anti-βGC-1 (residues 605-619, Sigma-Aldrich) primary antibodies and goat anti-rabbit (BioRad) secondary antibodies coupled to alkaline phosphatase. Bands were revealed using NBT and BCIP reagents (Thermo Fisher).

3.3.4. Luciferase Assay

Cell lysates for the luciferase assay were prepared following the Promega protocol with slight modifications. The 1X Cell Culture Lysis Reagent (CCLR) was prepared according to the manufacturer's protocol, supplemented with 50 U/mL benzonase. To maximize the signal from luciferase activity in the cell lysate, we optimized the volume of cells that were harvested, as well as the volume of lysis buffer for resuspension. As a result, we resuspended 1.5 mL pellets in 100 µL of 100 mM K₂HPO₄ (pH 7.4) and 2 mM EDTA. Each sample received 300 µL of 1X CCLR.

Lysis was accomplished via mechanical disruption with glass beads and clarified at 10,000xg for 5 minutes at 4 °C.

Luciferase activity was measured in clarified cell lysates using a GloMax Multi+ Microplate Multimode Reader. We transferred 20 μ L of clarified lysate into a 96-well black bottom plate. We added 100 μ L of luciferin substrate (Promega) to each well and the signal was integrated over 10 seconds with a 2 second delay between wells. All samples were plated in triplicate and measured in two or more experimental replicates. All data were normalized to protein concentrations measured using the bicinchonic acid assay (Pierce). Background luciferase activity was measured from cells co-transformed with pOPTXcGMPRE:LUC, pGro7, and pCDF- α GC1 lacking the β GC-1 polypeptide (**Figure S1**).

3.3.5. cGMP/cAMP Immunoassays

Extracellular and intracellular cGMP and cAMP levels were measured at the 72 hours time point, using the Parameter Assay Kits (R&D Systems) following the manufacturer's protocol. We washed 1.5 mL cell pellets once in PBS (50 mM sodium phosphate (pH 7.5) and 0.5 M NaCl) and resuspended them in 280 μ L of lysis buffer (Cell Lysis Buffer-5, 1 mg/mL lysozyme, 25 U/mL benzonase, and 0.3 mM 3-isobutyl-1-methylxanthine). Lysis was accomplished with glass beads and clarified at 4,000xg for 10 minutes at 4 °C, and stored at -80 °C until further use.

All measurements of extracellular cGMP or cAMP required background subtraction. Background extracellular cGMP levels were measured in TB media. Background extracellular cAMP levels were measured from post-induction BL21(DE3) *cyaA*- cells co-transformed with pCDF- α GC1, pOPTXcGMPRE:LUC,

and pGro7, and grown at 15 °C, 90 RPM for 72 hours. All extracellular cyclic nucleotide concentrations were normalized to cell lysate protein concentrations measured using the bicinchonic acid assay (Pierce). The cGMP/cAMP signal was measured using a SpectraMax plate reader. All samples were plated in duplicate and measured in two or more experimental replicates.

3.3.6. Multi-Sequence Alignment

Alignment of adenylyl cyclase and guanylyl cyclase catalytic domains were performed using CLUSTAL Omega^{171,172} and viewed using ESPript.^{173,174}

3.3.7. Accession Numbers

Uniprot accession codes for *Homo sapiens* αGC-1 and βGC-1 are Q02108 and Q02153, respectively.

3.4. Results

3.4.1. Assay Promiscuity and Reduction of Background cAMP Signal

We designed and optimized a luciferase reporter assay that measures heterologous GC-1 activity in bacterial cells. For this assay, we co-transform *E. coli* cells with pCDF-αβGC1 (expressing heterodimeric GC-1 constructs), pGro7 (expressing GroEL/ES chaperones), and pOPTXcGMPRE:LUC (expressing Firefly luciferase)¹⁷⁵ plasmids (**Table 3.1**). Induction of GC-1 expression in the presence of GroEL/ES chaperones will produce cGMP, which in turn will induce expression of luciferase. Luciferase activity measurements will therefore be an indirect measure of

cGMP levels and GC-1 expression and activity in *E. coli*. We optimized multiple cell growth parameters including IPTG concentration, temperature, and growth time, as well as volumes of harvested sample and lysis buffer to perform the luciferase assay.

Table 3.1. List of plasmids for reporter assay. ^aOligopeptide transporter X cyclic guanosine 3',5'-monophosphate reporter gene: luciferase.

Plasmid Name	Gene	Promoter	Antibiotic Resistance	Origin of Replication
pOPTXcGMPRE:LUC ^a	Luciferase	<i>OPTXcGMPRE</i>	Kan ^r	pBR322
pGro7	GroEL/ES	<i>araB</i>	Chlor ^r	p15A
pCDF- α β GC1	α GC-1/ β GC-1	<i>T7</i>	Amp ^r	CloDF13
pCDF- α GC1	α GC-1	<i>T7</i>	Amp ^r	CloDF13

Previous characterization of the pOPTXcGMPRE:LUC plasmid demonstrated increased luciferase activity upon addition of a cell-permeable cGMP analog and to a lesser extent of a cell-permeable cAMP analog.¹⁷⁵ In BL21(DE3) cells transformed only with the pOPTXcGMPRE:LUC vector, we measured significant luciferase activity (**Figure 3.1**). This is most likely due to endogenous cAMP production, as *E. coli* cells do not produce significant cGMP levels.^{176,177} To reduce background luciferase activity, we tested BL21(DE3) cells lacking the *cyaA* gene, which encodes for endogenous adenylyl cyclase.^{178–180} Because these cells cannot produce cAMP, they are ideal hosts for expressing heterologous nucleotide cyclases and measuring exogenous cyclic nucleotides. We compared background luciferase activity in BL21(DE3) cells (either *cyaA*⁺ or *cyaA*⁻) in the absence of pCDF- $\alpha\beta$ GC1 and pGro7 (**Figure 3.1**). In the absence of endogenous adenylyl cyclase (*cyaA*⁻ cells), luciferase activity was ~90% lower than in cells with intact adenylyl cyclase (*cyaA*⁺ cells). To confirm that this decrease in luciferase activity was due to the loss of cAMP production, we measured extracellular cAMP levels in both cell lines, as previous work indicated *E. coli* secretes a majority of cyclic nucleotides into the cell culture media.¹⁷⁹ The BL21(DE3) *cyaA*⁺ cells secreted $1.72 \pm 0.35 \times 10^5$ pmol cAMP/mg protein while BL21(DE3) *cyaA*⁻ cells had no detectable cAMP amounts (**Table 3.2**). These results confirm that the OPTXcGMPRE promoter is sensitive to both cGMP and cAMP, and that endogenous cAMP levels can be effectively eliminated in BL21(DE3) *cyaA*⁻ cells.

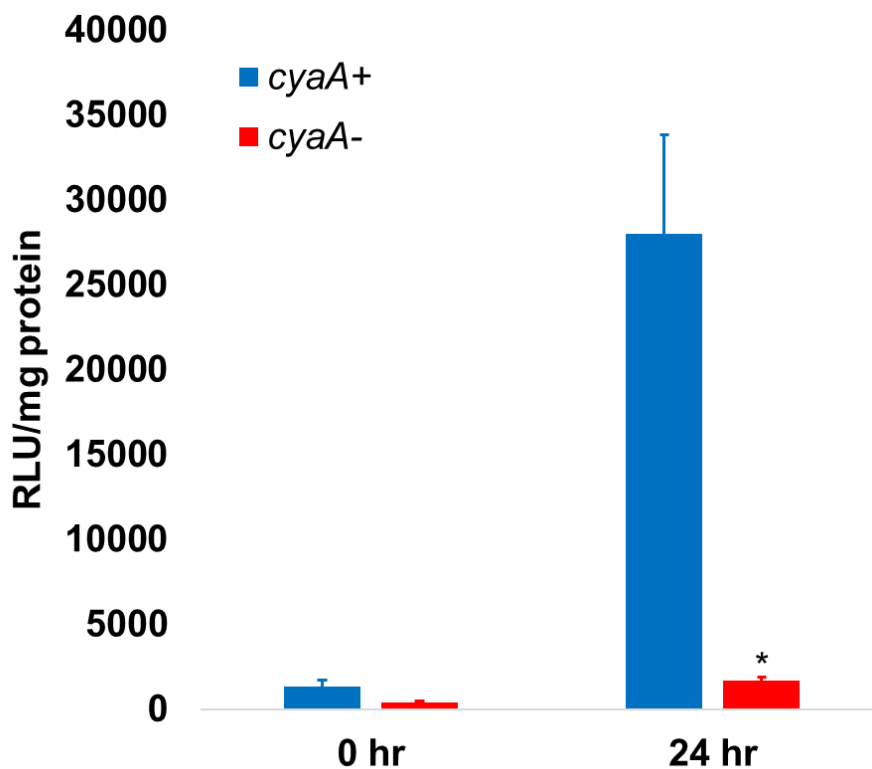


Figure 3.1. Luciferase activity from BL21(DE3) (*cyaA*⁺) and BL21(DE3) *cyaA*-deficient (*cyaA*⁻) cells transformed with pOPTXcGMPRE:LUC. Data represent an average of three or more experiments plated in triplicate. Error bars represent the standard error of the mean. Statistical significance between *cyaA*⁺ and *cyaA*⁻ cells at 24 hours was analyzed using Student's t-test (* $p < 0.05$).

Table 3.2. Extracellular cAMP levels from BL21(DE3) *cyaA*⁺ and BL21(DE3) *cyaA*⁻ (*cyaA* deficient) cells. Samples were plated in duplicate and averaged from three experimental replicates. Error represents the standard error of the mean from three or more independent experiments. ^aNot detectable.

Cells	pmol cAMP/mg protein ($\times 10^5$)
BL21(DE3) <i>cyaA</i> ⁺	1.72 \pm 0.35
BL21(DE3) <i>cyaA</i> ⁻	N/D ^a

3.4.2. Luciferase Activity Induction by Wild-type GC-1 and Inhibition by Inactive GC-1 Variants

To test the feasibility of the novel reporter assay, we measured luciferase activity in BL21(DE3) *cyaA*⁻ cells co-transformed with wild-type pCDF- $\alpha\beta$ GC1, pGro7 and pOPTXcGMPRE:LUC vectors. Samples were collected at several time points and luciferase activity was measured in clarified cell lysates. Detectable activity was defined as samples with relative light units (RLU)/mg of protein levels greater than background (**Supplementary Fig. A1**). Luciferase activity was detectable in these cells only 72 hours post induction (**Table 3.3** and **Supplementary Fig. A3**). To confirm these findings, we determined intracellular (cell lysates) and extracellular (supernatant) cGMP levels 72-hour post-induction, which showed elevated cGMP levels mostly in the supernatant (**Table 3.4**). The cGMP measurements support the luciferase assay results and demonstrate the utility of the reporter assay.

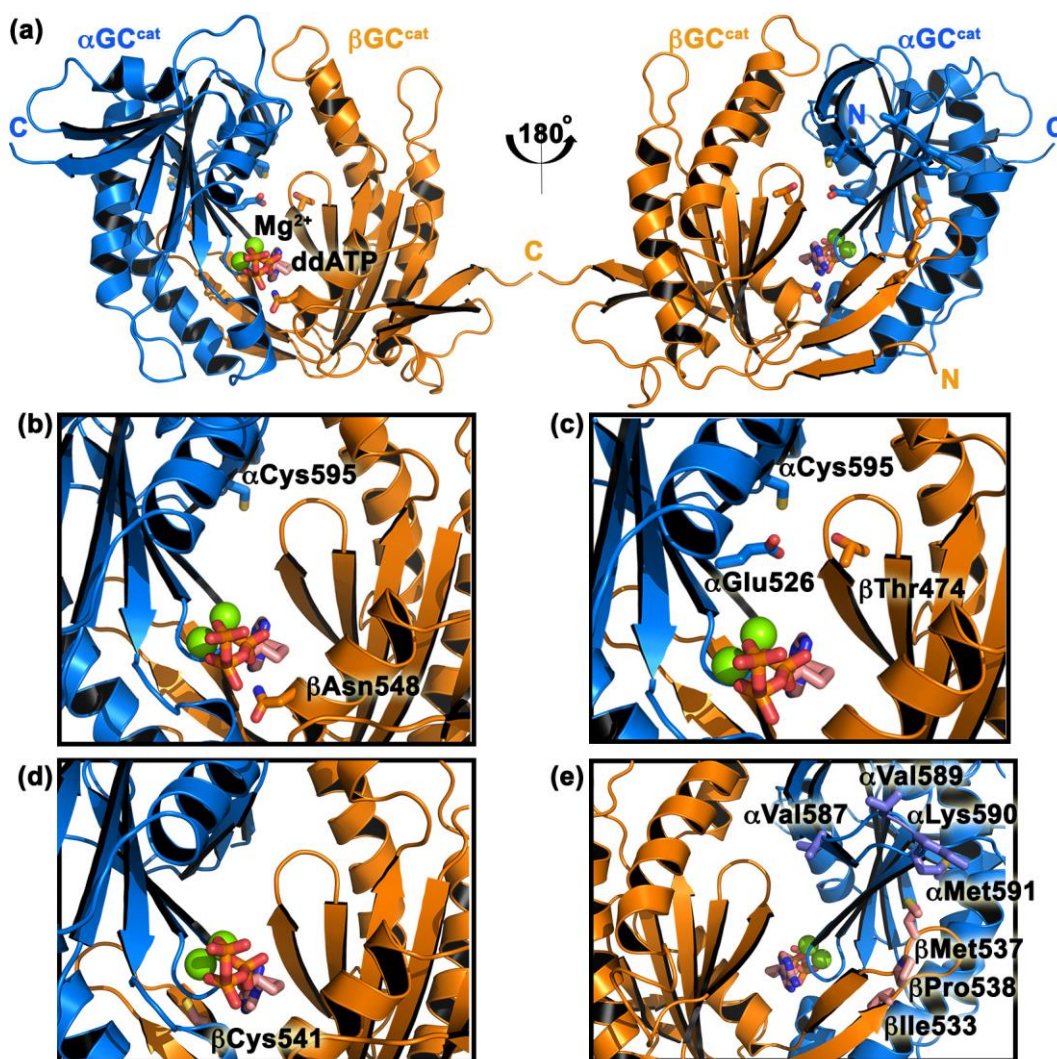


Figure 3.2. Amino acids in the GC-1 catalytic domain targeted for mutagenesis. (a) Ventral (left) and dorsal (right) sides of the GC-1 catalytic domain ($\alpha\beta\text{GC}^{\text{cat}}$) in the predicted activated conformation with Mg^{2+} and dideoxy-ATP (ddATP) bound in the active site. (b) Amino acids αCys595 and βAsn548 were mutated to inactivate GC-1. (c) Amino acids αCys595 , αGlu526 , and βThr474 were predicted to form an interfacial hydrogen-bond network ¹¹. (d) βCys541 in the substrate-binding pocket was proposed to modulate substrate specificity.³⁵ (e) Amino acids from both dorsal flaps were mutated.

Table 3.3. Luciferase activity for wild-type and mutant GC-1. Luciferase assay was measured in cell lysates from cell pellets collected after 72 hour of cell growth and were plated in triplicate. Error represents the standard error of the mean from three or more independent experiments. Statistical significance between wild-type and mutant GC-1 samples was calculated using the Student's *t*-test (**p* < 0.05; ***p* < 0.01; ****p* < 0.001). ^aNot detectable.

Sample	Luciferase activity (RLU/mg protein)	Fold-increase	<i>p</i> -value
Wild-type αβGC-1	274.0 ± 86.2	1.0	
<i>α-flap variants</i>			
αVal587Ile/αVal589Thr	1219.9 ± 228.6	4.5	*
αVal587Ile/αVal589Thr/αLys590Arg	667.0 ± 164.5	2.4	
αMet591Asn	1264.2 ± 206.4	4.6	*
<i>β-flap variants</i>			
βIle533Met	1297.7 ± 245.2	4.7	*
βMet537Asn	738.1 ± 131.9	2.7	
βPro538Gln	1244.1 ± 330.9	4.5	
<i>αβ-flap variants</i>			

α Val587Ile/Val589Thr/Lys590Arg/ β Met537Asn	1062.4 ± 72.0	3.9	***
$\alpha\beta$ flap deletions	1687.8 ± 101.4	6.2	***
α Met591Asn/ β Met537Asn	2623.0 ± 495.6	9.6	*
<i>Interfacial variants</i>			
α Cys595Ser	579.0 ± 134.5	2.1	
α Cys595Ser/ β Thr474Val	2667.8 ± 462.5	9.7	**
β Thr474Val	1250.4 ± 311.0	4.6	
β Thr474Met	1726.4 ± 380.5	6.3	**
α Cys595Ser/ α Glu526Ala	3366.0 ± 1315.1	12.3	
α Cys595Tyr	676.7 ± 4.9	2.5	*
<i>Interfacial/β-flap variants</i>			
α Cys595Ser/ β Met537Asn	964.7 ± 245.6	3.5	
α Cys595Ser/ β Met537Asn/ β Pro538Gln	1925.0 ± 240.7	7.0	**
α Cys595Ser/ β Pro538Gln	439.0 ± 123.6	1.6	
<i>GTP cleft variants</i>			

β Asn548Trp	N/D ^a	---	
β Cys541Gly	1801.7 ± 374.2	6.6	*
<i>Interfacial/GTP cleft variants</i>			
β Cys541Gly/ α Cys595Ser	2059.9 ± 190.3	7.5	***
<i>Interfacial/β-flap/GTP cleft variants</i>			
α Cys595Ser/ β Met537Asn/ β Asn548Trp	N/D ^a	---	
β Cys541Gly/ α Cys595Ser/ β Met537Asn	1957.9 ± 344.0	7.1	**
β Cys541Gly/ α Cys595Ser/ β Met537Asn/ β Pro538Gln	297.1 ± 70.0	1.1	

Table 3.4. Extracellular cGMP and cAMP levels from wild-type and mutant GC-1 samples. The cGMP and cAMP levels were measured in the extracellular supernatant after 72 hours of cell growth and were plated in duplicate. Error represents the standard error of the mean from three or more independent experiments. ^aNot detectable.

Sample	pmol cGMP/ mg protein ($\times 10^3$)	Fold-increase	pmol cAMP/ mg protein ($\times 10^3$)	Fold-increase
α GC-1 (- β GC-1)	N/D ^a		N/D ^a	
Wild-type $\alpha\beta$ GC-1	1.87 ± 0.5	1.0	0.59 ± 0.1	1.0
<i>α-flap variants</i>				
α Val587Ile/ α Val589Thr	3.78 ± 0.9	2.0		
α Val587Ile/ α Val589Thr/ α Lys590Arg	3.68 ± 1.1	2.0		
α Met591Asn	3.72 ± 0.5	2.0		
<i>β-flap variants</i>				
β Ile533Met	2.85 ± 1.4	1.5		
β Met537Asn	4.15 ± 0.9	2.2		
β Pro538Gln	2.67 ± 0.8	1.4		

$\alpha\beta$ -flap variants

α Val587Ile/Val589Thr/Lys590Arg/ β Met537Asn	3.53 ± 2.0	1.9
$\alpha\beta$ flap deletions	3.21 ± 0.8	1.7
α Met591Asn/ β Met537Asn	4.47 ± 1.2	2.4

Interfacial variants

α Cys595Ser	12.15 ± 2.0	6.5		
α Cys595Ser/ β Thr474Val	6.44 ± 1.3	3.4		
β Thr474Val	3.85 ± 1.4	2.1		
β Thr474Met	4.43 ± 0.5	2.4		
α Cys595Ser/ α Glu526Ala	9.41 ± 1.5	5.0		
α Cys595Tyr	0.50 ± 0.3	0.3	1.29 ± 0.4	2.2

Interfacial/ β -flap variants

α Cys595Ser/ β Met537Asn	19.45 ± 4.1	10.4
α Cys595Ser/ β Met537Asn/ β Pro538Gln	9.16 ± 2.3	4.9
α Cys595Ser/ β Pro538Gln	2.02 ± 0.8	1.1

GTP cleft variants

β Asn548Trp	N/D ^a			
β Cys541Gly	4.12 ± 1.2	2.2	4.48 ± 1.3	7.6

Interfacial/GTP cleft variants

β Cys541Gly/ α Cys595Ser	24.78 ± 1.4	13.2	3.69 ± 1.5	6.2
---------------------------------------	-----------------	------	----------------	-----

Interfacial/ β -flap/GTP cleft variants

α Cys595Ser/ β Met537Asn/ β Asn548Trp	1.54 ± 0.3	0.8		
β Cys541Gly/ α Cys595Ser/ β Met537Asn	28.6 ± 4.6	15.3	3.13 ± 0.8	5.3
β Cys541Gly/ α Cys595Ser/ β Met537Asn/ β Pro538Gln	9.99 ± 1.7	5.3	1.79 ± 0.4	3.0

To determine whether we could specifically reduce luciferase activity by inactivating GC-1, we made the α Cys595Tyr GC-1 variant, which was previously reported to reduce GC-1 catalytic activity (**Figure 3.2b**).¹⁰¹ Surprisingly, cells transformed with this variant showed luciferase activity 2-fold higher than cells transformed with wild-type GC-1 (**Table 3.3** and **Supplementary Fig. A3**). However, we showed that these cells displayed 70% reduced extracellular cGMP levels, in good agreement with previous studies. We hypothesized that the remaining luciferase activity may be caused by weak adenylyl cyclase activity of GC-1. Indeed, extracellular cAMP measurements of cells transformed with the α Cys595Tyr GC-1 variant were 2.2-fold higher than those transformed with wild-type GC-1, suggesting that the observed increase in luciferase activity was due to elevated adenylyl cyclase activity (**Table 3.4**). To obtain further GC-1 inactivation, we made the novel β Asn548Trp GC-1 variant (**Figure 3.2b**). Based on the $\alpha\beta$ GC^{cat} crystal structure (PDB code 4NI2) and comparison with adenylyl cyclase,^{90,91} β Asn548 is predicted to interact with the nucleotide ribose group. We expected that mutation of β Asn548 into a bulky Trp would hinder nucleotide binding and inhibit catalytic activity. Indeed, cells expressing β Asn548Trp GC-1 had no detectable luciferase activity or extracellular cGMP levels compared to those expressing wild-type GC-1 (**Tables 3.3** and **3.4**), despite similar expression as shown by Western blot (**Supplementary Fig. A2a**). Together, these results confirm that the luciferase assay specifically reports on heterologous GC-1 activity, and that the cGMP/cAMP production can be deconvoluted with a follow-up ELISA assay.

3.4.2.1. Validation of pOPTXcGMPRE:LUC Plasmid with Cell-permeable cGMP Analog

The pOPTXcGMPRE:LUC plasmid was designed to report on intracellular cGMP levels in *E. coli* and screen for putative guanylyl cyclases.¹⁷⁵ When the cell-permeable analogs of cGMP and cAMP, 8-bromoguanosine 3',5'-cyclic monophosphate (8-Br cGMP) and dibutyryl cAMP, respectively, were added to *E. coli* BL21(DE3) cells transformed with the reporter plasmid, a dose-dependent increase in luciferase activity was measured. However, in our hands, we observed no increase in luciferase activity upon addition of 8-Br cGMP (see Discussion).

3.4.2.2. Design of Inactive GC-1 Variants

To further validate the luciferase reporter assay, we made several inactivating mutations in the GTP-binding cleft and measured luciferase activity and extracellular cGMP levels for comparison with GC-1 wild-type. The α Arg574Ala mutation was predicted to disrupt GTP binding based on structural alignment with the activated C1/C2 domain from AC.^{90,91,160} For cells, transformed with this variant, luciferase activity was lower than cells transformed with wild-type GC-1 at the 72 hour time point (**Figure 3.3**) and extracellular cGMP levels were ~60% reduced, confirming inhibition of GC-1 activity.

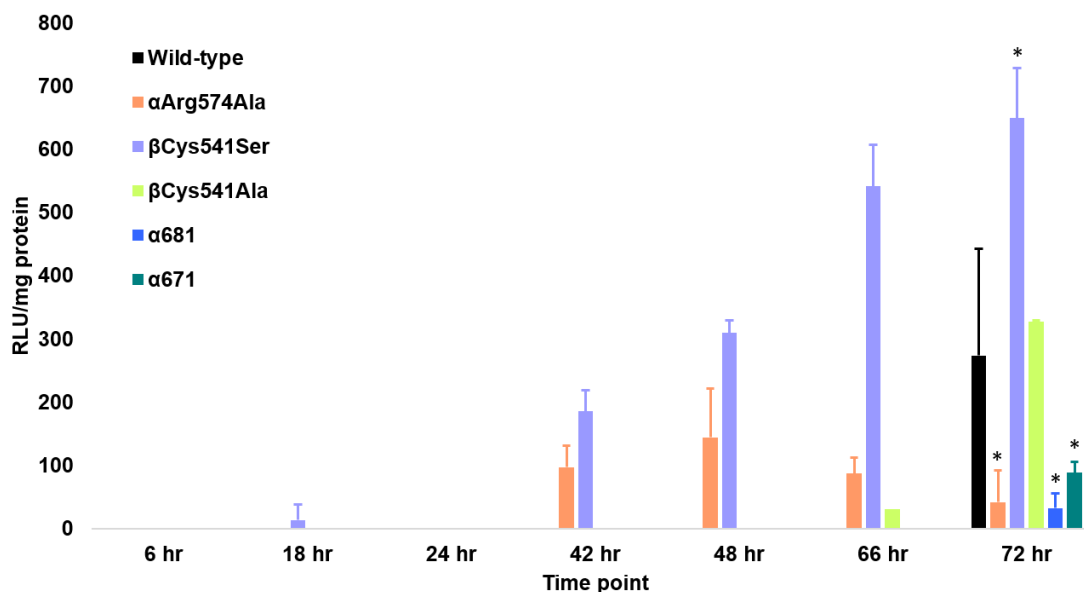


Figure 3.3. Luciferase activities induced by inactive GC-1 variants. Data represent an average of one or more experiments. In cases of one experiment, data represent an average of three technical replicates. Statistical comparison between wild-type and mutant GC-1 at the 72 hour time point was analyzed using the Student's *t* test (* $p < 0.001$). Error bars represent a 95% confidence interval.

The β Cys541Ser mutation has been previously reported to inactivate GC-1, due to the potential role of this residue in substrate binding.^{104,105} Surprisingly, for cells transformed with this variant, luciferase activity was greater than for cells transformed with wild-type GC-1 (**Figure 3.3**). However extracellular cGMP levels were lower for cells transformed with the mutant GC-1, supporting inhibition of GC-1 (**Table 3.5**). The reason in this discrepancy may be due to the promiscuity of the OPTX promoter. In addition to cGMP, this promoter was shown to respond to cAMP (see **section 3.4.1**). Thus, we hypothesized that β Cys541Ser GC-1 also displays ATP cyclase activity, resulting in activation of luciferase expression.¹²⁸ Meanwhile, cells transformed with the β Cys541Ala variant showed no significant difference in luciferase activity in comparison with GC-1 wild-type (**Figure 3.3**).

Table 3.5. Extracellular cGMP from wild-type and inactive GC-1 variants.

^aSamples were plated in duplicate and averaged from two or more experimental replicates. Error represents a 95% confidence interval. ^bNot detectable. ^cNot measured.

Sample	pmol cGMP/mg protein ^a	Fold-increase
α GC-1 ($-\beta$ GC-1)	N/D ^b	---
Wild-type $\alpha\beta$ GC-1	$(1.87 \pm 0.90) \times 10^3$	1.0
α Arg574Ala $\alpha\beta$ GC-1	$(0.67 \pm 0.62) \times 10^3$	0.4
β Cys541Ser $\alpha\beta$ GC-1	$(1.46 \pm 0.80) \times 10^3$	0.8
β Cys541Ala $\alpha\beta$ GC-1	$(1.50 \pm 1.6) \times 10^3$	0.8
α 681 $\alpha\beta$ GC-1	N/M ^c	N/M ^c
α 687 $\alpha\beta$ GC-1	N/M ^c	N/M ^c

Lastly, we sought to further characterize C-terminal truncations of the α GC-1 polypeptide as previous work from our lab¹⁸¹ lead us to hypothesize that the conserved 30 amino-acid C-terminal of α GC-1 stabilize the enzyme. We deleted 10 and 20 amino acids from the C-terminus (α 681 and α 671, respectively). For cells transformed with these variants, luciferase activity was almost completely abolished (**Figure 3.3**), supporting our hypothesis for an auto-regulatory role of the α GC-1 C-terminal tail.

3.4.3. Variants Along Catalytic Domain Dorsal Flaps Modulate GC-1 Activity

To determine the dynamic range of the assay, we tried to activate GC-1 by adding various NO donors. However, no increase in luciferase activity was observed, suggesting that GC-1 was not activated. This is most likely due to the presence of the Mocr tag at the N-terminus of the β GC-1 subunit, which abolished NO-induced activation but maintained basal activity, as observed previously.¹⁵² Consequently, we

transformed cells with a known activating GC-1 variant¹⁰¹ for which we expected to see an increase in luciferase activity. Indeed, cells expressing the β Met537Asn GC-1 variant, which is located on the dorsal flap of the β GC^{cat} subunit (**Figure 3.2e**), showed increased luciferase activity at multiple time points (**Table 3.3** and **Supplementary Figs. A4**). In contrast, luciferase activity was undetectable for cells expressing wild-type GC-1 except at the 72-hour time point. Cells expressing the activating variant had 2.7-fold greater luciferase activity and 2.2-fold greater extracellular cGMP levels than those expressing wild-type GC-1 at the 72-hour time point (**Table 3.4**). While the increase in luciferase activity may seem modest, it is significant (p -value is 0.054). Additionally, the results of the luciferase activity measurements match those obtained for cGMP levels. These results validate the reporter assay in detecting activating mutations in GC-1. Thus, we set out to identify other potential activating residues in the GC-1 dorsal flaps.

To determine whether residues in the dorsal flap of the α GC^{cat} subunit may be activating, we made the α Met591Asn GC-1 variant, which is homologous to β Met537Asn (**Figure 3.2e**). Cells expressing this variant also displayed luciferase activity at multiple time points. At the 72-hour time point, these cells showed 4.4-fold greater luciferase activity and 2.0-fold higher cGMP levels than those expressing wild-type GC-1 (**Tables 3.3** and **3.4**). We also designed the double variant α Met591Asn/ β Met537Asn GC-1 to determine whether we could measure an additive effect from both mutations on GC-1 activity. Although luciferase activity at the 72-hour time point was 10.7-fold higher than cells transformed with wild-type GC-1, we measured only 2.9-fold greater extracellular cGMP levels from the

α Met591Asn/ β Met537Asn variant (**Tables 3.3 and 3.4; Supplementary Fig. A4**). This suggests that the double mutant may also have increased cAMP activity. Thus, our luciferase reporter assay and cGMP measurements revealed the novel dorsal-flap α Met591Asn mutation as an activating GC-1 mutation, with an additive effect of the double α Met591Asn/ β Met537Asn mutation on GC-1 activity.

Next, we made other variants along the β GC^{cat} dorsal flap to determine the potential role of these residues in GC-1 activation (**Figure 2e**). In adenylyl cyclase, the Ile1010Met and Pro1015Gln variants in the C2 catalytic subunit both increased AC activity¹¹⁹. We made the corresponding mutations in GC-1 (β Ile533Met and β Pro538Gln) and measured luciferase activity and cGMP levels in cells expressing these mutants (**Tables 3.3 and 3.4**). We observed activity profiles similar to cells expressing β Met537Asn or α Met591Asn GC-1 variants with luciferase activity above the threshold level at multiple time points and moderately increased cGMP levels compared to cells expressing wild-type GC-1 (1.5-fold and 1.6-fold increase, respectively). These results support a general role of the catalytic domain dorsal flap residues in modulating GC-1 activity.

Alignment of α GC^{cat} and β GC^{cat} dorsal flaps amino-acid sequences revealed several differences between the two sequences (**Figure 3.4**). To mimic the β GC^{cat} dorsal flap, we made the double α Val587Ile/Val589Thr and the triple α Val587Ile/Val589Thr/Lys590Arg GC-1 variants (**Figure 3.2e**). We hypothesized that these mutations may increase contacts between the α GC^{cat} flap and the β GC^{cat} subunit to promote the “double flap-wrap” conformation observed for most AC structures.⁹¹ Cells expressing α Val587Ile/Val589Thr and

α Val587Ile/Val589Thr/Lys590Arg GC-1 displayed luciferase activity at multiple time points, and 4.5- and 2.5-fold greater luciferase activity than cells expressing GC-1 wild-type at the 72-hour time point, respectively. Cells expressing either the double or triple variant showed extracellular cGMP levels 2.0-fold greater than those expressing wild-type GC-1 (Tables 3.3 and 3.4). This activity was similar to what we observed with cells expressing other variants along the GC-1 dorsal flaps, which may indicate a regulatory role for the dorsal flaps.

	585	594
α GC-1 (<i>H. sapiens</i>) – Q02108	G V V C V K M P R Y	
β GC-1 (<i>H. sapiens</i>) – Q02153	G V I G Q R M P R Y	
α GC-1 (<i>M. musculus</i>) – Q9ERL9	G V V G V K M P R Y	
β GC-1 (<i>M. musculus</i>) – O54865	G V I G Q R M P R Y	
α GC-1 (<i>P. troglodytes</i>) – H2QQB9	G V V G V K M P R Y	
β GC-1 (<i>P. troglodytes</i>) – H2QQC0	G V I G Q R M P R Y	
α GC-1 (<i>M. sexta</i>) – O77105	G V V G K T M L K Y	
β GC-1 (<i>M. sexta</i>) – O77106	G V I G H R M P R Y	
α GC-1 (<i>C. elegans</i>) – O02298	G V V G I K M P R Y	
β GC-1 (<i>C. elegans</i>) – Q6DNF4	G V V G A K M P R Y	
α GC-1 (<i>L. africana</i>) – G3TED3	G V V G V K M P R Y	
β GC-1 (<i>L. africana</i>) – G3TED8	G V I G Q R M P R Y	
α GC-1 (<i>D. rerio</i>) – E7EZW5	G V V G V K M P R Y	
β GC-1 (<i>D. rerio</i>) – F1QNR4	G V I G Q R M P R Y	
α GC-1 (<i>A. mellifera</i>) – Q5W7P2	G V V G K K M P R Y	
β GC-1 (<i>A. mellifera</i>) – Q5UAF0	G V I G H R M P R Y	
α GC-1 (<i>O. curvnotus</i>) – Q7T041	G V V G V R M P R Y	
β GC-1 (<i>O. curvnotus</i>) – H2MZ22	G V I G Q R M P R Y	
AC-I C1 (<i>B. taurus</i>) – P19754	G V L G L R K W Q Y	
AC-I C2 (<i>B. taurus</i>) – P19754	G V I G A R R P Q Y	
AC-II C2 (<i>R. norvegicus</i>) – P26769	G V I G A Q K P Q Y	
AC-II C1 (<i>F. heteroclitus</i>) – A0A146MPW3	G V I G L R K W Q F	
AC-II C2 (<i>F. heteroclitus</i>) – A0A146MPW3	G V I G A R K P Q Y	
AC-III C1 (<i>A. colombica</i>) – A0A195AZI6	G V L G Q R Q W Q F	
AC-III C2 (<i>A. colombica</i>) – A0A195AZI6	G V I G A R K P H Y	
AC-IV C1 (<i>O. aries</i>) – W5QCS2	G V I G L Q K W Q Y	
AC-IV C1 (<i>X. tropicalus</i>) – L7N3L5	G V I G L Q K W Q Y	
AC-IV C2 (<i>X. tropicalus</i>) – L7N3L5	G V I G A Q K P Q Y	
AC-V C1 (<i>C. lupus</i>) – P30803	G V L G L R K W Q F	
AC-VI C1 (<i>S. scrofa</i>) – F1SPN5	G V L G L R K W Q F	
AC-VI C2 (<i>S. scrofa</i>) – F1SPN5	G V I G A R K P Q Y	
AC-VII C1 (<i>C. mydas</i>) – M7BJQ6	G V I G L R K W Q Y	
AC-VII C2 (<i>C. mydas</i>) – M7BJQ6	G V I G A R K P Q Y	
AC-VIII C1 (<i>G. gallus</i>) – A0A1D5PNE8	G V L G L R K W Q F	
AC-VIII C2 (<i>G. gallus</i>) – A0A1D5PNE8	G V I G A K K P Q Y	
AC-IX C1 (<i>F. catus</i>) – M3WWD4	G I L G M R R F K F	
AC-IX C2 (<i>F. catus</i>) – M3WWD4	G V I G T T K L L Y	
AC-IX C1 (<i>D. ficusphila</i>) – A0A1W4VGI4	G I V G T R R V K F	
AC-IX C2 (<i>D. ficusphila</i>) – A0A1W4VGI4	G V I G T S K L Y Y	

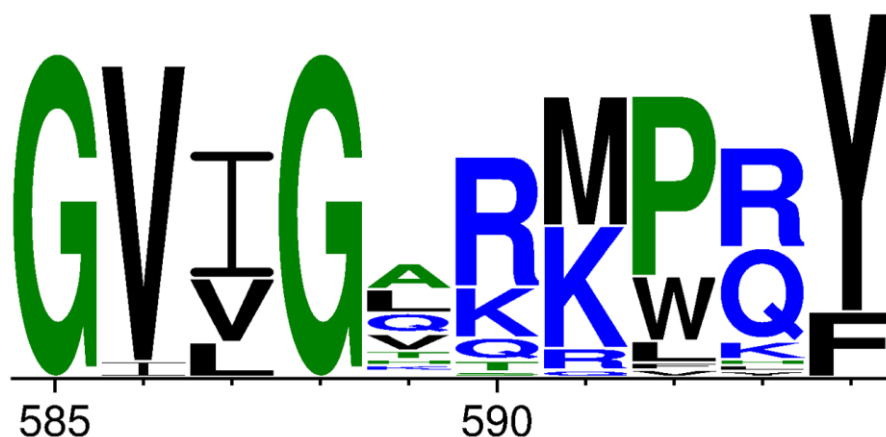


Figure 3.4. Alignment of guanylyl cyclase and adenylyl cyclase dorsal flaps. (Top) Alignment was generated with CLUSTAL Omega⁵⁰⁻⁵² and visualized with ESPrpt.^{40,41} Numbering corresponds to the dorsal flap sequence for α GC-1 (*H. sapiens*). Similar residues (red letters) are in blue boxes and invariant residues are highlighted in red. Residues in *H. sapiens* $\alpha\beta$ GC-1 that have been targeted for mutagenesis in this study are highlighted as follows: α Val587 (green), α Val587 (yellow), α Lys590 (pale green), α Met591 (pink), β Ile533 (blue), β Met537 (purple), and β Pro538 (teal). Uniprot accession codes are indicated for each sequence. (Bottom) Graphic representation of conserved residues generated with WebLogo.⁵³

Finally, our alignment of the dorsal flaps in GC and AC enzymes revealed two AC enzymes that completely lack dorsal flaps. As a result, we sought to determine the effect of removing both dorsal flaps on GC-1 activity. We replaced α GC^{cat} 588-592 and β GC^{cat} 534-538 residues with Ala-Gly dipeptides. Surprisingly, cells expressing these “flap-less” variants showed activities very similar to those expressing the dorsal flap variants described above. At the 72-hour time point, luciferase activity and extracellular cGMP levels were 6.2-fold greater and 1.7-fold greater, respectively, than cells expressing wild-type GC-1 (Tables 3.3 and 3.4). These results suggest that the mutations described above may alter the balance of contacts between the flaps and other GC-1 domains.

3.4.4. Variants at the Dimer Interface Activate GC-1 and Synergize with Dorsal Flap Variants

Previous reports showed that the GC-1 α Cys595Ser mutant displayed a 7-fold increase in GC-1 activity.¹⁰⁵ Accordingly, cells expressing α Cys595Ser GC-1 showed 1.8-fold increase in luciferase activity and 6.5-fold increase in cGMP levels compared to cells expressing wild-type GC-1. Surprisingly, cells expressing the double α Cys595Ser/ β Met537Asn GC-1 variant showed increased luciferase activity (3.5 fold) and dramatically increased cGMP levels (10.4 fold) over cells expressing wild-type GC-1 (**Tables 3.3** and **3.4**). This activation was almost completely abolished in cells expressing the triple α Cys595Ser/ β Met537Asn/ β Asn548Trp variant, showing the deleterious effect of the novel β Asn548Trp inactivating mutation, even in a super-active GC-1 background. These cells showed no detectable luciferase activity at any time point and 92% lower extracellular cGMP levels compared with cells transformed with the α Cys595Ser/ β Met537Asn GC-1 variant. Finally, we made the triple α Cys595Ser/ β Met537Asn/ β Pro538Gln GC-1 variant. Cells expressing this variant showed high luciferase activity (7.6-fold greater than cells expressing wild-type GC-1), but 2-fold lower extracellular cGMP levels compared to cells expressing the double α Cys595Ser/ β Met537Asn GC-1 variant. This result suggests a dampening effect of the β Pro538Gln mutation when combined to activating mutations.

To test our previous hypothesis regarding an interfacial hydrogen-bond network among residues α Cys595, α Glu526, and β Thr474,⁹¹ we made the β Thr474Val GC-1 variant (**Figure 2.2c**). Surprisingly, cells expressing this variant showed luciferase activity and cGMP levels 4.6-fold and 2.1-fold higher than cells

expressing wild-type GC-1, respectively (**Tables 3.3** and **3.4**). This result suggests that removal of the hydroxyl group is activating, contrary to what is expected if this residue participates in a hydrogen-bond network. To test whether hydrophobic interactions at the dimer interface may be beneficial for activity, we made the β Thr474Met GC-1 variant and measured increased luciferase activity and extracellular cGMP levels in comparison to the β Thr474Val variant. Together, these results suggest that increasing hydrophobic interactions at the dimer interface may constitute a novel mechanism for activating GC-1.

3.4.5. The β Cys541Gly Mutation Reduces Substrate Specificity and Synergizes with Other Variants to Increase GC-1 Activity

The β Cys541 residue was proposed to play a key role in substrate specificity and is conserved in guanylyl cyclases (**Figures 3.2d** and **3.4**).^{88,91,103,160} To test the role of this conserved residue, we made the β Cys541Gly GC-1 mutant. Cells expressing this variant showed luciferase activity and cGMP levels 6-fold and 2.2-fold greater than cells expressing wild-type GC-1, respectively. In addition, cells expressing this variant displayed extracellular cAMP levels 7.6-fold higher than cells expressing wild-type GC-1 (**Tables 3.3** and **3.4**). As a consequence, the β Cys541Gly GC-1 showed drastically reduced substrate specificity compared to wild-type GC-1 (cGMP/cAMP ratio of 0.9 and 3, respectively).

To identify potential synergy between multiple mutations, we combined the substrate-binding cleft β Cys541Gly mutation with activating mutations in the dimer interface and dorsal flaps. Cells expressing the double α Cys595Ser/ β Cys541Gly GC-1 variant displayed luciferase activity and cGMP levels 7.5-fold and 13.2-fold greater

than cells expressing wild-type GC-1, respectively. Cells expressing the triple α Cys595Ser/ β Cys541Gly/ β Met537Asn GC-1 variant showed luciferase activity and cGMP levels 7.1-fold and 15.3-fold higher than cells expressing wild-type GC-1, making it the highest-activity variant so far in this study. Interestingly, cells expressing either the α Cys595Ser/ β Cys541Gly or the α Cys595Ser/ β Met537Asn/ β Cys541Gly GC-1 variant had slightly reduced extracellular cAMP compared to the single β Cys541Gly variant (5.3- and 6.2-fold, respectively). These cells showed substrate specificity for GTP exceeding that of wild-type GC-1, despite the β Cys541Gly mutation (**Tables 3.3** and **3.4**). Finally, cells expressing the quadruple α Cys595Ser/ β Met537Asn/ β Pro538Gln/ β Cys541Gly GC-1 variant showed luciferase activity and cGMP levels 1.1-fold and 5.9-fold greater than cells expressing wild-type GC-1. This phenotype is consistent with what we observed before, confirming a dampening effect induced by the β Pro538Gln mutation when combined with other mutations.

3.5 Discussion

While the mechanism by which NO-binding may promote a series of activating conformational changes from the N-terminal HNOX domain to the C-terminal cyclase domain is unknown, we have developed a novel system to systematically define this mechanism of activation. Using a luciferase reporter assay, mutagenesis, and extracellular cGMP/cAMP measurements, we have identified and characterized multiple novel activating variants of the GC-1 catalytic domain. Interestingly, we have also measured a synergistic effect with several combinations of variants. Our results suggest novel mechanisms that tune GC-1 activity using residues

in three discreet locations of the catalytic domain: (i) dorsal flaps, (ii) the dimer interface, and (iii) the substrate-binding cleft. We propose that these residues couple the NO-induced activation signal from the penultimate coiled-coil domain to the active site of the catalytic domain to increase GC-1 activity.

3.5.1. A Luciferase Reporter Assay for Heterologous GC-1 Activity in *E. coli*

We designed, optimized, and validated a luciferase assay to report on heterologous GC-1 activity in bacterial cells. To our knowledge, this is the first time that a bacterial reporter assay is used to identify mutations in GC-1 that affect its activity.

First, we showed that the plant OPTXcGMPRE promoter for luciferase is not specific for cGMP. We measured high luciferase activity in BL21(DE3) cells even in the absence of the pCDF- $\alpha\beta$ GC1 plasmid, suggesting that either cGMP is present in *E. coli* cells, or that the promoter responds to other nucleotides, as was proposed previously.¹⁷⁵ To resolve this issue, we used BL21(DE3) *cyaA*⁻ cells,¹⁷⁹ where the gene encoding for endogenous adenylyl cyclase (*cyaA*) is deleted, and showed that background luciferase activity was dramatically reduced. Using cAMP and cGMP immunoassays, we confirmed that these extracellular cyclic nucleotides were undetectable in BL21(DE3) *cyaA*⁻ cells in the absence of the GC-1 expression vector. The residual luciferase activity in BL21(DE3) *cyaA*⁻ cells transformed with pOPTXcGMPRE:LUC alone is then likely due to cyclic nucleotides present in the cell culture media. It is also possible that the plant OPTXcGMPRE promoter responds to metabolites other than cGMP/cAMP that could be present inside the cell or in the culture media, as the exact mechanism of action of this plant promoter in

bacterial cells is not known.^{175,182} Our attempts to use minimal media to completely eliminate background luciferase activity were unsuccessful. Instead, we determined a background threshold for luciferase activity in the presence of pGro7 and the pCDF- α GC1 plasmid, which lacks the β GC-1 polypeptide. This background was subtracted from all subsequent luciferase activity measurements to reveal heterodimeric GC-1 constructs with cyclase activity.

Second, for cells transformed with wild-type GC-1 and GroEL/ES chaperone vectors, luciferase activity was only detectable after three days of growth post-induction. In these cells, we measured significant extracellular cGMP levels and only marginal extracellular cAMP levels.

Third, two inactivating GC-1 mutations were used to further validate the assay. Cells transformed with the inactivating α Cys595Tyr GC-1 mutant displayed diminished guanylyl cyclase activity, as shown previously.¹⁰¹ However, we showed that this mutant also had increased adenylyl cyclase activity, which likely caused the increased luciferase activity. How this substitution modifies GC-1 substrate specificity is not clear, but it is possible that the bulky Tyr residue at the dimer interface modifies the nearby GTP-binding pocket to favor ATP binding instead. GC-1 was shown to have broader substrate specificity than originally thought¹⁰⁶ and our assay allows us to identify mutations that affect GC-1 substrate preference (see below). Additionally, we made the novel β Asn548Trp inactivating variant. Cells transformed with this variant had no detectable luciferase activity or extracellular cGMP levels.

Overall, our results confirm that *E. coli* secretes the majority of cyclic nucleotides and validate the luciferase assay, whereby luciferase activity measurements indirectly report on heterologous GC-1 expression and its nucleotidyl activity in *E. coli*.

3.5.2. Multiple Catalytic Domain Structural Elements Control GC-1 Activity

We and others have defined the key structural elements of the cyclase domain as the dorsal flaps, dimer interface, and substrate-binding region (**Figure 3.2**).^{90,91,101,103,105,183} Our luciferase assay and extracellular cGMP measurements allowed us to identify several novel activating mutations along both dorsal flaps and at the dimer interface of the GC-1 catalytic domain. In addition, our sequence alignment of the dorsal flaps from adenylyl cyclases and guanylyl cyclases revealed that these flaps are well conserved, allowing us to identify a consensus sequence. We measured a synergistic effect by combining dorsal flaps, dimer interface, and substrate-binding region variants, leading us to propose a mechanism by which coupling of these different structural elements allows the signal to propagate from the NO-sensing domain to the catalytic domains to modulate GC-1 activity.

3.5.2.1. Dorsal Flaps Allosterically Modulate GC-1 Activity

Our previous x-ray structure of the heterodimeric catalytic domains from human GC-1 revealed the flexibility and asymmetric conformations of the dorsal flaps (PDB code 4NI2). While the β GC^{cat} dorsal flap (residues 531-540) wrapped onto the adjacent catalytic subunit, the α GC^{cat} dorsal flap (residues 585-594) was flipped out. The exact role of the dorsal flaps in GC-1 activation is unknown,

however one of the only two activating mutations known thus far belongs to the β GC^{cat} dorsal flap. The β Met537Asn mutation was shown to render GC-1 constitutively active by increasing its basal V_{max} .²⁶ We previously hypothesized that this structural element is a key modulator of the orientation of the catalytic subunits necessary for catalytic activity.¹¹ Our multi-sequence alignment using the catalytic domains of GC-1 and AC from multiple species reveals unique features of these dorsal flaps. While the catalytic domains of GC-1 and AC share limited sequence identity, the dorsal flaps are well conserved and contain the consensus sequence Gly-Val-Ile-Gly-X₅-Tyr.^{40,41} Of all the sequences, *Mycobacterium tuberculosis* AC has the smallest dorsal flaps containing only an Arg-Ala-Gly tripeptide,¹⁴ while the C2 subunit from *Ovis aries* AC-IV lacks a dorsal flap altogether. The available structure of the homodimeric *M. tuberculosis* AC in its activated conformation (PDB code 1Y11)¹⁴ suggested that docking of the coiled-coil region from the N-terminal regulatory domain close to the catalytic domain core may be permitted by the short dorsal flaps. However, several structures of catalytic domains from AC and homologs reveal a different arrangement.^{15–17,42} These proteins all contain dorsal flaps similar in sequence to GC-1. However, the dorsal flaps are more structured than the GC-1 flaps and all present the double “flap-wrap” conformation, likely due to the presence of the helical regions preceding the catalytic domains in these structures. By packing snugly onto the adjacent catalytic subunit, these flaps still allow tight contacts of the catalytic subunits with the preceding helix-turn-helix motif of the coiled-coil domain thought to transmit the activation signal to the active site. In *Beggiatoa* sp. AC, these

dorsal flaps were proposed to change conformation during activation, thus promoting conformational changes of the catalytic center.¹⁶

To unravel the potential role of these flaps in GC-1 activation, we made a series of mutations in both flaps. First, the luciferase assay and extracellular cGMP levels measurements confirmed that the β Met537Asn mutation is activating and further validated the assay for the identification of gain-of-function GC-1 variants. Second, two other mutations in the β GC-1 dorsal flap, β Ile533Met and β Pro538Gln, also resulted in increased activity. Similarly, mutations in the α GC^{cat} dorsal flap, including α Met591Asn, which mimics the β Met537Asn mutation, and the double α Val587Ile/Val589Thr and triple α Val587Ile/Val589Thr/Lys590Arg GC-1 mutants all yielded increased GC-1 activity. Third, we mutated both flaps in GC-1 to Ala-Gly dipeptides and showed that cells transformed with this double mutant displayed luciferase activity and cGMP levels similar to the above flap mutants. These results reveal novel activating mutations and suggest that the dorsal flaps are important for GC-1 activation.

In the absence of a structure for full-length GC-1, we generated a model for residues β 382-607 and α 442-659 based on the homologous CyasOL structure (PDB code 5O5K), which contains a helix-turn-helix motif at the end of the preceding coiled-coil domain.⁴³ The sequence identity between CyasOL residues 204-436 and GC-1 is 33% for α 442-661 and 36% for β 382-607. The resulting model suggests a possible assembly for the coiled-coil domain and the catalytic domain in GC-1 (**Figure 3.5a**) that is compatible with previous electron microscopy and mass spectrometry studies.²²⁻²⁴ In particular, the model shows the central role of the dorsal

flaps in connecting the helical domain to the active site, and suggests that the “flipped-out” conformation of the $\alpha\text{GC}^{\text{cat}}$ dorsal flap in our previous structure is incompatible with the proposed assembly. Residues βIle533 and αVal587 are located at the interface with the adjacent catalytic subunit (**Figure 3.5b**) and their mutation into larger hydrophobic amino acids may stabilize the nearby hydrophobic pocket, as proposed before.³⁴ In contrast, βPro538 and αLys590 are located at the potential interface with the adjacent helical domain, and their mutation could alter interactions between these structural elements. Finally, residues βMet537 , αVal589 , and αMet591 are all sandwiched between the catalytic and helical domains, and their mutations into hydrogen-bonding amino acids could modify the interface between these domains as well as the active site conformation (**Figure 3.5b**). Overall, our results show that altering the balance of interactions between the dorsal flaps and the helical domain on one side, and the dorsal flaps and the catalytic domains on the other side, either by mutations or deletion of the flaps leads to GC-1 activation. This strongly suggests a key allosteric regulatory role for the dorsal flaps in transmitting conformational changes from the helical domain to the catalytic center. Previous studies proposed that NO-induced activation could occur via conformational changes mediated by the helical domain.²³ In particular the dorsal flap in $\alpha\text{GC-1}$, as well as the helix-turn-helix motif preceding the catalytic domain in both subunits showed deuterium exchange rates that were affected by NO addition, suggesting their involvement in the signal transduction cascade. Additionally, comparison of the conformation of the helix-turn-helix motif in various AC structures suggested possible differences depending on the presence of bound nucleotides.^{15,17,19,42,44} Altogether, these results point to a key role

of the dorsal flaps in coupling the coiled-coil domain to the active site. The exact mechanism by which the dorsal flaps are involved in mediating NO-induced activation remains to be determined.

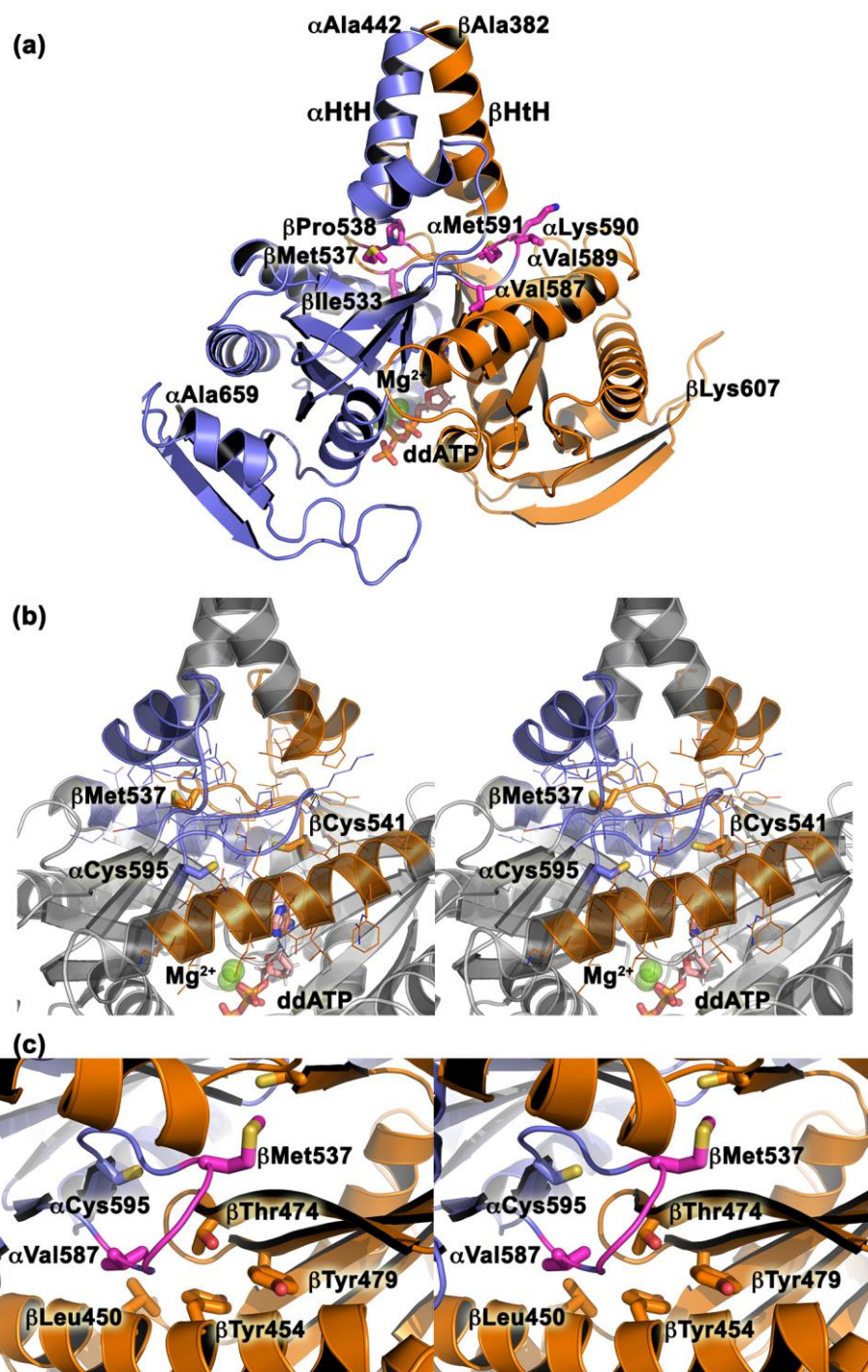


Figure 3.5. Model for wild-type CC-GC^{cat}. (a) The model was generated with SWISSMODEL^{54,55} with the 3D structure of the CyasOL helical and cyclase domains as a template (PDB code 5O5K). Residues 442-659 (blue) and 382-607 (orange) were modeled for αGC-1 and βGC-1, respectively. Key residues from the dorsal flaps mutated in this study are shown as sticks and labeled. The helix-turn-Helix (αHtH and βHtH) motifs of the penultimate coiled coil domain are indicated. Magnesium ions (green balls) and dideoxy-ATP (sticks, ddATP) are included in the model. (b)

Stereoview of the central positioning for the dorsal flaps, which are sandwiched between the helix-turn-helix motif and the active site of the catalytic domain. The view is the same as in (a). Key residues are shown in sticks and colored in blue (α GC) and orange (β GC). (c) Stereoview of the hydrophobic pocket around residue β Thr474.

3.5.2.2. Synergy Between the Dorsal Flap, the Dimer Interface, and the Substrate-Binding Region Suggests Possible Hotspots

Our studies identify for the first time synergy among different structural elements of the catalytic domain to increase GC-1 activity. In particular, combining various activating mutations not only activates GC-1 but also affects its substrate specificity.

The α Cys595Ser mutation was the second activating mutation ever identified for GC-1.^{25,45} We had originally hypothesized that substitution of sulfur with oxygen may improve hydrogen bonding at the dimer interface with residues β Thr474 and α Glu526 to increase GC-1 activity.¹¹ Accordingly, we measured significantly higher luciferase activity and extracellular cGMP levels for cells transformed with the α Cys595Ser GC-1 mutant compared to wild-type GC-1. This variant had the highest extracellular cGMP levels out of all single-point mutations measured in this study. To identify potential hydrogen-bonding partners, we mutated nearby residues β Thr474 and α Glu526, located on the substrate-binding hairpins. First, the double α Cys595Ser/ α Glu526Ala showed increased GC-1 activity, despite the loss of the hydrogen bonding side-chain on α Ala526, suggesting that this residue does not play a key role in GC-1 activity. Second, substitution of β Thr474 with hydrophobic residues (Val, Met) increased GC-1 activity. This was also observed in the double α Cys595Ser/ β Thr474Val variant. This suggests that β Thr474 is not involved in a hydrogen-bonding network at the dimer interface. This residue is located in a

hydrophobic pocket lined with residues β Leu450, β Tyr454, β Tyr479, α Phe597, and dorsal flap residue α Val587 (**Figure 3.5c**), whose mutation into a larger hydrophobic residue also increased GC-1 activity (vide supra). Based on our results, we propose that the β Thr474Val and β Thr474Met mutants fill a hydrophobic pocket at the interface between the helical domain and the active site to promote GC-1 activation, similarly to what we proposed for α Val587. Instead of the interfacial hydrogen-bonding network that we originally proposed, our results point to coupling between the various structural elements in the catalytic domains. This is further confirmed by the synergistic increase in activity observed for the double α Cys595Ser/ β Met537Asn GC-1 variant. These residues are located 8 Å apart and link the helical domain to the active site center. Their mutation into hydrogen-bonding residues could therefore alter the interface between the helical domain and the catalytic substrate-binding regions, leading to an active conformation. We propose that α Cys595, β Thr474, and β Met537 are part of a network of amino acids that connect the helical domain to the active site.

All GCs possess a Glu-Cys residue pair thought to be involved in nucleobase specificity via hydrogen bonds.⁴⁶ Indeed, β Cys541 mutations have previously been shown to influence GC-1 substrate specificity and activity. The β Cys541Asp mutant switched GC-1 to an AC while retaining NO sensitivity,³⁶ and the β Cys541Ser mutant abolished GC-1 activity and NO sensitivity.²⁵ Interestingly, the Cys residue is replaced by Gly562 in the bacterial GC from *Synechocystis PCC6803* (GC_{cya2}), which shows even greater specificity for GTP.³⁵

To test the role of β Cys541 in GC-1, we made the β Cys541Gly mutant, which we predicted would be highly specific for GTP over ATP. Instead, we found that the β Cys541Gly GC-1 variant displayed greater activity than wild-type GC-1 but lost GTP substrate specificity. Additionally, we showed that when this mutation was combined with activating mutations at the dimer interface (α Cys595Ser/ β Cys451Gly) and the dorsal flap (α Cys595Ser/ β Met537Asn/ β Cys451Gly), activity was increased synergistically and specificity for GTP was increased compared to wild-type GC-1. Our results thus suggest that the role of β Cys541 is more complex than just providing interaction to the nucleobase. Instead, we propose that α Cys595, β Met537, and β Cys451 are part of a network of hot spots that allow transmission of the NO signaling events from the HNOX domain through the coiled-coil domain to the active center of the catalytic domain.

Not all combinations of mutations were found to be synergistic. In particular, the β Pro538Gln mutation was found to dampen the synergistic activation observed for other mutants described above. We hypothesized that the β Pro538Gln variant, located in the dorsal flap, would be activating as seen previously for the AC Pro1015Gln mutation.³⁴ While the single-point variant had a modest increase in GC-1 activity, the quadruple α Cys595Ser/ β Met537Asn/ β Cys451Gly/ β Pro538Gln variant had about half the activity of the highly active α Cys595Ser/ β Met537Asn/ β Cys451Gly variant. This was also true for the α Cys595Ser/ β Met537Asn/ β Pro538Gln vs. α Cys595Ser/ β Met537Asn variants, and the α Cys595Ser/ β Pro538Gln vs. the α Cys595Ser variants. These results corroborate previous results that suggested that the homologous Pro1015 in AC and Pro858 in retinal GC are highly influential on

activity.^{47,48} The β Pro538 residue is located on the dorsal flap at the interface with the helical domain preceding the catalytic domain (**Figure 3.5b**). In all the multiple variants cited above, mutation of the rigid β Pro538 into a more flexible hydrogen-bonding residue has a negative effect on activity. Our results thus confirm our hypothesis that a fine balance of interactions mediated by the dorsal flaps with the helical domain and the catalytic domain is critical to GC-1 activity.

In summary, we have optimized a luciferase reporter assay for GC-1 activity that we used to identify several activating variants in the catalytic domain that work in concert to coordinate GTP cyclase activity. We show that some of these residues affect not only the GTP cyclase activity of GC-1 but also its substrate specificity. Based on our results, we propose that these residues constitute hot spots in the GC-1 NO-induced activation cascade to propagate the activating signal through the penultimate helical domain to the active site. In particular, the dorsal flaps act as an interfacing switch between the helical and the catalytic domains, a mechanism that is likely shared with other class III nucleotide cyclases. Importantly, our results further our understanding of the mechanisms by which GC-1 activity is regulated and provide new routes for the rational design of small molecules that target these allosteric regions to improve dysfunctional GC-1 activity in cardiovascular diseases. The described luciferase reporter system will be used as an unbiased screening tool to identify additional mutations that activate GC-1 and/or alter its substrate specificity via random mutagenesis. It is therefore an exciting new tool to understand the evolutionary relationships between guanylyl cyclases and related adenylyl cyclases, and understand how these enzymes may have evolved distinct activation mechanisms.

3.7. Acknowledgment

We would like to thank Dr. Thomas Miller for collecting preliminary luciferase assay results. We also thank Dr. Philip Farabaugh and Dr. Zeev Rosenzweig for allowing us access to a luminometer and plate reader, respectively.

Chapter 4: Purification and Characterization of the Activated GC-1 Catalytic Domain

4.1. Introduction

Elucidation of the structural elements required for activation of the GC-1 catalytic domain ($\alpha\beta\text{GC}^{\text{cat}}$) remains elusive. Hypotheses regarding activation of $\alpha\beta\text{GC}^{\text{cat}}$ have so far relied on comparison with the active C1/C2 catalytic domain structure from homologous adenylyl cyclase (AC).^{95,127} Both structures dimerize in a head-to-tail orientation with a conserved substrate binding site at the dimer interface (see **section 2.4**).^{90,91,127} Although structurally similar, both proteins are regulated differently. C1/C2 is activated by endogenous G_{sa} , part of a G-protein coupled receptor, and exogenous forskolin, a diterpene which stabilizes the dimer.¹⁹⁰ In contrast, $\alpha\beta\text{GC}^{\text{cat}}$ is part of the soluble guanylyl cyclase (GC-1) enzyme, which binds nitric oxide (NO) with picomolar affinity using a heme cofactor to regulate $\alpha\beta\text{GC}^{\text{cat}}$ activity. The structural mechanism for this allosteric regulation remains unknown.^{44,154,156,160}

Activation of $\alpha\beta\text{GC}^{\text{cat}}$ is thought to occur via a 26° rotation of $\alpha\text{GC}^{\text{cat}}$ around $\beta\text{GC}^{\text{cat}}$, rearrangement of the GTP-binding β_2 - β_3 loop in $\alpha\text{GC}^{\text{cat}}$, and closure of the substrate-binding cleft.^{90,91} We previously predicted this rearrangement also includes re-alignment of interfacial residues at the dimer interface.⁹¹ To test these hypotheses we attempted to determine the structural elements responsible for coordinating domain activation.

Purification of $\alpha\beta\text{GC}^{\text{cat}}$ is challenging for several reasons. First, yields are rather low with typical purifications yielding ~1-2 mg of $\alpha\text{GC}^{\text{cat}}$ and <0.5 mg of $\beta\text{GC}^{\text{cat}}$ per liter of cell culture when purified separately. $\beta\text{GC}^{\text{cat}}$ is also prone to precipitation after cleaving the solubility tag in the absence of $\alpha\text{GC}^{\text{cat}}$. However, co-purification of $\alpha\text{GC}^{\text{cat}}$ and $\beta\text{GC}^{\text{cat}}$ improves yields for reasons unknown.¹⁸¹ Co-expressing each catalytic subunit with the GroEL/ES chaperone system is essential for purification, but can occasionally lead to difficulties in removing the chaperone.

Second, $\beta\text{GC}^{\text{cat}}$ has a strong propensity to homodimerize rather than bind to $\alpha\text{GC}^{\text{cat}}$, significantly reducing the amount of $\alpha\beta\text{GC}^{\text{cat}}$ heterodimers and preventing us from calculating an accurate concentration of heterodimeric $\alpha\beta\text{GC}^{\text{cat}}$.⁹¹ This is in contrast to C1/C2 where both subunits preferentially heterodimerize and activity is restored when mixed together.¹⁹¹ Furthermore, $\beta\beta\text{GC}^{\text{cat}}$ homodimers have a significant impact on crystallization studies. Indeed, we and others^{90,91} have reported the ease in obtaining $\beta\beta\text{GC}^{\text{cat}}$ crystals and difficulties in crystallizing the heterodimer. These reasons outline the difficulties in obtaining adequate amounts of purified $\alpha\beta\text{GC}^{\text{cat}}$ and the necessity for innovative methods for successful structural studies of the catalytic domain.

Here, we used a variety of tools including site-directed mutagenesis, x-ray crystallography, and immunoassays to characterize the activated $\alpha\beta\text{GC}^{\text{cat}}$. First, we present the crystal structure of the Met537Asn $\beta\beta\text{GC}^{\text{cat}}$ mutant that is structurally similar to wild-type $\beta\beta\text{GC}^{\text{cat}}$. Next, we performed activity measurements of $\alpha\beta\text{GC}^{\text{cat}}$ in cell lysates to confirm our hypothesis that dorsal flaps act as regulatory elements on activity. Finally, we designed a “linked” $\alpha\beta\text{GC}^{\text{cat}}$ (“Lnk. $\alpha\beta\text{GC}^{\text{cat}}$ ”) construct,

which fuses the C-terminus of $\alpha\text{GC}^{\text{cat}}$ to the N-terminus of $\beta\text{GC}^{\text{cat}}$ through a short linker, to promote heterodimerization. This construct, while difficult to purify, retains catalytic activity and provides an alternative construct to study the GC-1 catalytic domain.

4.2. Materials and Methods

4.2.1. Mutagenesis

Mutagenesis was accomplished through site-directed mutagenesis (Agilent) and confirmed through sequencing (GENEWIZ). Wild-type $\alpha\text{GC}^{\text{cat}}$ was mutated to Val587Ile/Val589Thr/Lys590Arg $\alpha\text{GC}^{\text{cat}}$ in a single PCR reaction with the following primers:

forward- 5' AGTGGTTCAGTGTTCGCCGGGGTAATCGGCACTAGGATGCCGCGCTATTGC 3'

reverse- 5' AAACAGGCAATAGCGCGGCATCCTAGTGCCGATTACCCGGCGAACACTGA 3'.

Wild-type $\beta\text{GC}^{\text{cat}}$ was mutated to Met537Asn $\beta\text{GC}^{\text{cat}}$ with the following primers:

forward- 5' ACTGGCGTCATTGGTCAGCGCAACCCGCGTTACTGCCTGTTTCGGC 3'

reverse- 5' GCCGAACAGGCAGTAACGCGGGTTGCGCTGACCAATGACGCCAGT 3'.

4.2.2. Expression and Purification of the quadruple $\alpha\text{Val587Ile/Val589Thr/Lys590Arg}/\beta\text{Met537Asn } \alpha\beta\text{GC}^{\text{cat}}$ variant

Purification of $\alpha\text{Val587Ile/Val589Thr/Lys590Arg}/\beta\text{Met537Asn } \alpha\beta\text{GC}^{\text{cat}}$ was performed as previously described.⁹¹ Briefly, Val587Ile/Val589Thr/Lys590Arg $\alpha\text{GC}^{\text{cat}}$ was N-terminally tagged with a 6xHis-thioredoxin (Trx) tag in the expression

vector pNH-TrxT and Met537Asn β GC^{cat} was C-terminally tagged with a 6xHis-FLAG tag in the expression vector pNIC-CTHF. Both constructs carried a TEV cleavage site and were a kind gift of Dr. Charles K. Allerton (Structural Genomics Consortium).

Both proteins were expressed separately in BL21(DE3) cells co-transformed with a plasmid containing the GroEL/ES chaperones (Takara). TB cultures (1L) were inoculated with 25 mL of overnight culture and grown to Abs₆₀₀ ~1.0. Cells were cold shocked for 1 hour and protein expression was induced with 1 mM isopropyl β -D-1-thiogalactopyranoside (IPTG) and 0.2% (w/v) arabinose. Cells grew at 15 °C, 225 RPM for 24 hours. Cells were harvested (4,000xg, 15 minutes, 4 °C) and pellets were stored at -80 °C.

Cell pellets expressing each catalytic subunit were resuspended in 50 mL of lysis buffer (50 mM sodium phosphate pH 7.5, 0.5 M NaCl, 30 mM imidazole, 0.1% Tween-20 (v/v), EDTA-free protease inhibitors (Roche), 25 mg lysozyme, and 3 μ L benzonase (Sigma)) and mixed. Cells were lysed by sonication and centrifuged (40,000xg, 45 minutes, 4 °C). Clarified lysates were loaded onto a 5 mL HisTrap pre-equilibrated with buffer A (50 mM sodium phosphate pH 7.5, 0.5 M NaCl, 30 mM imidazole) and washed until a baseline A₂₈₀ was established. The column was then washed with 15% (v/v) buffer B (50 mM sodium phosphate, pH 7.5, 0.5 M NaCl, 300 mM imidazole) to remove contaminants. Target protein was eluted by 15-100% gradient elution and SDS-PAGE was used to identify fractions to pool. TEV protease was added at a 1:13 ratio (TEV:protein (w:w)) and the cleavage reaction was dialyzed

overnight (20 mM tris, pH 8, 150 mM NaCl, 5% (v/v) glycerol) in a 6-8 kD-cutoff membrane.

Post-cleavage precipitation was removed prior to loading onto the next column (4,000xg, 10 minutes, 4 °C). The sample was injected onto HisTrap and QHP columns to remove TEV, uncleaved $\alpha\beta\text{GC}^{\text{cat}}$, the tags, and the chaperones. The flow-through was collected and concentrated in a 10 kDa-cutoff centrifugal dialysis membrane to $\text{Abs}_{280} \sim 4.3$. Size-exclusion chromatography was performed to remove residual contaminants on a Superdex 200 in 20 mM HEPES pH 7.4 and 150 mM NaCl. Fractions containing both catalytic subunits were pooled and concentrated to $\text{Abs}_{280} \sim 9.0$. Aliquots were flash-frozen in liquid nitrogen and stored at -80 °C.

4.2.3. Crystallization and Structure Determination of Met537Asn $\beta\beta\text{GC}^{\text{cat}}$

Crystals were obtained by vapor diffusion sitting drops using 0.2 μL of protein (9 mg/mL), mixed with 1 mM GTP and 3 mM MgCl_2 , and 0.2 μL of mother liquor (0.1 M PCB buffer pH 8.0, 25% (w/v) PEG 1500) from the PACT premier HT-96 crystallization screening kit (QIAGEN). Drops were set-up using an ArtRobbins Phoenix robot. Crystals were cryo-protected in 20% (v/v) ethylene glycol and flash-frozen in liquid nitrogen. Data were collected on the 9-2 beamline at the Stanford Synchrotron Radiation Lightsource. Data were processed using HKL2000.¹⁹² Phases were solved by molecular replacement (Phaser)¹⁹³ using the wild-type $\beta\beta\text{GC}^{\text{cat}}$ structure.⁹⁰ The final model was refined using PHENIX¹⁹⁴ and rebuilt with COOT.¹⁹⁵

4.2.4. Bio-Layer Interferometry

Interactions between wild-type $\alpha\text{GC}^{\text{cat}}$ and $\beta\text{GC}^{\text{cat}}$ were measured through bio-layer interferometry on an Octet-RED96 system (ForteBio). HIS2 sensors (anti-His) (ForteBio) were equilibrated in 250 μL of buffer (20 mM HEPES pH 7.4, 150 mM NaCl, 0.1% (v/v) Tween-20) for at least 10 minutes prior to loading. We used 6xHis- $\beta\text{GC}^{\text{cat}}$ (2.2 μM) for loading and a serial dilution (0-100 μM) of $\alpha\text{GC}^{\text{cat}}$ for binding. Pre-wetted sensors were equilibrated for 30 seconds in buffer to establish the baseline. Sensors were then loaded with 6xHis- $\beta\text{GC}^{\text{cat}}$ for 600 seconds and washed in fresh buffer for 120 seconds to remove unbound protein. Next, sensors were dipped in wells containing varying concentrations of $\alpha\text{GC}^{\text{cat}}$ to measure association kinetics for 600 seconds. Finally, sensors were dipped in wells containing buffer to monitor dissociation of $\alpha\text{GC}^{\text{cat}}$ from $\beta\text{GC}^{\text{cat}}$ for 600 seconds. Data were analyzed using the Data Analysis module of the Octet software package.

4.2.5. Design, Cloning, Expression, and Partial-Purification of Lnk. $\alpha\beta\text{GC}^{\text{cat}}$

4.2.5.1. Design and cloning

The genetic sequence for Lnk. $\alpha\beta\text{GC}^{\text{cat}}$ was purchased through BioBasic in a pUC57 expression vector with flanking restriction digestion sequences for NcoI and EcoRI restriction enzymes, which were used to clone into pCDF-Duet MCS-1. Lnk. $\alpha\beta\text{GC}^{\text{cat}}$ consists of the $\alpha\text{GC}^{\text{cat}}$ domain (aa. 467 – 690) fused via its C-terminus to the N-terminus of the $\beta\text{GC}^{\text{cat}}$ domain (aa. 407 – 619). A short linker (GSGSGHM) and TEV cleavage sequences link the catalytic subunits. The construct carries an N-terminal 6xHis-thioredoxin (Trx)-SUMO tag and a C-terminal AviTag sequence

(GLNDIFEAQKIEWHE) to enable biotinylation if needed. A PreScission Protease cleavage sequence is located between $\beta\text{GC}^{\text{cat}}$ and the C-terminal AviTag. Finally, the $\alpha\text{GC}^{\text{cat}}$ region contains a triple mutation (Tyr660Phe/Gln662Asn/Gly663Ala) to prevent non-specific TEV cleavage as we previously shown.⁹¹ The uncleaved peptide sequence is as follows:

6xHis-Trx-SUMO- $\alpha\text{GC}^{\text{cat}}$ -TEV- $\beta\text{GC}^{\text{cat}}$ -PP-afi

MHHHHHSSGMSDKIIHLTDDSFDTDVLKADGAILVDFWAEWCGPCKMIAPILDEIADEYQGKLTVAKLNIDQNPGTAPKYGIRGIPTLLLFKNGEVAATKVGALSKGQLKEFLDANLAMSDSEVNQEAKPEVKPEVKPETHINLKVSDGSSEIFFKIKKTTPLRRLMEAFARQGKEMDSLRFYDGIQADQTPEDLDMEDNDIIEAHREQIGGMQGQVVQAKKFSNVTMLFSDIVGFTAICSQCSPLQVITMLNALYTRFDQQCGELDVYK VETIGDAYCVAGGLHKESDTHAVQIALMALKMMELSD EVMSPHGEPIKMRIGLHSGSVFAGVVGVKMPRYCLFGNNVTLANKFESCSPRKINVSPTTYRLLKDCPGFVFTPRSREELPPNFPSEIPGICHFLDAFQNATNSKPCFQKKDVEDGNANFLGKASGIDGSGSGHMENLYFQSMGHKRPVPAKRYDNVTILFSGIVGFNAFCSKHASGEGAMKIVNLLNDLYTRFDLTLDSTRKNPFVYKVE TVGDKYMTVSGLPEPCIHARSICHLALDMMEIAGQVQVDGESVQITIGIHTGEVVTGVIGQRM PRYCLFGNTVNLTSRTETTGEKGKINVSEYTYRCLMSPENS DPQFHLEHRGPVSMKGKKEPMQVWFLSRKNTGTEETKQDDDLEVLFGQPGGLNDIFEAQKIEWHE

4.2.5.2. Expression and solubility

BL21(DE3) cells were co-transformed with Lnk. $\alpha\beta\text{GC}^{\text{cat}}$ and pGro7 (Takara Inc.) and plated on LB agar plates, supplemented with kanamycin (50 $\mu\text{g/mL}$) and chloramphenicol (35 $\mu\text{g/mL}$). A 5 mL overnight culture in Luria Broth was used to inoculate 200 mL TB media. Once cells reached $\text{Abs}_{600} \sim 1.0$, cultures were cold-shocked for 1 hr and induced with 1 mM IPTG and 0.2% (w/v) arabinose. Cells grew overnight at 15 °C, 225 RPM and were harvested (4,000xg, 15 minutes, 4 °C) and pellets were stored at -80 °C.

Pellets were resuspended in 30 mL lysis buffer (see **section 4.3.1**) and sonicated. Lysates were clarified at 40,000xg, 4 °C for 45 minutes. Expression and solubility of Lnk. $\alpha\beta\text{GC}^{\text{cat}}$ were determined by comparing crude and clarified samples by Western blot. Briefly, 10 μL of crude or clarified lysate were mixed with 5 μL of SDS-PAGE loading buffer (60 mM Tris, pH 6.8, 25% (v/v) glycerol, 2% (w/v) SDS, 5% (v/v) β -mercaptoethanol. Samples were denatured at 70 °C for 8 minutes and loaded onto a 13% acrylamide gel. Proteins were transferred onto a nitrocellulose membrane and subsequently blocked in a 4% (w/v) milk solution. Lnk. $\alpha\beta\text{GC}^{\text{cat}}$ was detected using rabbit anti- αGC -1 primary antibodies (aa. 673-690, Sigma) and goat anti-rabbit secondary antibodies coupled to alkaline phosphatase (Sigma). Bands were revealed using NBT and BCIP reagents (BioRad).

4.2.5.3. Purification of Lnk. $\alpha\beta\text{GC}^{\text{cat}}$

BL21(DE3) cells co-expressing Lnk. $\alpha\beta\text{GC}^{\text{cat}}$ and pGro7 were cultured as described in **section 4.2.2**. Pellets were resuspended in 50 mL of lysis buffer and

sonicated. The clarified lysate (40,000xg, 4 °C, 45 minutes) was loaded onto a 5 mL HisTrap column and washed in buffer A (50 mM sodium phosphate pH 7.5, 0.5 M NaCl, 30 mM imidazole). Contaminants were eluted with 15% (v/v) buffer B (50 mM sodium phosphate pH 7.5, 0.5 M NaCl, 300 mM imidazole). A gradient elution (15% - >100%) was performed to obtain semi-purified Lnk. $\alpha\beta\text{GC}^{\text{cat}}$. Based on SDS-PAGE, fractions were pooled and immediately dialyzed (20 mM HEPES, pH 7.6, 100 mM NaCl, 5% (v/v) glycerol) using 30 kDa-cutoff Millipore centrifugal filter units. The 6xHis-Trx-SUMO tag was cleaved with ULP1 overnight (1:500 (w:w)) with gentle rocking at 4 °C. Post-cleavage sample was loaded onto 5 mL HisTrap and QHP columns with buffer C (20 mM HEPES pH 7.6, 100 mM NaCl, 5% (v/v) glycerol).

Biotinylation was performed the protein post cleavage. Flow-through from the QHP was pooled and dialyzed overnight into biotinylation buffer (10 mM Tris, pH 8.0, 30 mM NaCl) in a 10 kDa-cutoff membrane. Biotinylation was performed by mixing ~0.5 μM Lnk. $\alpha\beta\text{GC}^{\text{cat}}$ with 2.5 μg BirA and supplementing with 0.5 μM biotin, 0.1 M ATP, and 0.1 M $\text{Mg}(\text{OAc})_2$. The biotinylation reaction was incubated at 27 °C for 1 hr. Precipitation was removed via centrifugation and analyzed on SDS-PAGE.

4.2.5.4. Semi-purification of Lnk. $\alpha\beta\text{GC}^{\text{cat}}$

BL21(DE3) cells expressing only Lnk. $\alpha\beta\text{GC}^{\text{cat}}$ were lysed as described in **section 4.2.5.3**. Clarified lysate was loaded onto a pre-equilibrated 5 mL Talon column. After incubating the loaded column for 30 min at 4 °C to improve binding, we washed the Talon resin in buffer A (50 mM sodium phosphate pH 7.6, 0.5 M

NaCl, 15 mM imidazole) until the A_{280} baseline was established. The column was washed with 7% (v/v) of buffer B (50 mM sodium phosphate pH 7.6, 0.5 M NaCl, 500 mM imidazole) and semi-purified Lnk. $\alpha\beta\text{GC}^{\text{cat}}$ was eluted by a 7-40% (v/v) elution gradient. Purity was analyzed by SDS-PAGE and the sample was concentrated to $A_{280} \sim 7.5$ (150 μL) and flash frozen in liquid nitrogen.

4.2.6. Activity Assays

Activity measurements were performed using cell lysates from wild-type and mutant $\alpha\beta\text{GC}^{\text{cat}}$. Briefly, BL21(DE3) cells expressing either $\alpha\beta\text{GC}^{\text{cat}}$ wild-type and mutants were grown in 100 mL TB media as described above and harvested. Each pellet was resuspended in 0.3 mL of lysis buffer (50 mM sodium phosphate, pH 7.5, 0.5 M NaCl, 30 mM imidazole, 0.1% (v/v) Tween-20) supplemented with EDTA-free protease inhibitors (Roche), 0.5 mg/mL lysozyme, and 25 U/mL benzonase. Cells were lysed using a microtip sonicator and clarified (10,000 x g, 10 minutes, 4 °C).

All reactions were performed in 40 mM tris, pH 7.4, 3 mM MgCl_2 or MnCl_2 , 1 mM GTP, 0.3 mM 3-isobutyl-1-methylxanthine, and 1 mM dithiothreitol. Reactions were incubated for 15 minutes at 37 °C and stopped with 20 mM EDTA. cGMP levels were determined using a competitive enzyme immunoassay (R&D Systems). All results were normalized to total protein determined through the bicinchonic acid assay (Pierce).

4.3. Results

4.3.1. Purification and Crystallization Attempts of Activated $\alpha\beta\text{GC}^{\text{cat}}$

Co-purification of $\alpha\beta\text{GC}^{\text{cat}}$ yielded ~1 mg of pure protein per liter of cell culture with few contaminants (**Figure 4.1**). We tried to obtain crystals of the activated $\alpha\beta\text{GC}^{\text{cat}}$ heterodimer crystal by varying several parameters. These attempts included adding GTP substrate, as well as the non-hydrolysable GTP analog GpCpp, potent inhibitors (TNP-ATP and TNP-GTP) predicted to be specific toward the heterodimer (see **section 2.5.4**), and various metal cofactors (Mg^{2+} , Mn^{2+} , and Ca^{2+}). In addition, we designed mutations to strengthen heterodimer interfacial contacts and promote heterodimerization; these mutations included $\alpha\text{Cys595Ser}$,^{104,105} $\beta\text{Met537Asn}$,¹⁰¹ and the triple $\alpha\text{Val587Ile/Val589Thr/Lys590Arg}$ variant (see **section 3.5.2**). Nevertheless, all attempts yielded $\beta\beta\text{GC}^{\text{cat}}$ homodimer crystals.

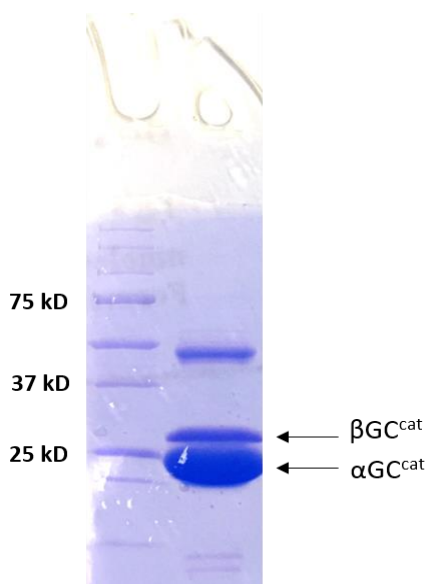


Figure 4.1. Purification of $\alpha\beta\text{GC}^{\text{cat}}$. The catalytic domains of GC-1 were purified and used for crystallization trials, BLI experiments, and activity assays.

4.3.2. Crystal Structure of Met537Asn $\beta\beta\text{GC}^{\text{cat}}$

We report here the crystal structure of Met537Asn $\beta\beta\text{GC}^{\text{cat}}$ mutant solved to a resolution of 2.2 Å (**Table 4.2**). The structure dimerizes in a head-to-tail orientation that is similar to other proteins in the nucleotide cyclase family^{90,91,95,127} and is a mixture of α -helices and β -sheets. Superimposition of mutant Met537Asn $\beta\beta\text{GC}^{\text{cat}}$ with wild-type $\beta\beta\text{GC}^{\text{cat}}$ (PDB code 2WZ1) structures showed no major conformational changes upon mutation with an RMSD value of 0.15 Å² for 331 atoms imposed. PISA analysis of the dimer interface in comparison with wild-type $\beta\beta\text{GC}^{\text{cat}}$ identified no alteration in interfacial contacts between the two subunits.^{91,196} Lastly, we compared the electron densities of wild-type and Met537Asn $\beta\beta\text{GC}^{\text{cat}}$ and found no significant discrepancies between the two aside from a modified Cys residue (see below).

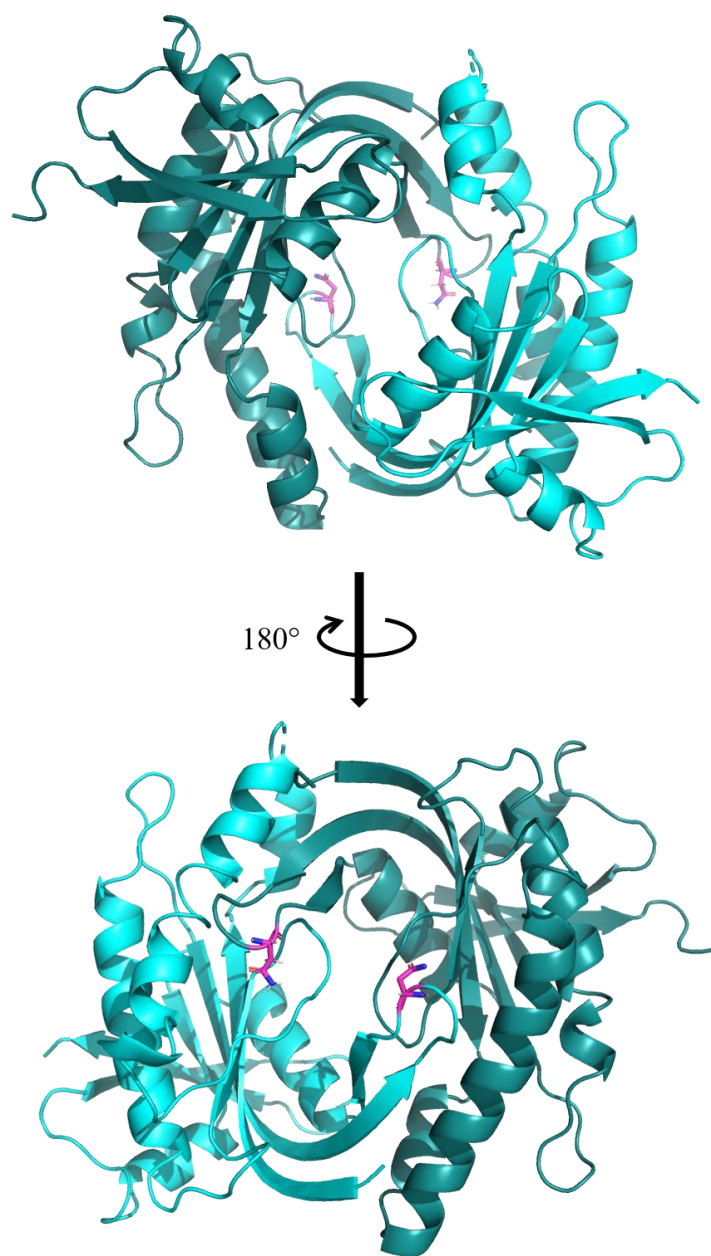


Figure 4.2. Crystal structure of Met537Asn $\beta\beta\text{GC}^{\text{cat}}$. Dorsal side (left) and ventral side (right) with the Met537Asn mutation highlighted in sticks (magenta).

Table 4.1. X-Ray data collection and refinement statistics for Met537Asn $\beta\beta\text{GC}^{\text{cat}}$.

Data Collection	
Space group	C2221
Wavelength (Å)	0.9795
Resolution (Å)	32.8 - 2.2 (2.3 - 2.2)
Unit cell parameters	$a = 65.528, b = 89.487, c = 139.697$
No. of measurements	111,783 (29,353)
No. of unique measurements	21,014 (2,059)
Redundancy	3.8 (4.3)
Completeness (%)	98.9 (99.4)
[I/ σ (I)]	6.4 (10.4)
R _{merge} (%)	8.4 (14.7)
Refinement	
Resolution range (Å)	32.8 - 2.2 (2.3 - 2.2)
No. of protein atoms	3308
No. of water atoms	286
RMSD of bond lengths	0.013
RMSD of bond angles (°)	1.12
R _{work} (%)	14.9 (14.7)
R _{free} (%)	20.5 (23.1)
<i>Ramachandran plot</i>	
Favored	97.9
Allowed	1.84
Generous	0.26
Clashscore	3.7
Avg. B-factor	26.35
Protein	25.55
Ligands	44.54
Solvent	33.32

4.4.2.1. Post-translational modification of Cys489

Analysis of electron density during structure refinement revealed that residue Cys489 on chain B was covalently modified either during purification or crystallization. A variety of modifications were modeled in an attempt to fit the electron density (**Figure 4.3**), including dimethyl arsenic, sulfenic acid, homocysteine, and mercaptocysteine, as these modifications are commonly found in

the Protein Data Bank. The $2F_o - F_c$ and $F_o - F_c$ electron density maps were used to guide this process along with Wilson B-factors for the corresponding atoms of the functional group. Based on this analysis, the dimethyl arsenic modification was chosen (**Figure 4.4**). Crystallization conditions contained arsenic-based cacodylate buffer, which can react with exposed cysteine residues to form dimethyl arsenic-modified cysteine (residue CAS). However, high Wilson B-factors for the As atom and methyl atoms (~70-140) suggest that the modified residue may only be partially occupied.

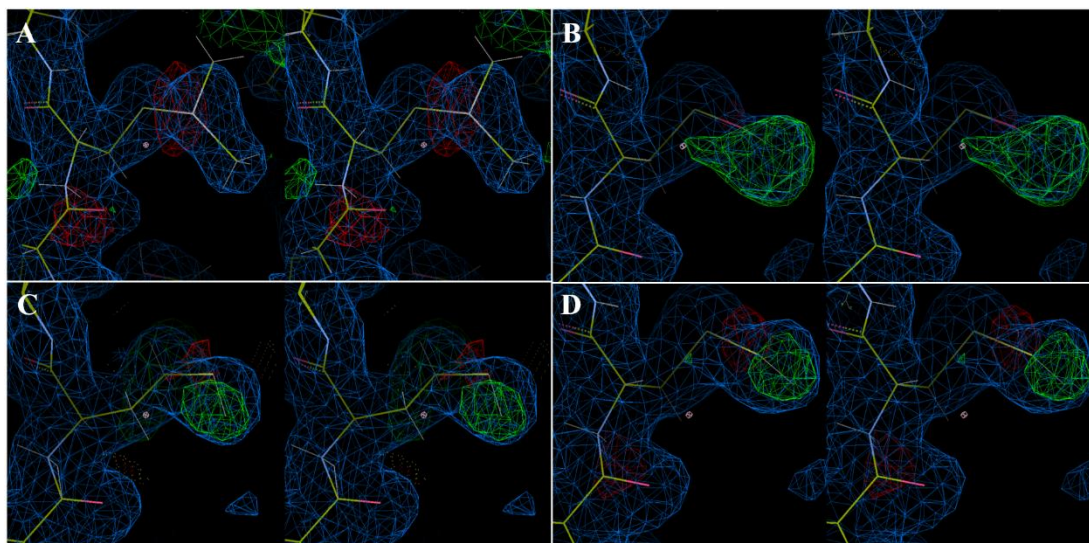


Figure 4.3. Stereo view (convergent) of electron densities for covalently-modified Cys489. Electron density was visualized with COOT¹⁹⁵ and used to determine which modification best fit the difference map (green and red). Modifications that were considered were a) dimethyl arsenic, b) sulfenic acid, c) homocysteine, and d) mercaptocysteine.

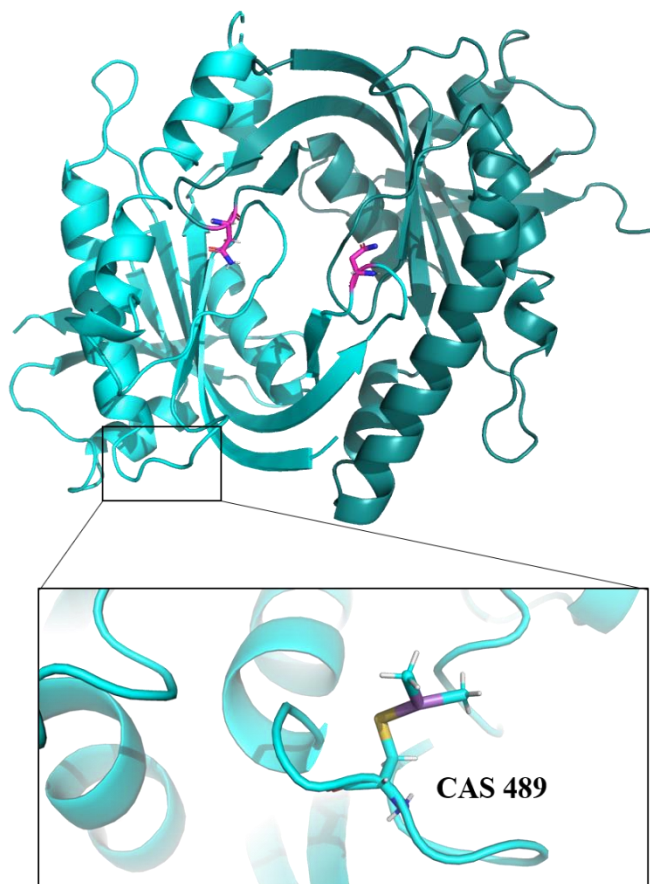


Figure 4.4. Met537Asn $\beta\beta\text{GC}^{\text{cat}}$ with dimethyl arsenic-modified Cys489. Dorsal view of Met537Asn $\beta\beta\text{GC}^{\text{cat}}$ (top) with dimethyl arsenic-modified Cys489 (CAS 489) (bottom).

This is not the first instance of a dimethyl arsenic-modified Cys residue in a GC^{cat} structure. The structure of *C. reinhardtii* homodimeric GC^{cat} showed five Cys residues covalently modified by dimethyl arsenic.⁸⁹ However, alignment of *Homo sapiens* ββGC^{cat} with *C. reinhardtii* GC shows that the modified Cys residue reported here is not homologous to those reported previously. Regardless, it suggests that this ββGC^{cat} Cys residue is sensitive to posttranslational modifications, as is the case for multiple Cys residues in GC-1.^{78,89,131,135}

4.3.3. Bio-Layer Interferometry

Bio-layer interferometry (BLI) detects biomolecular interactions such as protein-protein interactions using antibody-coated sensors.¹⁹⁷ Anti-His antibody-coated sensors (HIS2) were used to bind 6xHis-tagged βGC^{cat} and detect interactions with αGC^{cat}. Preliminary results using wild-type αGC^{cat} and βGC^{cat} suggested binding between the two catalytic subunits at αGC^{cat} concentrations 3-100 μM (**Figure 4.5**). Further attempts to identify optimal buffer conditions for heterodimerization, including addition of substrate, inhibitor TNP-GTP (see **section 2.5.4**), and use of the αCys595Ser variant, were hindered by αGC^{cat} aggregation. Furthermore, αGC^{cat} binding was inhibited by ββGC^{cat} homodimerization on the sensor (see Discussion).

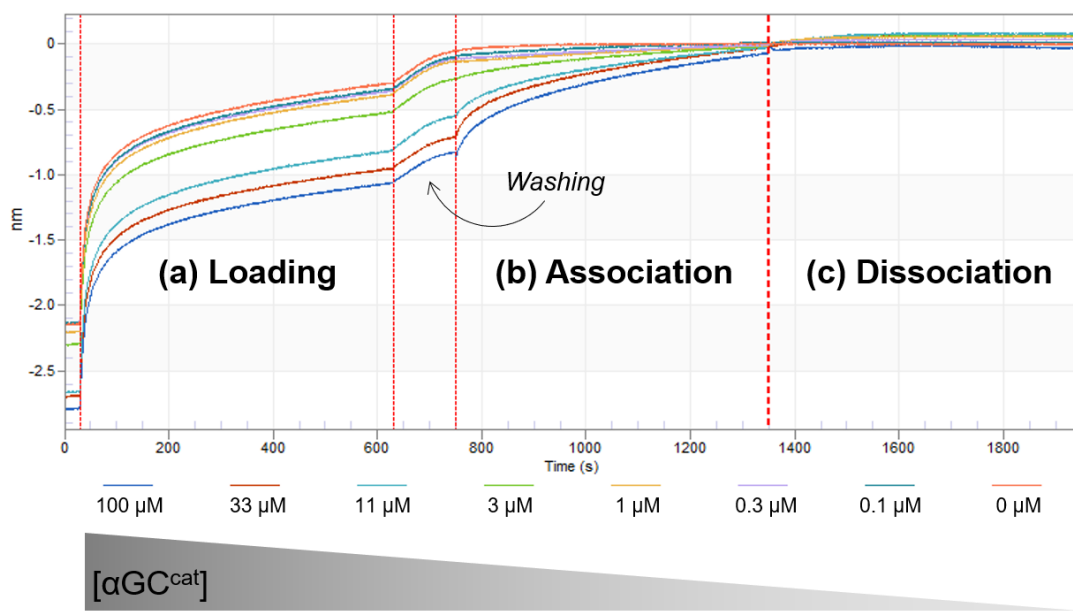


Figure 4.5. Bio-Layer Interferometry (BLI) measurements on $\alpha\beta\text{GC}^{\text{cat}}$ interactions. (a) Loading: 6xHis- $\beta\text{GC}^{\text{cat}}$ (2.2 μM) was loaded onto anti-His antibody-coated sensors. (b) Association: varying concentrations of $\alpha\text{GC}^{\text{cat}}$ was used to bind to $\beta\text{GC}^{\text{cat}}$. (c) Dissociation: sensors were dipped into fresh buffer and dissociation rates of $\alpha\text{GC}^{\text{cat}}$ were recorded.

4.3.4. Expression and Purification of “Linked” $\alpha\beta\text{GC}^{\text{cat}}$

In an effort to overcome the issues associated to preferential homodimerization, we designed a construct that contains both catalytic subunits in a single peptide: we linked the C-terminus of $\alpha\text{GC}^{\text{cat}}$ to the N-terminus of $\beta\text{GC}^{\text{cat}}$ (**Figure 4.6**). This “linked” construct (“Lnk. $\alpha\beta\text{GC}^{\text{cat}}$ ”) consisted of a 6X-His-thioredoxin (Trx) and SUMO tag at the N-terminus of $\alpha\text{GC}^{\text{cat}}$ and a 14 amino acid linker between the catalytic subunits to ensure proper alignment of catalytic residues at the dimer interface, based on our crystal structure.⁹¹

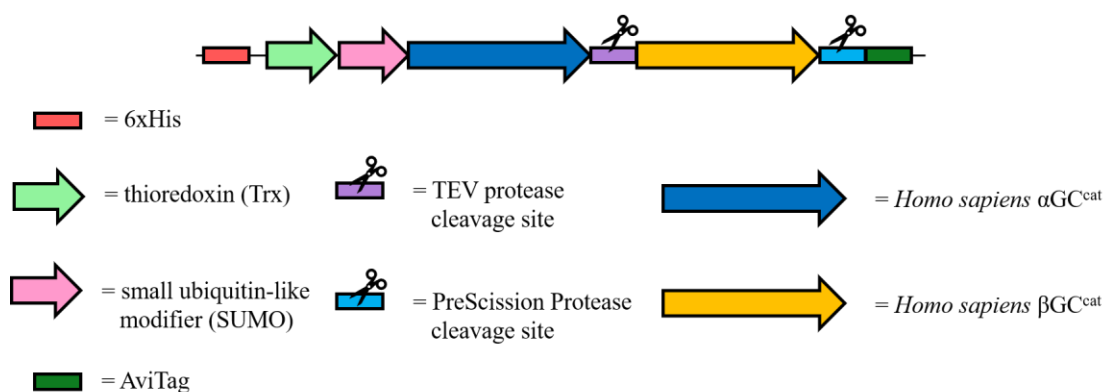


Figure 4.6. Overview of Lnk. αβGC^{cat} construct. The C-terminus of αGC^{cat} (aa. 467 – 690) was fused to the N-terminus of βGC^{cat} (aa. 407 – 619), linked by a TEV cleavage site. A 6xHis-Trx-SUMO tag was included at the N-terminus for improved solubility, and a C-terminal AviTag preceded by a PreScission Protease cleavage site was added at the C-terminus for BLI studies.

Expression and solubility of Lnk. αβGC^{cat} was confirmed when co-expressed with the GroEL/ES chaperone system (**Figure 4.7**). Initial attempts to purify the fusion construct showed optimal cleavage of the N-terminal 6xHis-Trx-SUMO tag using ULP1, however we were unable to remove GroEL from the semi-purified sample (**Figure 4.8a, 4.8b**). By taking advantage of the C-terminal AviTag, we attempted to biotinylate the semi-purified protein and use a streptavidin affinity column to further purify the construct. However, the sample aggregated after the biotinylation reaction (**Figure 4.9**). We attempted to refold precipitated Lnk. αβGC^{cat} in 5% (v/v) glycerol, but GroEL remained as a contaminant. Optimization of Lnk. αβGC^{cat} solubility and purification, including varying IPTG concentration or salting out using ammonium sulfate, were unsuccessful and lead to impurities or aggregation.

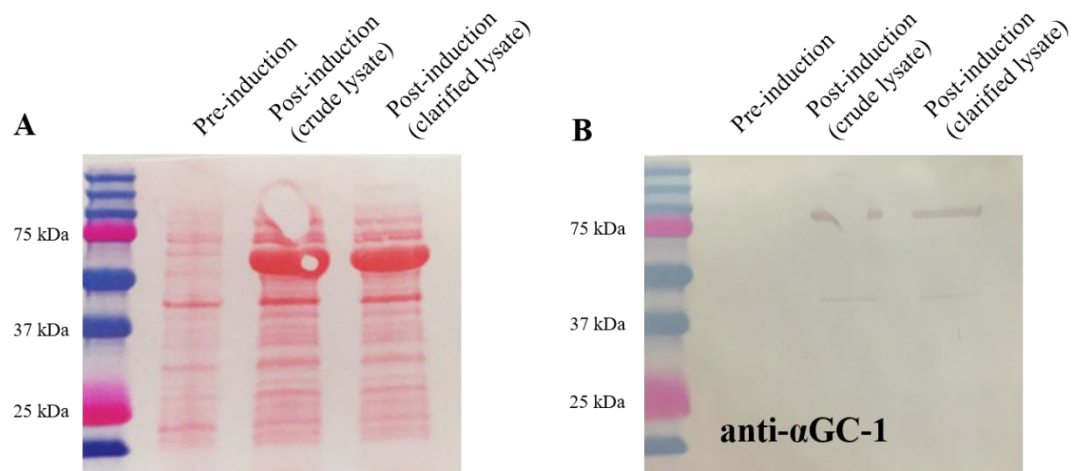


Figure 4.7. Western blot of Lnk. $\alpha\beta\text{GC}^{\text{cat}}$ crude and clarified lysates. (A) Ponceau red stain for total protein in cell lysates. (B) Western blot using rabbit anti- $\alpha\text{GC}^{\text{cat}}$ (res. 673-690) primary antibodies confirms expression and solubility of Lnk. $\alpha\beta\text{GC}^{\text{cat}}$.

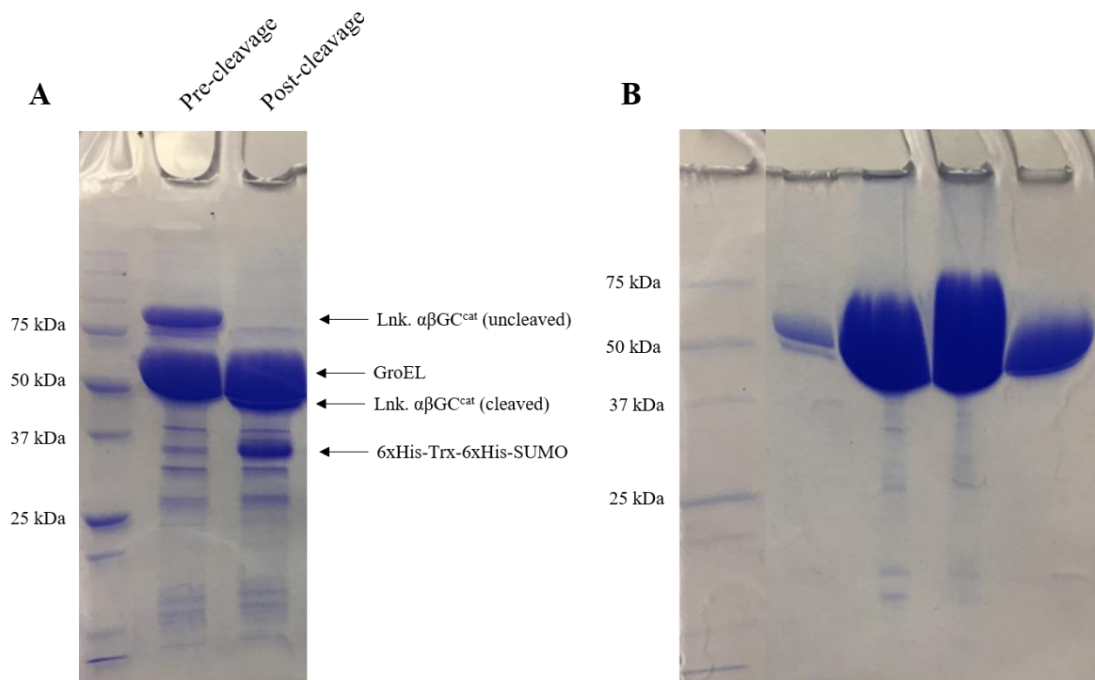


Figure 4.8. SDS-PAGE gels during purification of Lnk. $\alpha\beta\text{GC}^{\text{cat}}$. Lnk. $\alpha\beta\text{GC}^{\text{cat}}$ purity was assessed using SDS-PAGE. (A) The 6xHis-Trx-SUMO tag was cleaved overnight with ULP1. (B) SDS-PAGE of Lnk. $\alpha\beta\text{GC}^{\text{cat}}$ after elution from anion exchange where GroEL chaperone protein remained a major contaminant.

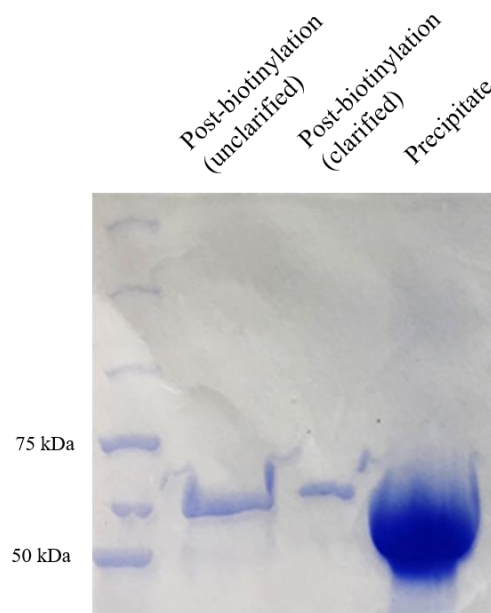


Figure 4.9. Biotinylation of Lnk. $\alpha\beta\text{GC}^{\text{cat}}$. Semi-purified Lnk. $\alpha\beta\text{GC}^{\text{cat}}$ was biotinylated using BirA, but precipitated with GroEL.

4.4.4.1 Semi-Purification of Lnk. $\alpha\beta\text{GC}^{\text{cat}}$

Attempts at purifying Lnk. $\alpha\beta\text{GC}^{\text{cat}}$ resulted in severely-contaminated or aggregated protein (see **section 4.3.4**). To overcome these limitations, we neglected the chaperone expression vector during expression in *E. coli* and semi-purified Lnk. $\alpha\beta\text{GC}^{\text{cat}}$ using Talon resin, a metal affinity resin highly-specific for 6xHis-tagged proteins (**Figure 4.10**). Semi-purified Lnk. $\alpha\beta\text{GC}^{\text{cat}}$ was used determine GC activity (see below).

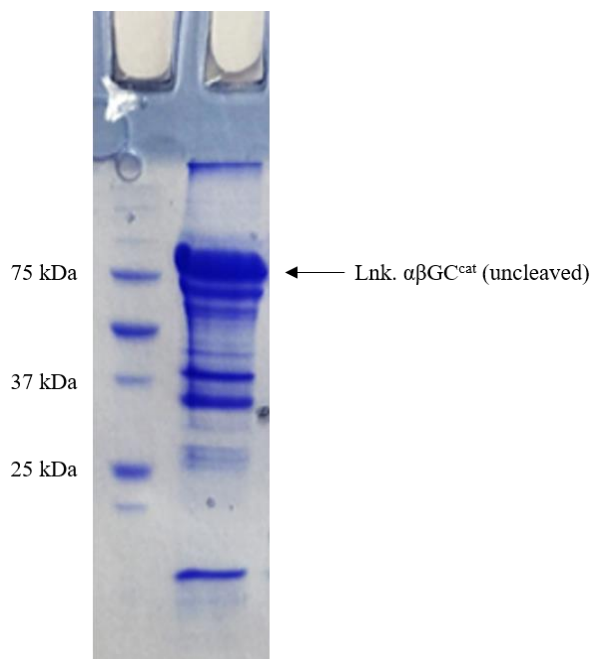


Figure 4.10. SDS-PAGE of semi-purified Lnk. $\alpha\beta\text{GC}^{\text{cat}}$. Lnk. $\alpha\beta\text{GC}^{\text{cat}}$ was semi-purified using a 5 mL Talon column and 12 μL was analyzed on SDS-PAGE.

4.3.5. Activity of Mixed Catalytic Subunits with Wild-type and Mutant $\alpha\beta\text{GC}^{\text{cat}}$ and Semi-purified Lnk. $\alpha\beta\text{GC}^{\text{cat}}$

4.4.5.1. Mixed Catalytic Subunits Display Modest Activity in Lysates

We made activating or inactivating mutations to $\alpha\text{GC}^{\text{cat}}$ and $\beta\text{GC}^{\text{cat}}$ and measured their activity in cell lysates in comparison with wild-type catalytic domains. By mixing cell lysates from cells expressing either catalytic subunit with assay buffer, we measured ~ 15 pmol cGMP/(min.mg) protein using wild-type $\alpha\beta\text{GC}^{\text{cat}}$ (**Figure 4.11**). We also expressed and purified the $\beta\text{Met537Asn}$ $\beta\text{GC}^{\text{cat}}$ with wild-type $\alpha\text{GC}^{\text{cat}}$, as this mutation was previously reported to increase the V_{max} in full-length GC-1 ~ 7 -fold.¹⁰¹ Indeed, in mixed cell lysates expressing $\alpha\text{GC}^{\text{cat}}$ and $\beta\text{Met537Asn}$ GC^{cat} , we measured a ~ 1.5 -fold increase in specific activity.

Alignment of $\alpha\text{GC}^{\text{cat}}$ and $\beta\text{GC}^{\text{cat}}$ dorsal flaps identified several differences (see **section 3.4.3**). We hypothesized that mutating the α -flap to mimic the β -flap via the triple variant $\alpha\text{Val587Ile/Val589Thr/Lys590Arg}$ mutant could potentially increase heterodimerization and increase activity. Indeed, activity measurements using cell lysates with $\alpha\text{Val587Ile/Val589Thr/Lys590Arg}$ $\alpha\beta\text{GC}^{\text{cat}}$ had a ~1.9-fold higher specific activity than those with wild-type $\alpha\beta\text{GC}^{\text{cat}}$ (**Figure 4.11**). These results support our hypothesis in achieving domain activation by targeting the dorsal α -flap.

Lastly, we measured activity from the $\beta\text{Cys541Ala}$ variant to determine. The $\beta\text{Cys541Ser}$ mutation has previously been shown to be inactivating and we hypothesized that substitution of Cys541 into Ala would have a similar effect.¹⁰⁵ Surprisingly, activity measurements using cell lysates with $\beta\text{Cys541Ala}$ $\alpha\beta\text{GC}^{\text{cat}}$ showed a specific activity that was ~1.4-fold higher than those with wild-type $\alpha\beta\text{GC}^{\text{cat}}$ indicating that the mutation may be activating instead (**Figure 4.11**).

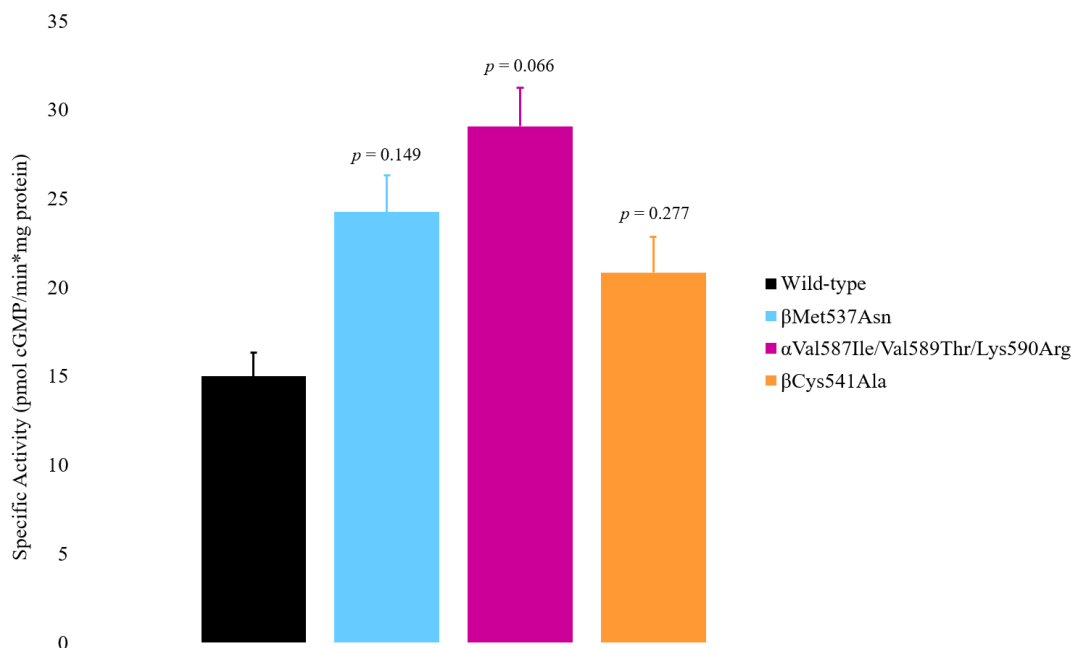


Figure 4.11. Activities of wild-type and mutant $\alpha\beta\text{GC}^{\text{cat}}$ in cell lysate. Activity from cells expressing wild-type or mutant $\alpha\beta\text{GC}^{\text{cat}}$ was analyzed using 100 μL of clarified cell lysate. Data represent an average of two technical replicates from one experiment. Statistical comparison between wild-type and mutant $\alpha\beta\text{GC}^{\text{cat}}$ was analyzed using the Student's t test. Error bars represent one standard deviation.

4.4.5.2. Lnk. $\alpha\beta\text{GC}^{\text{cat}}$ Is Active in Lysate and Semi-purified

Attempts at purifying Lnk. $\alpha\beta\text{GC}^{\text{cat}}$ resulted in severely-contaminated or aggregated protein (see **section 4.3.4**), preventing us from measuring activity on the purified protein. To determine whether Lnk. $\alpha\beta\text{GC}^{\text{cat}}$ retains GC activity, we used cell lysates from cells expressing Lnk. $\alpha\beta\text{GC}^{\text{cat}}$ and GroEL/ES and a semi-purified Lnk. $\alpha\beta\text{GC}^{\text{cat}}$ sample. In cell lysates, we measured GC activity from Lnk. $\alpha\beta\text{GC}^{\text{cat}}$ that was comparable to wild-type $\alpha\beta\text{GC}^{\text{cat}}$ (**Figure 4.12**) and activity from semi-purified Lnk. $\alpha\beta\text{GC}^{\text{cat}}$ confirmed that the construct is catalytically-competent.

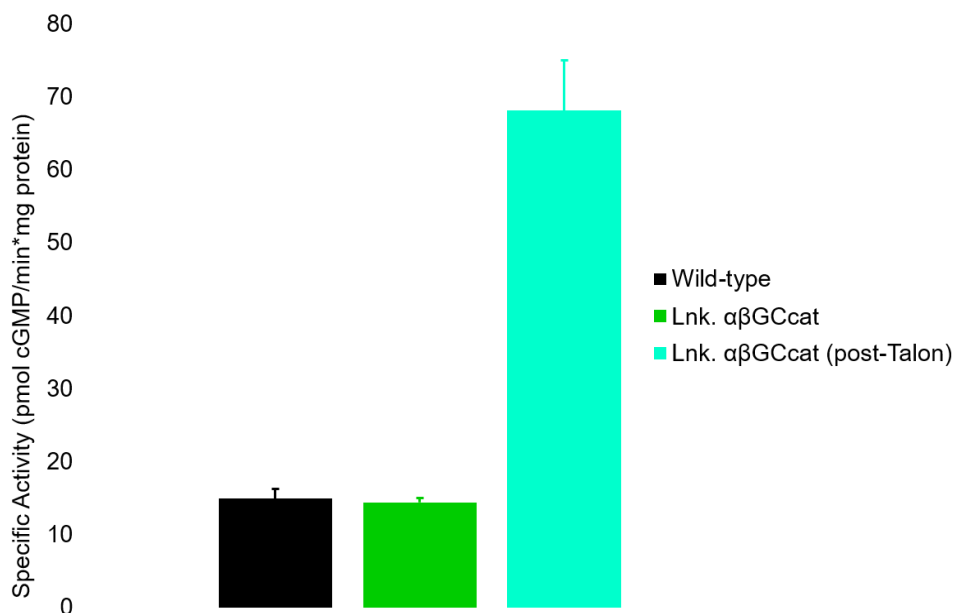


Figure 4.12. Activities of wild-type $\alpha\beta\text{GC}^{\text{cat}}$ (black) and Lnk. $\alpha\beta\text{GC}^{\text{cat}}$ in cell lysates (green) and semi-purified (teal). Activity from cell lysates used 100 μL of clarified lysate and activity from semi-purified protein used ~ 100 pmol of Lnk. $\alpha\beta\text{GC}^{\text{cat}}$. Data represent an average of two technical replicates from one experiment. Error bars represent one standard deviation.

4.4. Discussion

4.4.1. Structure of Met537Asn $\beta\beta\text{GC}^{\text{cat}}$ is similar to that of Wild-type $\beta\beta\text{GC}^{\text{cat}}$

We purified the quadruple $\alpha\text{Val587Ile/Val589Thr/Lys590Arg}/\beta\text{Met537Asn}$ $\alpha\beta\text{GC}^{\text{cat}}$ variant, which we predicted would promote crystallization of the heterodimer by increasing contacts at the dimer interface.^{91,101} However, we were only able to crystallize the Met537Asn $\beta\beta\text{GC}^{\text{cat}}$ homodimer. Like wild-type $\beta\beta\text{GC}^{\text{cat}}$, the Met537Asn variant crystallized in the C2221 space group. The catalytic domain also dimerizes in the head-to-tail fold as seen in other homodimeric and heterodimeric GC and AC structures.^{90,91,95,160} Met537Asn is located on the dorsal flaps and comparison with wild-type $\beta\beta\text{GC}^{\text{cat}}$ shows no significant structural alteration induced by the mutation.

During structure refinement of Met537Asn $\beta\beta\text{GC}^{\text{cat}}$, we determined that Cys489 was modified by dimethyl arsenic, most likely during crystallization as the protein crystallized in arsenic-based buffer (see **section 4.2.3** for crystallization details). While Cys amino acids in GC^{cat} are prone to oxidation,^{78,89,131,135} this is the first time that βCys489 was observed with a modification in a GC structure as analysis of wild-type $\beta\beta\text{GC}^{\text{cat}}$ (PDB code 2WZ1) $2F_o - F_c$ and $F_o - F_c$ density maps indicated no modification occurred.⁹⁰ Computational analysis of all Cys residues in full-length GC-1 reported the βCys489 thiol group is less solvent exposed than other Cys amino acids.¹³¹ However, HDX-MS studies comparing isolated $\alpha\beta\text{GC}^{\text{cat}}$ and $\alpha\beta\text{GC}^{\text{cat}}$ in the context of full-length GC-1 showed no indication that βCys489 is buried by regions outside of the catalytic domain.¹¹⁷ Together, this could indicate that βCys489 is more exposed in the homodimer and prone to oxidation, as seen in our structure.

4.4.2. Interactions Between Catalytic Subunits

In our case, BLI measurements were complicated by continuous binding onto the sensors, as indicated by the gradual rise in optical interference during the washing and dissociation steps. This is most likely due to free $\beta\text{GC}^{\text{cat}}$ interacting with the $\beta\text{GC}^{\text{cat}}$ -bound probe and disrupting $\alpha\text{GC}^{\text{cat}}$ binding. As our lab previously found, the isolated $\beta\text{GC}^{\text{cat}}$ domain preferentially homodimerizes rather than binding to $\alpha\text{GC}^{\text{cat}}$.⁹¹ Future work on $\alpha\beta\text{GC}^{\text{cat}}$ using BLI will need to overcome $\beta\beta\text{GC}^{\text{cat}}$ homodimers in order to calculate a reliable K_D , possibly through buffer optimization and variants that favor heterodimerization over homodimerization.

4.4.3. Activity Measurements Show that Catalytic Domains are Active in Cell Lysates

4.4.3.1. Variants in $\alpha\beta GC^{cat}$ improve activity in cell lysates

Our activity assays using mixed cell lysates expressing both GC-1 catalytic subunits support our hypothesis that variants in the dorsal flaps may be activating (see **Chapter 3**). The $\alpha Val587Ile/Val589Thr/Lys590Arg$ and $\beta Met537Asn$ mutations significantly increased GC^{cat} activity in comparison with wild-type GC^{cat} . All mutations were made along the dorsal flaps and were rationally designed to activate the catalytic domain (see **section 3.4.3**). The $\beta Cys541Ala$ mutation, which we predicted would be inactivating as $\beta Cys541$ is highly conserved in GC sequences (**Figure A2**),^{91,103} showed no detrimental impact on $\alpha\beta GC^{cat}$ activity. The $\beta Cys541$ residue is predicted to stabilize the GTP nucleotide base¹⁹⁸ and Ser substitution is sufficient to abolish activity in full-length GC-1.^{104,105} Our results are surprising and challenge the role proposed for $\beta Cys541$ as a determinant for substrate specificity. Although $\beta Cys541Ser$ GC-1 loses substrate specificity (see **section 3.4.2.2**) and substitution of $\beta Cys541$ with Gly drastically alters substrate specificity (see **section 3.4.5**), it is possible the Ala substitution reorients GTP-cleft residues to maintain adequate GC-1 activity in the isolated catalytic domain.

It is important to note that these activity measurements were adjusted to total protein amount and not normalized to the catalytically-competent heterodimer in solution. Because these mutations may impact the affinity between the catalytic domains, which could affect activity measurements,⁹¹ future work will be needed to

determine dissociation constants for mutant $\alpha\beta\text{GC}^{\text{cat}}$ and normalize activity measurements for adequate comparison with wild-type $\alpha\beta\text{GC}^{\text{cat}}$.

4.4.3.2. Wild-Type Lnk. $\alpha\beta\text{GC}^{\text{cat}}$ as a Viable Model for Future Studies

We fused $\alpha\text{GC}^{\text{cat}}$ and $\beta\text{GC}^{\text{cat}}$ domains into a single peptide to overcome complications of $\beta\beta\text{GC}^{\text{cat}}$ homodimerization in solution⁹¹ and reproducibly crystallize the active heterodimer. However, purification of Lnk. $\alpha\beta\text{GC}^{\text{cat}}$ was plagued with issues, mostly by difficulties to remove the GroEL chaperone protein that was co-expressed. Optimization of expression and purification was performed but resulted in contaminated or precipitated protein unsuitable for crystallography. Nonetheless, we showed that Lnk. $\alpha\beta\text{GC}^{\text{cat}}$ retains catalytic activity. Furthermore, by neglecting the GroEL/ES expression vector, we semi-purified Lnk. $\alpha\beta\text{GC}^{\text{cat}}$ and measured significant GC activity. Although we cannot comment on the fold of Lnk. $\alpha\beta\text{GC}^{\text{cat}}$ in the absence of GroEL, our activity measurements support the use of Lnk. $\alpha\beta\text{GC}^{\text{cat}}$ to pursue structure/function studies of the GC-1 catalytic domain. However, future work will need to overcome purification issues perhaps by adjusting N-terminal solubility tags, alternate chaperone systems to co-express, and using Co^{2+} -affinity resin as opposed to Ni^{2+} -affinity for purification.

4.5. Conclusions

We have outlined our attempts at crystallizing the activated $\alpha\beta\text{GC}^{\text{cat}}$ domain, which resulted in solving the structure of homodimeric Met537Asn $\beta\beta\text{GC}^{\text{cat}}$. Comparison with wild-type $\beta\beta\text{GC}^{\text{cat}}$ shows no significant differences, aside from a dimethyl arsenic-modified Cys residue in a solvent exposed region of the homodimer.

BLI experiments attempted to characterize affinity between catalytic subunits, but were hindered by protein aggregation and $\beta\beta\text{GC}^{\text{cat}}$ homodimerization. However, activity assay measurements did support our hypothesis that dorsal flap variants tune $\alpha\beta\text{GC}^{\text{cat}}$ activity. We also designed a “linked” $\alpha\beta\text{GC}^{\text{cat}}$ construct by fusing both subunits into a single peptide. Activity measurements in cell lysate and semi-purified samples showed that this novel fusion construct is catalytically active, despite being prone to aggregation and precipitation.

4.6. Acknowledgments

We thank Dr. David Roberts (NIH) and Dr. Thomas Miller (NIH) for assistance with BLI measurements on the Octet-RED96 (ForteBio). We also thank Dr. Zeev Rosenzweig (UMBC) for allowing us access to the SpectraMax plate reader for activity assay measurements.

Chapter 5: Summary, Future Outlook, and Conclusions

5.1. Summary

This project aimed to identify structural elements, which are responsible in coordinating GC-1 catalytic domain activity. We hypothesized NO binding to the N-terminal heme cofactor induces a rearrangement of key amino acids along the full-length enzyme to activate the C-terminal catalytic domain. Elucidation of these amino acids will aid in a structure-based drug design targeting dysfunctional GC-1 in cardiovascular diseases.

5.1.1. Aim 1: Identify the amino acids that orient the catalytic domain and promote full catalytic activity

In **Chapter 3**, we described the design, optimization, and application of a luciferase reporter assay to detect activating GC-1 variants in bacterial cells. This reporter is based on OPTXcGMPRE, a cyclic nucleotide-responsive promoter¹⁸² which was cloned upstream of the gene encoding for Firefly luciferase,¹⁷⁵ thus placing luciferase expression dependent on cGMP. By using BL21(DE3) *cyaA*-deficient cells (*cyaA*-), we measured a ~90% reduction in background luciferase expression, supporting the promiscuity of the OPTX promoter for cAMP and possibly other nucleotides.¹⁷⁵ Although our results show that function of the OPTX promoter is indeed dependent on cyclic nucleotides, the mechanism behind its regulation and function remains unclear.

Using this assay, we discovered novel activating GC-1 variants located in the catalytic domain, allowing us to propose novel hypotheses regarding potential mechanisms important for GC-1 catalysis. We combined several mutations that synergistically lead to an increase in GC-1 activity. Several of the mutations are located ~15-20 Å apart and in distinct regions of the catalytic domain, supporting our hypothesis that GC-1 activity is allosterically tuned by a network of amino acids. These results have crucial implications for the signaling mechanism of NO stimulation (see below).

5.1.2. Aim 2: Structurally characterize the activated $\alpha\beta\text{GC}^{\text{cat}}$ domain

In **Chapter 4**, we presented the crystal structure of Met537Asn $\beta\beta\text{GC}^{\text{cat}}$, which we crystallized while attempting to solve the structure of the activated $\alpha\beta\text{GC}^{\text{cat}}$ heterodimer. Considerable effort was spent to overcome the issues due to preferential $\beta\beta\text{GC}^{\text{cat}}$ homodimerization. Indeed, based on our apo inactive heterodimeric $\alpha\beta\text{GC}^{\text{cat}}$ structure,⁹¹ we designed mutations to favor heterodimerization. We also combined several activating mutants in both catalytic subunits to obtain an activated heterodimeric catalytic domain structure. Additionally, we used small molecules (substrate, substrate analogs and inhibitors) predicted to favor formation of the active conformation of the catalytic domains (see **section 2.5.4**). Despite these efforts, all crystals obtained were homodimeric. The structure of homodimeric Met537Asn $\beta\beta\text{GC}^{\text{cat}}$ carries the typical head-to-tail dimer fold reported in other GC and AC dimers.^{90,91,95,127} Interestingly, βCys489 in one of the subunits was covalently-modified with a dimethyl arsenic moiety most likely during crystallization in

cacodylate buffer. Aside from this observation, we detected no significant differences between our mutant $\beta\text{GC}^{\text{cat}}$ and the wild-type structure.⁹⁰

Activity measurements of $\alpha\beta\text{GC}^{\text{cat}}$ that contains mutations targeting dorsal flaps in both subunits confirmed that activity of the isolated wild-type catalytic domain is increased via novel mutations targeting either dorsal flap. Based on our results in **Chapter 3**, we predicted that these mutations affect interfacial contacts between the penultimate coiled-coil domain and the active site via the interfacial dorsal flaps to promote optimal catalysis. In the context of truncated $\alpha\beta\text{GC}^{\text{cat}}$, it is also possible that these mutations affect the interface between the two subunits to promote activity.

Finally, we designed a novel “linked” construct, which fused both catalytic subunits in a single peptide (“Lnk. $\alpha\beta\text{GC}^{\text{cat}}$ ”). We hypothesized that having both domains in the same polypeptide would “increase” the affinity of the subunits to each other, and favor heterodimerization. We were able to partially purify Lnk. $\alpha\beta\text{GC}^{\text{cat}}$ and measured significantly-higher GC activity from the semi-purified sample in comparison with activity in cell lysate, confirming that by fusing both catalytic subunits into a single peptide, the construct retains catalytic activity.

5.1.3. Consequences for the NO/GC-1/cGMP Field

Currently, there are two models that explain how NO-binding triggers activation of $\alpha\beta\text{GC}^{\text{cat}}$. The first model (**Figure 5.1**) suggests that N-terminal domains, including the NO-sensor βHNOX , bind to $\alpha\beta\text{GC}^{\text{cat}}$ and inhibit activity. NO-binding is predicted to relieve this inhibition and allow $\alpha\beta\text{GC}^{\text{cat}}$ to adopt a catalytically-

favorable conformation. Several groups have supported this model, using isolated β HNOX and $\alpha\beta$ GC^{cat}^{116,117} as well as the full-length GC-1 enzyme.^{152–154} However, these reports have yet to conclusively prove this model. The second model (**Figure 5.2**) suggests that stimulation is reliant on a network of amino acids across each domain. This model is supported by chemical cross-linking studies,⁸⁵ HDX-MS measurements on basal and NO-stimulated GC-1,¹⁵⁶ and, to a lesser extent, electron microscopy images.⁸⁷

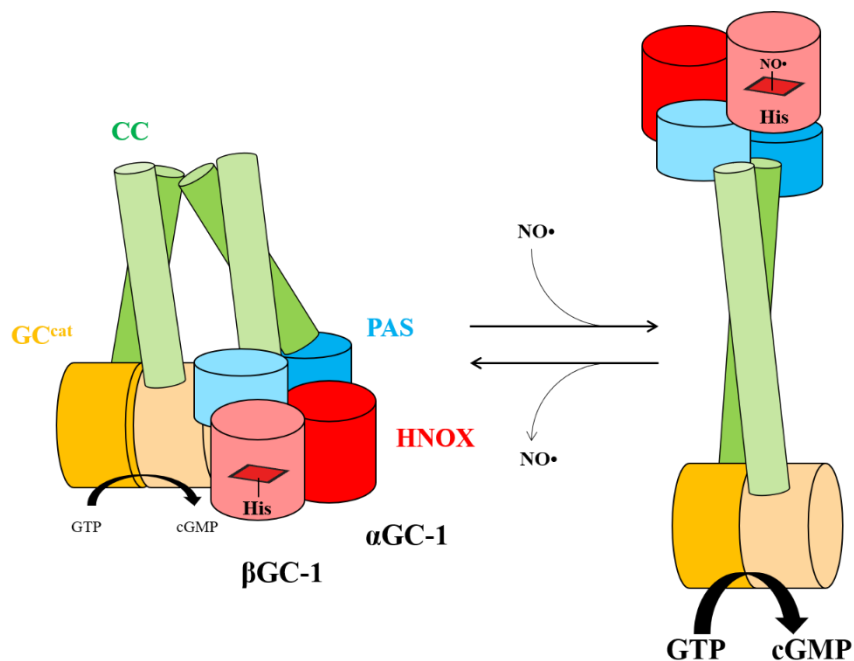


Figure 5.1. Model of GC-1 NO-stimulation through releasing putative inhibition by HNOX. (Left) GC-1 activity is inhibited through putative interactions between GC^{cat} and the β HNOX domain. (Right) Upon NO binding, inhibition is relieved and optimal GC-1 activity is restored.

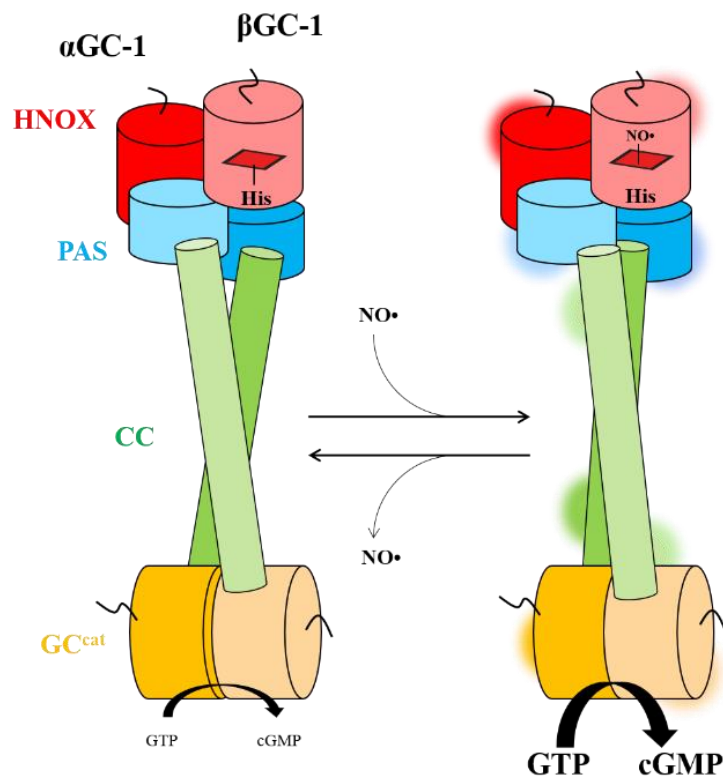


Figure 5.2. Model of GC-1 NO-stimulation through hotspots. (Left) GC-1 maintains basal activity. (Right) NO-binding reorients key amino acids in hotspots along GC-1 and propagates activation to the GTP-binding site through hydrogen bonding and hydrophobic interactions.

While the results presented in **Chapters 3 and 4** do not conclusively support one model over another, we do provide compelling data of a regulatory role for both dorsal flaps in $\alpha\beta\text{GC}^{\text{cat}}$ that may be ideal participants in a network of amino acids as outline in model B. Indeed, we identified multiple mutations that activate full-length GC-1 in **Chapter 3** and observed several of these to activate the truncated catalytic domain in **Chapter 4**. Previous work from our lab highlighted the $\alpha\beta\text{GC}^{\text{cat}}$ dorsal face to be highly-conserved and an ideal docking site for the adjacent coiled-coil (CC) domain.⁹¹ Furthermore, the recent structure of an AC domain with an attached coil on the dorsal face suggested these helical structures are crucial for dimerization and modulation of activity.¹⁶⁵ Together, these results implicate interactions between the

CC domain and dorsal flaps as a potential mechanism for tuning $\alpha\beta\text{GC}^{\text{cat}}$ activity (see **section 3.5.2**). This mechanism may be relayed through a putative interfacial hydrogen bond network to the GTP-binding cleft to promote catalysis. This hypothesis on GC-1 stimulation aligns more with model B, though does not rule potential regulatory interactions from βHNOX or other N-terminal domain.

5.2. Future Outlook

5.2.1. Future Studies Using the Novel Luciferase Reporter Assay

Since our luciferase reporter assay has been optimized and validated to detect active GC-1 variants (see **Chapter 3**), our lab now has an exciting new tool to probe GC-1 structure and function. Below, I have outlined several novel variants to test and present preliminary findings in support of this investigation.

5.2.1.1. NO-stimulated GC-1 activity using NO-donors

Thus far, the luciferase reporter assay has provided indirect measurement of basal GC-1 activity, but not NO-stimulated activity. Biophysical characterization of communication between the GC-1 heme pocket and catalytic domain remains essential for understanding the NO/GC-1/cGMP pathway. Future studies with the luciferase reporter assay can improve on this understanding using NO-donors during cell growth. Our lab has acquired several NO donors including DETA-NONOate and NOR3 which have significantly longer half-lives than standard NO donors.^{199,200} DETA-NONOate and NOR3 are ideal sources of NO for our luciferase reporter assay measurements as our findings indicate GC-1 activity is most active at 72 hours post-

induction in *E. coli*. After confirming these NO-donors stimulate wild-type GC-1 using our luciferase reporter assay, variants that have been shown to activate basal GC-1 can be used to determine a potential synergistic effect. Activating variants that synergize with NO-stimulation could further indicate these residues participate in the signal propagation of NO-binding.

5.2.1.2. Positively-charged residues on dorsal flaps

Alignment of GC and AC catalytic domains revealed the dorsal flaps carry a central Lys or Arg amino acid (**Figure A2**). Our lab has designed primers to mutate the corresponding amino acids α Lys590 and β Arg536 in *H. sapiens* GC-1 to Ala or Glu to determine the impact of removing the positively charged amino acid or charge-reversal. Preliminarily, β Arg536Ala GC-1 significantly increased luciferase activity in comparison with cells transformed with wild-type GC-1 (**Figure 5.4**). Future studies will measure extracellular cGMP levels to confirm whether or not β Arg536Ala does indeed increase GTP cyclase activity. The α Lys590 GC-1 variants will also be generated to determine their effect on activity. These tests will highlight a unique role for the presence of a positively-charged amino acid on the dorsal flaps.

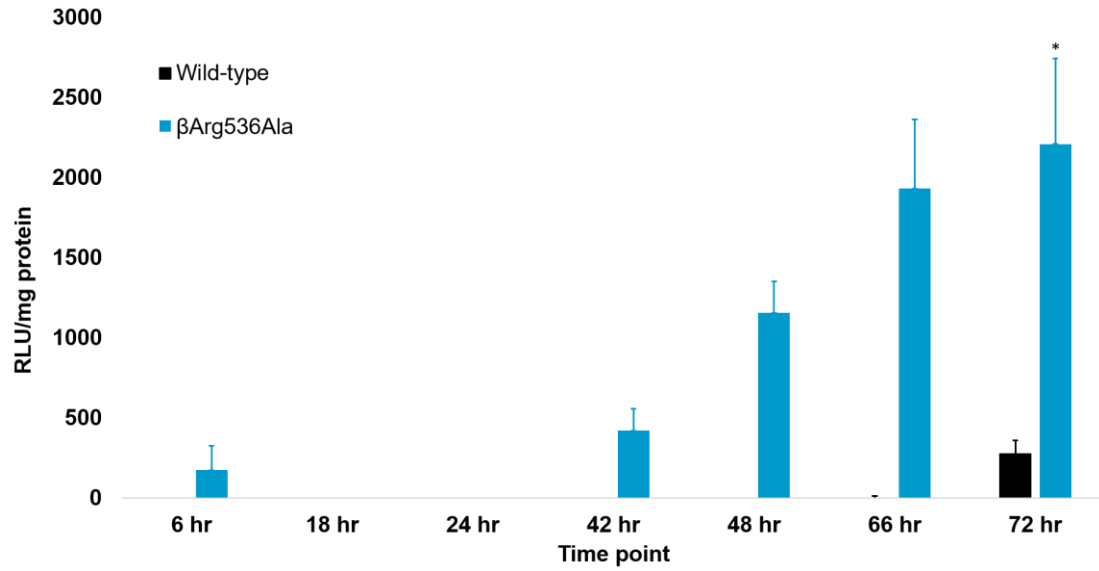


Figure 5.3. Luciferase activity induced by wild-type GC-1 and β Arg536Ala GC-1. Data represent an average of three or more experiments. Error bars represent the standard error of the mean. Statistical comparison between wild-type and β Arg536Ala GC-1 at the 72 hour time point was analyzed using the Student's *t* test (* $p < 0.05$).

Table 5.1. Extracellular cGMP levels from wild-type and β Arg536Ala GC-1 cells. cGMP levels were measured in the extracellular supernatant after 72 hours of cell growth using the R&D immunoassay kit and were plated in duplicate. Error represents the standard error of the mean from three or more independent experiments.

Sample	pmol cGMP/ mg protein ($\times 10^3$)	Fold-increase
Wild-type $\alpha\beta$ GC-1	1.87 ± 0.5	1.0
β Arg536Ala	3.43 ± 1.1	1.8

5.2.1.3. Characterization of β Phe543Ala in the GTP-binding cleft

To explore whether β Cys541Gly GC-1 activity could be due to reduced steric hindrance in the substrate-binding cleft, we made the variant β Phe543Ala that we predicted would be activating. Preliminary luciferase assay measurements were conflicting between replicates, however extracellular cGMP measurements suggested β Phe543Ala abolished GC-1 activity (data not shown). While β Phe543 is not predicted to be directly involved in GTP catalysis,¹⁶⁰ *in silico* docking with predicted GC^{cat} inhibitors show it may provide stabilizing van der Waals interactions with several compounds.^{118,149} Furthermore, our alignment between GC-1 and AC catalytic subunits shows this residue is invariant in $\alpha\beta$ GC^{cat} sequences. It would be interesting to determine how β Phe543Ala affects activity in superactive variants outlined in **Chapter 3** such as α Cys595Ser/ β Met537Asn and whether β Phe543Ala also synergizes with other variants.

5.2.2. Elucidation of Regulatory Elements for $\alpha\beta\text{GC}^{\text{cat}}$ Activation

5.2.2.1. Unbiased detection of active GC-1 variants through error-prone mutagenesis

Activating GC-1 variants discussed thus far have focused on the C-terminal catalytic domain due to the abundance of structural information provided by AC and GC^{cat} structures^{90,91,127,160,165,167,168} and an absence of structures of mammalian HNOX and PAS domains or full-length GC-1. As a consequence, rationally designing mutants in other GC-1 domains remains challenging. We tried extensively to randomly mutate GC-1 residues through methods such as error-prone PCR by substituting Mg^{2+} with Mn^{2+} and chemical mutagenesis with ethyl methanesulfonate,^{201,202} however, efforts thus far have been unsuccessful due to reduced polymerase activity with Mn^{2+} substitution and lack of colonies post-transformation. Recently, we obtained the error-prone *E. coli* cell line XL1-Red (Agilent), which lack several proteins involved in proof-reading.²⁰³ These cells are ideal hosts to perform random mutagenesis on a given plasmid without the need for additional reagents. Initial attempts using these cells yielded only silent mutations. By extending the growth time of XL1-Red cells transformed with wild-type GC-1 to three days, exchanging cells into fresh LB media every 24 hours, sequencing results confirmed successful random mutagenesis. We obtained the $\beta\text{Phe430Cys}$ GC-1 variant, as well as an additional mutation near multi-cloning site, outside of the βGC -1 gene. The βPhe430 residue is located in a buried hydrophobic pocket located at the $\alpha\beta\text{GC}^{\text{cat}}$ dimer interface and it is unclear how the Cys substitution will influence this region of the enzyme as well as the nearby catalytic site. BL21(DE3) *cyaA*- cells

transformed with this variant along with pOPTXcGMPRE:LUC and pGro7 have been grown and await analysis for luciferase activity and cGMP levels.

Future attempts at random mutagenesis using XL1-Red cells will require extended cell growth time to allow for increased rates of mutation. Using error-prone *E. coli* to generate a library of GC-1 mutations combined with the luciferase assay and cGMP level measurements will allow for unbiased identification of activating variants,²⁰⁴ and permit directed evolution of GC-1 and identification of residues responsible for NO-stimulation.

5.2.2.2. *Conserved residues*

Our alignment of catalytic subunits from GC and AC enzymes highlights five amino acids that are 100% identical across 27 sequences (see **section 3.4.3**). Given that most of these amino acids are too far from the substrate-binding cleft to directly participate in catalysis, they may be crucial residues participating in interfacial contacts to stabilize the catalytic domain. Future studies using MD simulations can determine how removing these residues may affect intersubunit contacts. Residues that are predicted to be crucial for intersubunit contact alignment can be targeted for alanine substitution and $\alpha\beta\text{GC}^{\text{cat}}$ activity will be measured in cell lysate. These results will impact research on GC-1 and AC protein and, more broadly, protein evolution in the context of allostery.²⁰⁵

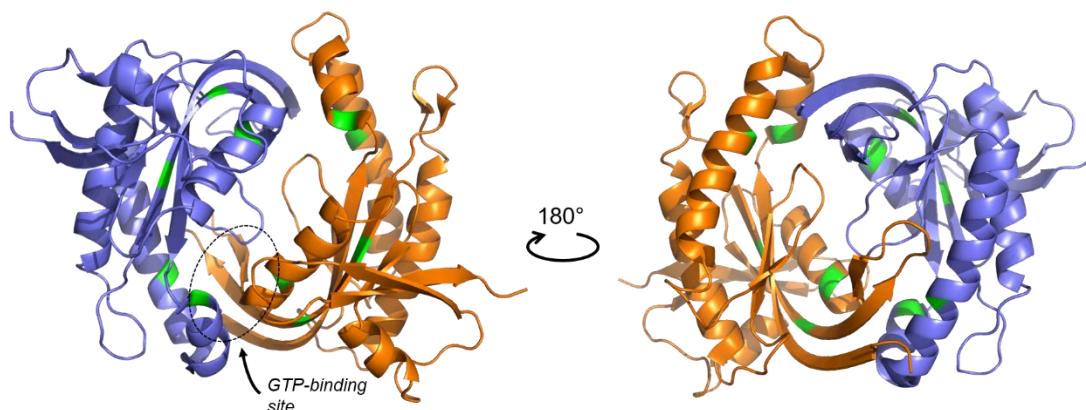


Figure 5.4. Highly-conserved residues in GC^{cat}. α GC^{cat} (violet) and β GC^{cat} (orange) with residues that are 100% conserved across 27 GC-1 and AC catalytic sequences (green).

5.2.3. Characterizing the regulatory role of N-terminal GC-1 domains

The β HNOX domain was proposed to inhibit activity of the catalytic domain.^{116,117,152} In this model, NO binding to the heme cofactor relieves the repression and cyclase activity increases 100-200-fold. This hypothesis remains controversial and requires further insight. Our luciferase reporter assay presents an ideal tool to quickly determine domains crucial for GC-1 activity without relying on protein purification and cGMP measurements, which can be timely and costly. The plasmid used to express heterodimeric GC-1 (pCDF- $\alpha\beta$ GC1) carries α GC-1 in MCS-1 and β GC-1 in MCS-2. Through simple site-directed mutagenesis and cloning, domains can be removed from this construct and GC-1 activity can be assessed through the luciferase reporter assay as outlined in **Chapter 3**. Expression and solubility of these constructs will be assessed through SDS-PAGE and Western blotting. Constructs with impaired expression or solubility can be improved by fusing N-terminal solubility tags such as maltose binding protein or SUMO.

5.3. Conclusions

5.3.1. Aim 1: Identify the amino acids that orient the catalytic domain and promote full catalytic activity

Using a bacterial luciferase reporter assay to screen activating GC-1 variants, we have identified a network of residues that tune catalytic activity. We targeted three distinct regions in the catalytic domain- i) dorsal flaps, ii) the dimer interface, and iii) the GTP-binding cleft. Several of these variants synergized to drastically increase activity up to ~15.3-fold greater than wild-type GC-1. Intriguingly, one variant on the dorsal flap had a consistently-antagonistic effect when added to other active constructs, further implicating a novel regulatory role for the dorsal flaps. Together, our results support a model of GC-1 activity relying on hotspots in the catalytic domain for activation. These hotspots may mediate the propagation of the NO-binding event via the preceding CC domain to reorient $\alpha\beta\text{GC}^{\text{cat}}$ into a catalytically-active conformer.

5.3.2. Aim 2: Structurally characterize the activated $\alpha\beta\text{GC}^{\text{cat}}$ domain

In our attempts to crystallize the activated $\alpha\beta\text{GC}^{\text{cat}}$ structure, we determined the structure of the catalytically-inactive Met537Asn $\beta\beta\text{GC}^{\text{cat}}$. Activity measurements on wild-type and mutant $\alpha\beta\text{GC}^{\text{cat}}$ in cell lysates supported our hypothesis that targeting the dorsal flaps through rationally-designed mutagenesis is a novel method to activate the GC-1 catalytic domain. To promote heterodimerization, we fused both catalytic subunits together, connected by a short linker sequence, and measured GC-1

activity from this construct in cell lysates and when semi-purified using Co^{2+} -affinity resin.

Appendices

1. Appendix A

1.1 Supporting Information

1.1.1. Background Luciferase Expression

We measured background luciferase activity and subtracted averaged data from all subsequent luciferase assay measurements. To mimic experimental conditions, we constructed a pCDF- $\alpha\beta$ GC1 expression vector lacking the gene for *H. sapiens* β GC-1, thus preventing GC activity from occurring. We co-transformed BL21 *cyaA*- cells with this plasmid in addition to pOPTXcGMPRE:LUC and pro7 expression vectors (see **Table 3.1**) and measured luciferase activity clarified lysates (**Figure A2**). These activity measurements represent background luciferase activity, most-likely induced by cyclic nucleotides present in the cell culture media, and was subtracted from all data presented in **Chapter 3**.

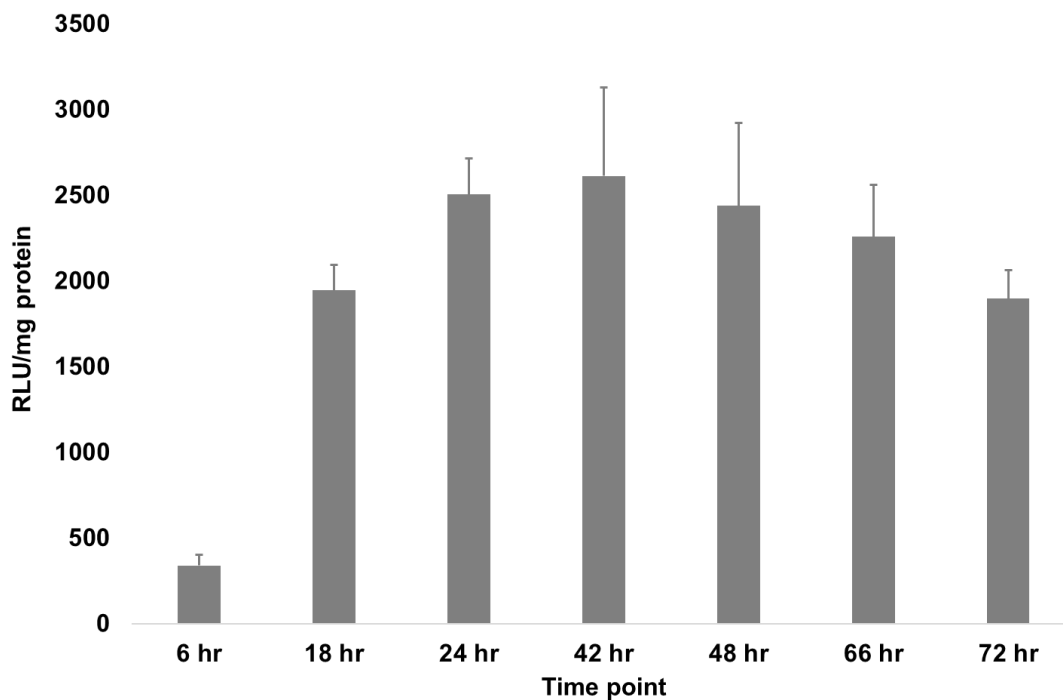
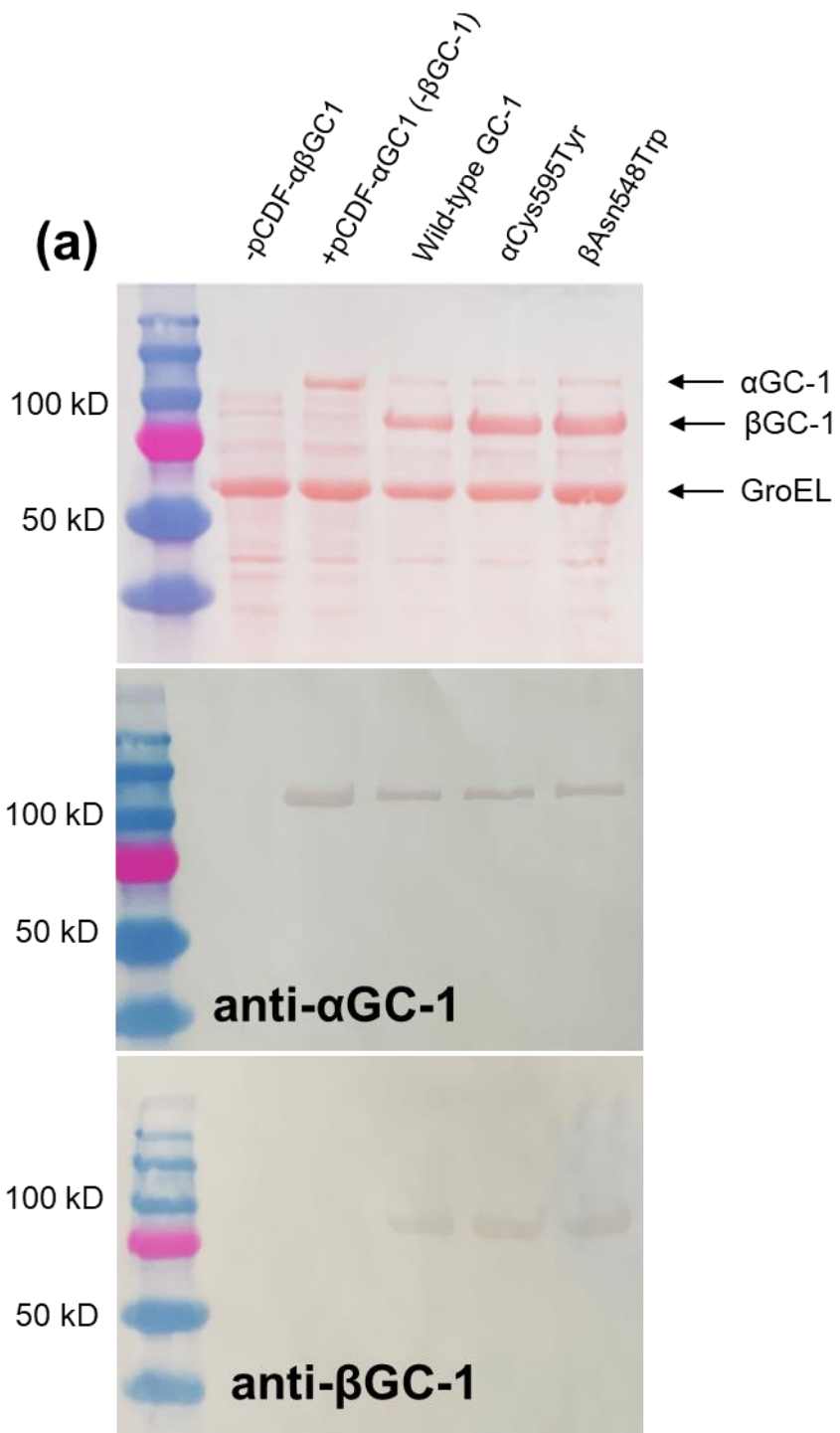
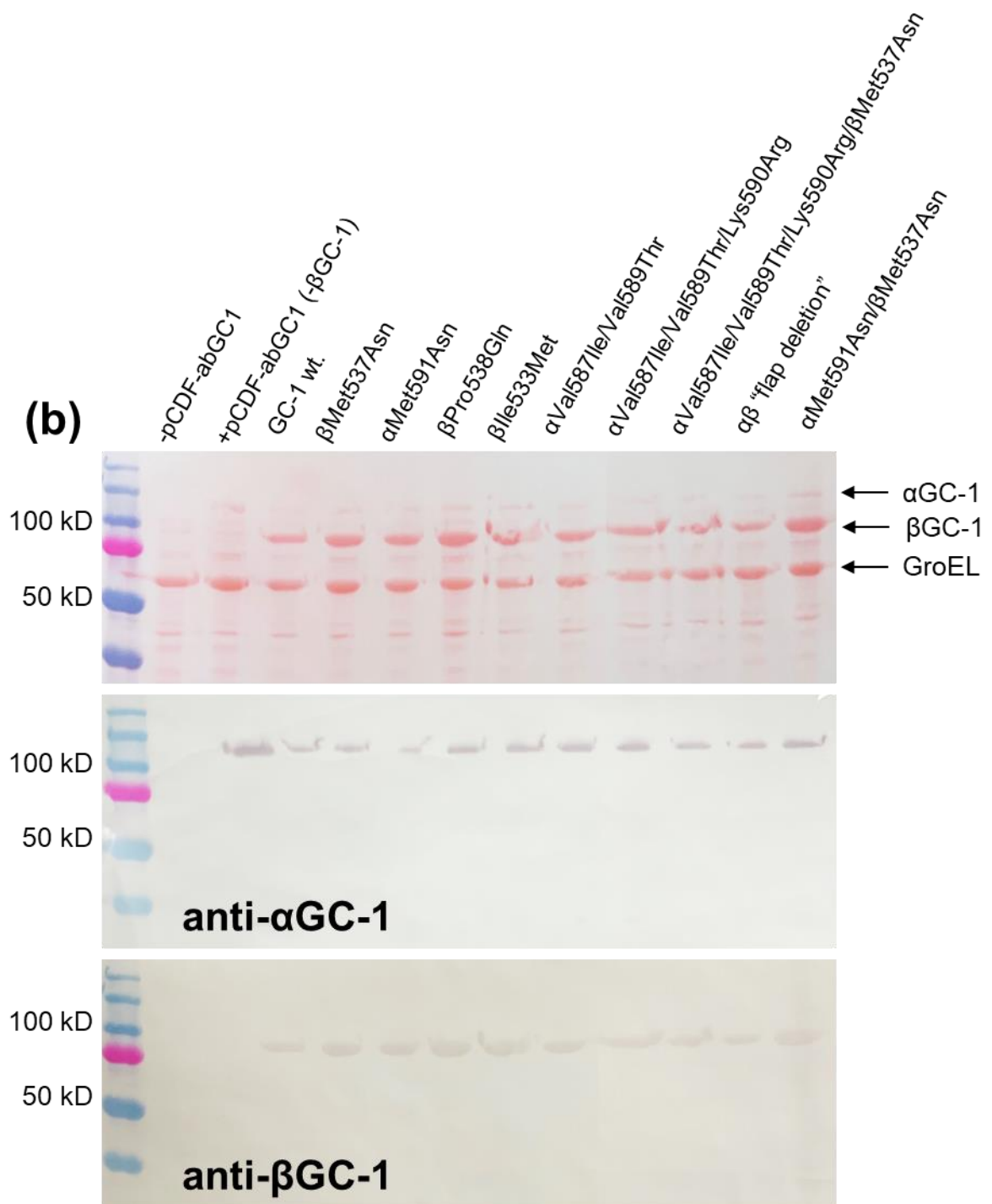


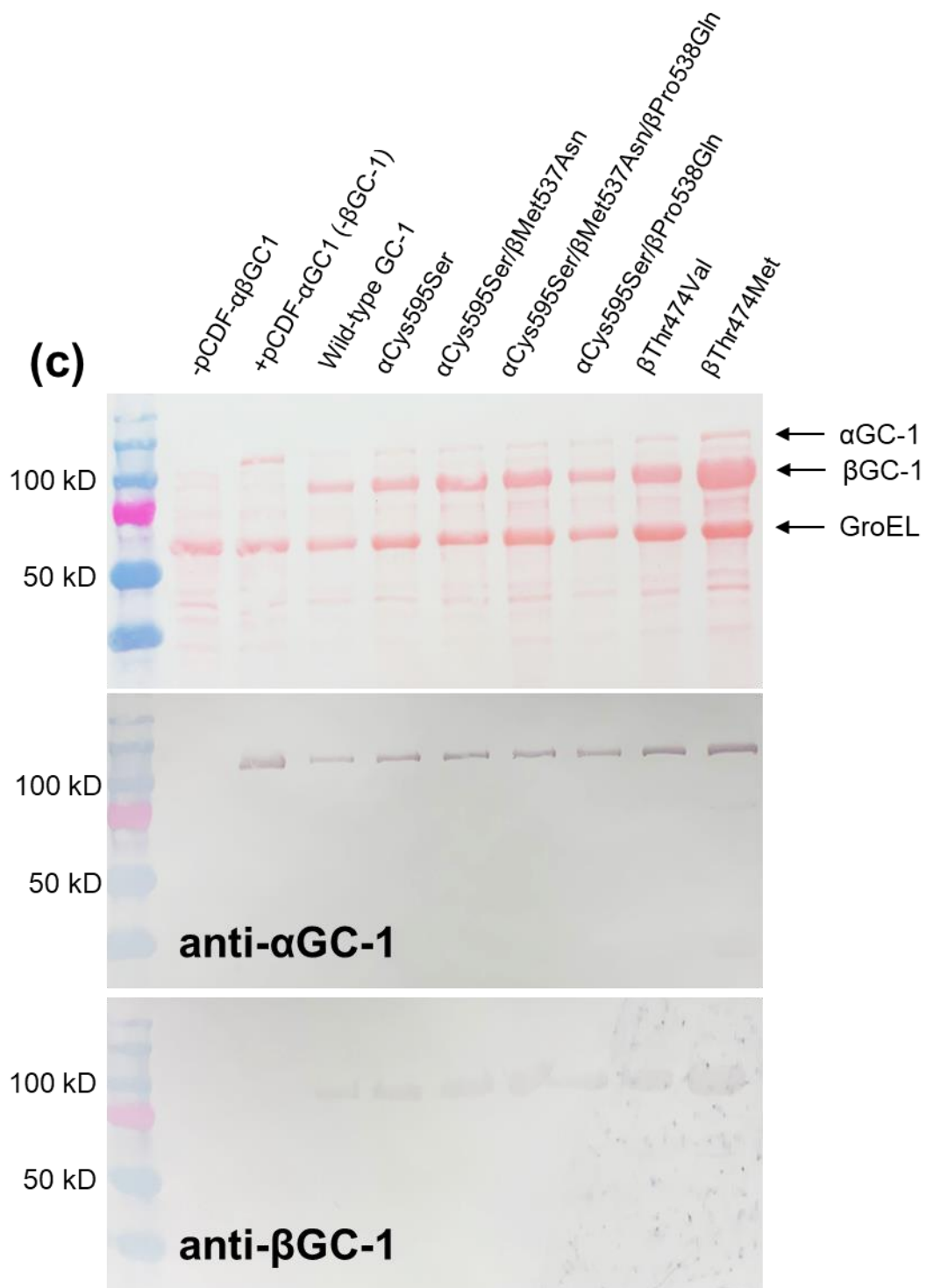
Figure A1. Background luciferase activity in BL21(DE3) *cyaA*⁻ cells. Error bars represent the standard error of the mean from three or more experimental replicates.

1.1.2. Expression tests for wild-type and mutant GC-1

Expression of wild-type and mutant α GC-1 and β GC-1 was determined at the 72 hr time point through Western blot (**Figure A2**). Ponceau Red stain stained for total protein expression, including the co-expressed GroEL chaperone.







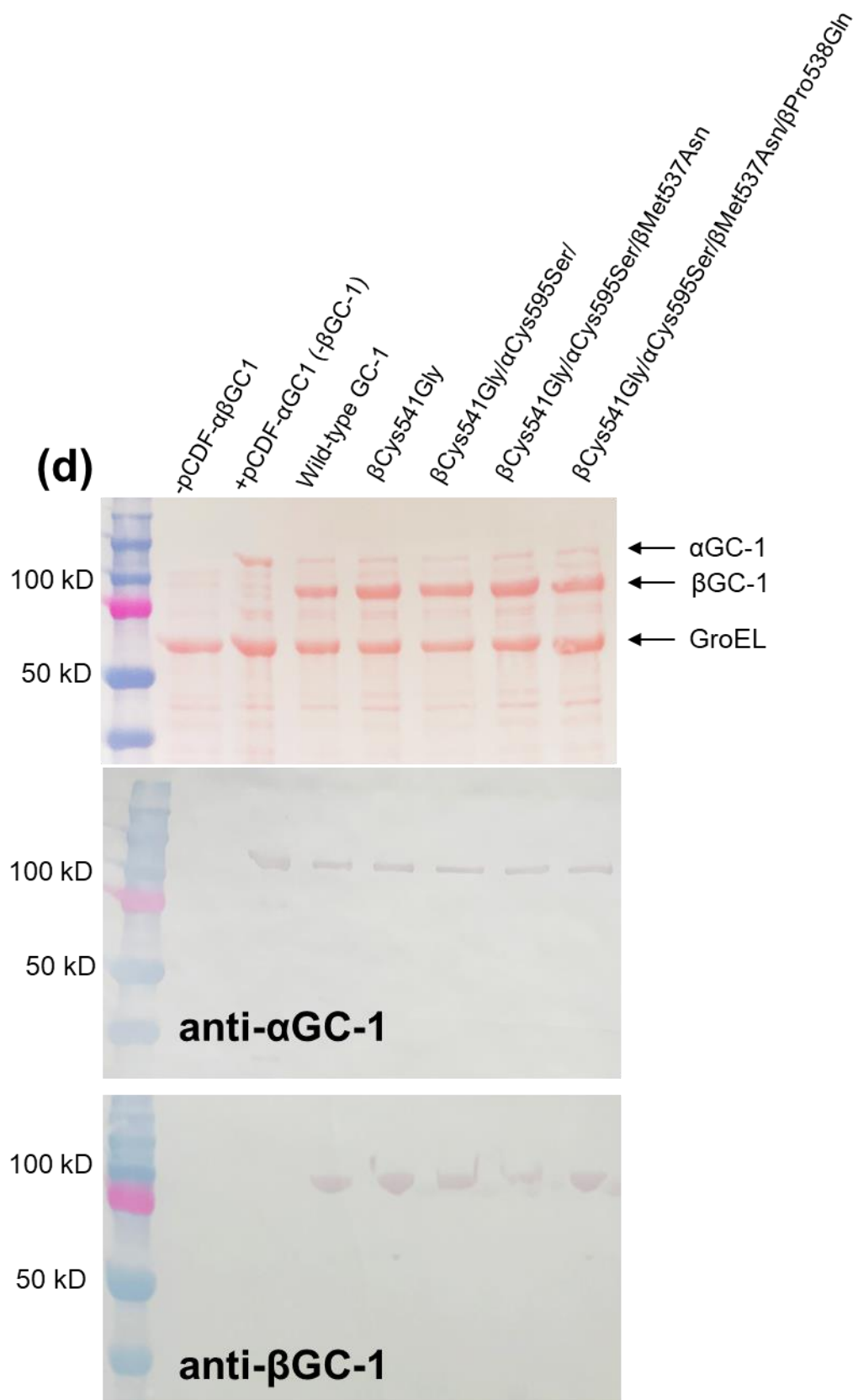


Figure A2. Expression test for wild-type and mutant GC-1. Western blot for expression of total protein for (a) inactive variants, (b) dorsal flap variants, (c) dimer interface variants, and (d) GTP-cleft variants. Each membrane was detected using Ponceau Red stain (top), anti- α GC-1 (middle), and anti- β GC-1 (bottom). Negative controls consisted of cells lacking either the $\alpha\beta$ GC-1 expression vector (-pCDF- $\alpha\beta$ GC1) or the β GC-1 gene (+pCDF- α GC1 (- β GC-1)). All samples were transformed with the pGro7 vector expressing the GroEL/ES chaperones.

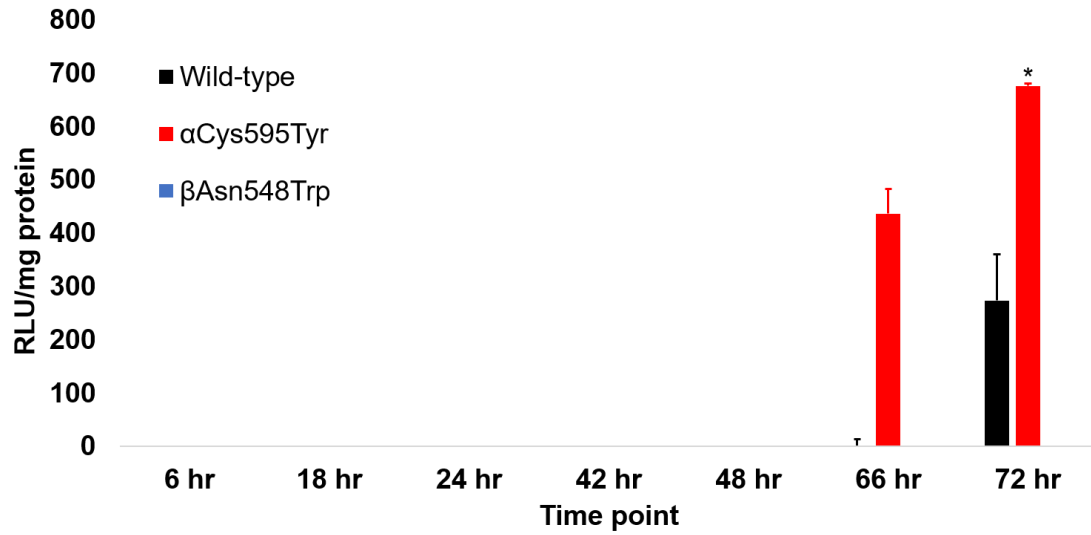


Figure A3. Luciferase activity induced by wild-type, α Cys595Tyr, and β Asn548Trp GC-1. Error bars represent the standard error of the mean from three or more experiments after background subtraction. Statistical significance between wild-type and α Cys595Tyr GC-1 cells at 72 hours was analyzed using Student's t-test (* $p < 0.05$).

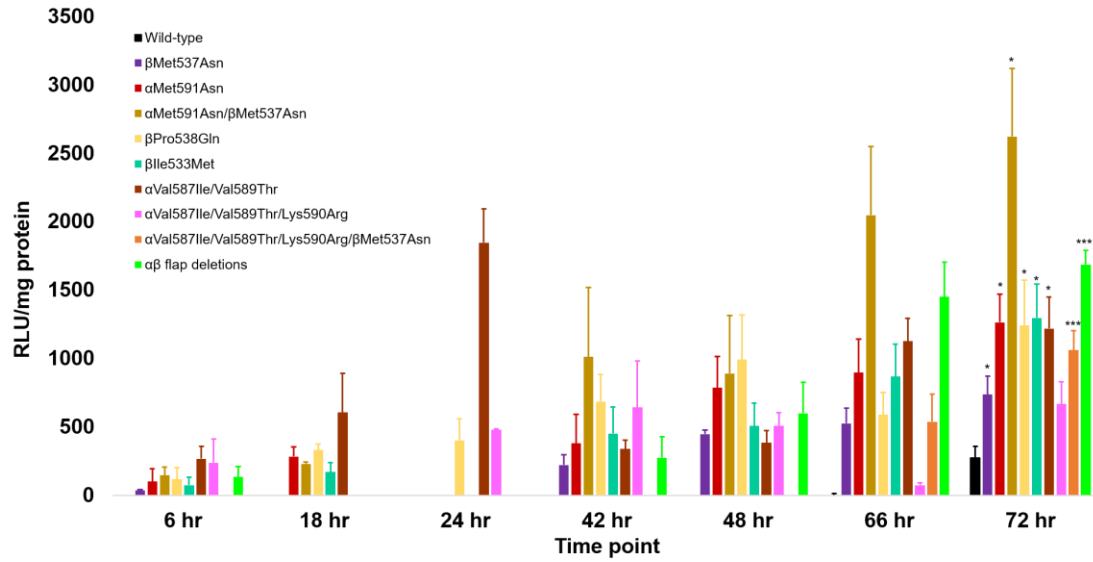


Figure A4. Luciferase activity induced by wild-type GC-1 and dorsal flap variants. Error bars represent the standard error of the mean from three or more experiments after background subtraction. Statistical significance between wild-type and mutant GC-1 cells was calculated using the Student's *t*-test (* $p < 0.05$; ** $p < 0.01$; *** $p < 0.001$).

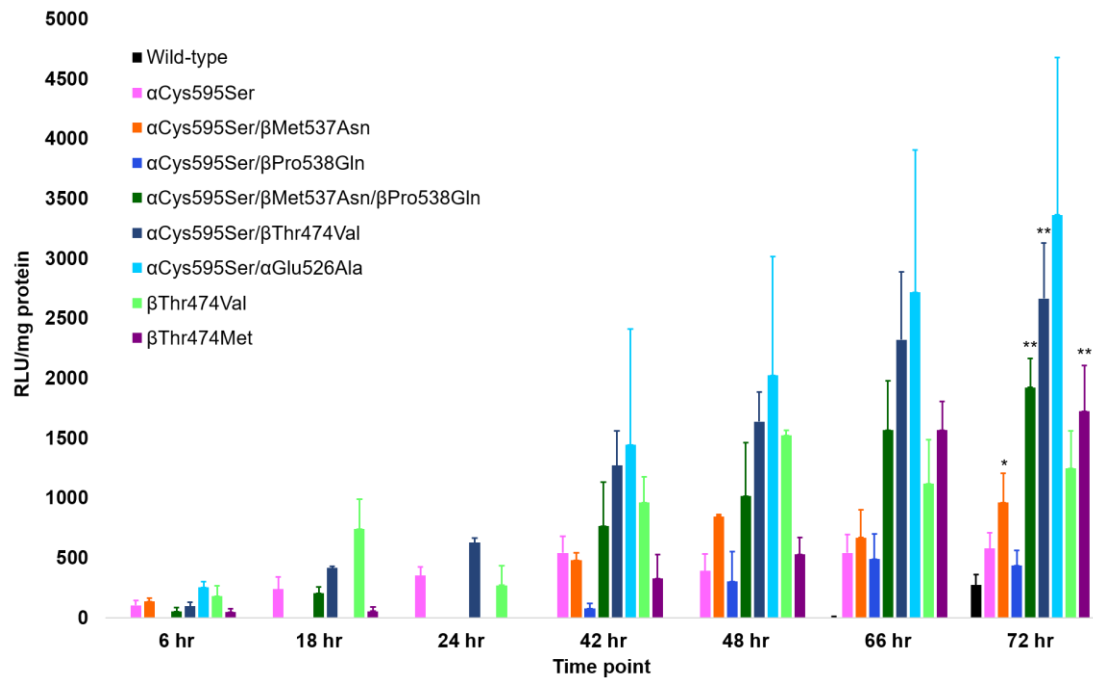


Figure A5. Luciferase activity induced by wild-type GC-1 and interfacial variants. Error bars represent the standard error of the mean from three or more experiments after background subtraction. Statistical significance between wild-type and mutant GC-1 cells was calculated using the Student's *t*-test (* $p < 0.05$; ** $p < 0.01$; *** $p < 0.001$).

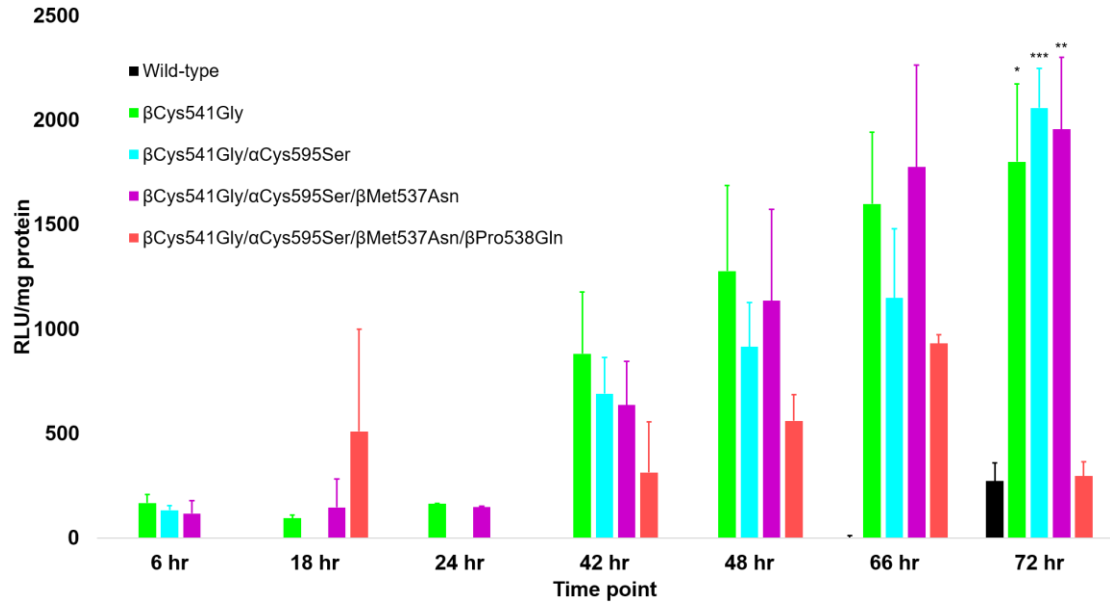


Figure A6. Luciferase activity induced by wild-type GC-1 and GTP-cleft variants. Error bars represent the standard error of the mean from three or more experiments after background subtraction. Statistical significance between wild-type and mutant GC-1 cells was calculated using the Student's *t*-test (* $p < 0.05$; ** $p < 0.01$; *** $p < 0.001$).

Bibliography

1. Ignarro, L. J., Buga, G. M., Wood, K. S., Byrns, R. E. & Chaudhuri, G. Endothelium-derived relaxing factor produced and released from artery and vein is nitric oxide. *Proc. Natl. Acad. Sci.* **84**, 9265–9269 (1987).
2. Palmer, R. M., Ferrige, A. G. & Moncada, S. Nitric oxide release accounts for the biological activity of endothelium-derived relaxing factor. *Nature* **327**, 524–526 (1987).
3. Arnold, W. P., Mittal, C. K., Katsuki, S. & Murad, F. Nitric oxide activates guanylate cyclase and increases guanosine 3':5'-cyclic monophosphate levels in various tissue preparations. *Proc. Natl. Acad. Sci.* **74**, 3203–3207 (1977).
4. Furchgott, R. F. The Discovery of Endothelium-Derived Relaxing Factor and Its Importance in the Identification of Nitric Oxide. *J. Am. Med. Assoc.* **276**, 1186–1188 (1996).
5. Stuehr, D. J. Structure-Function Aspects in the Nitric Oxide Synthases. *Annu. Rev. Pharmacol. Toxicol.* **37**, 339–359 (1997).
6. Venema, R. C., Sayegh, H. S., Kent, J. D. & Harrison, D. G. Identification, characterization, and comparison of the calmodulin-binding domains of the endothelial and inducible nitric oxide synthases. *J. Biol. Chem.* **271**, 6435–6440 (1996).
7. Santolini, J. The molecular mechanism of mammalian NO-synthases: A story of electrons and protons. *J. Inorg. Biochem.* **105**, 127–141 (2011).
8. Crane, B. R. *et al.* The structure of nitric oxide synthase oxygenase domain and

- inhibitor complexes. *Science* (80-.). **278**, 425–431 (1997).
9. Crane, B. R., Wu, C., Getzoff, E. D., Stuehr, D. J. & Tainer, J. A. Structure of Nitric Oxide Synthase Oxygenase Dimer with Pterin and Substrate. *Science* (80-.). **279**, 2121–2126 (1998).
 10. Fischmann, T. O. *et al.* Structural characterization of nitric oxide synthase isoforms reveals striking active-site conservation. *Nat. Struct. Biol.* **6**, 233–242 (1999).
 11. Flinspach, M. L. *et al.* Structural basis for dipeptide amide isoform-selective inhibition of neuronal nitric oxide synthase. *Nat. Struct. Mol. Biol.* **11**, 54–59 (2004).
 12. Raman, C. S. *et al.* Crystal structure of constitutive endothelial nitric oxide synthase: A paradigm for pterin function involving a novel metal center. *Cell* **95**, 939–950 (1998).
 13. Alderton, W. K., Cooper, C. E. & Knowles, R. G. Nitric oxide synthases: structure, function and inhibition. *Biochem. J.* **357**, 593–615 (2001).
 14. Poulos, T. L. & Li, H. Nitric oxide synthase and structure-based inhibitor design. *Nitric Oxide - Biol. Chem.* **63**, 68–77 (2017).
 15. Zhang, J. *et al.* Crystal structure of the FAD/NADPH-binding domain of rat neuronal nitric-oxide synthase: Comparisons with NADPH-cytochrome P450 oxidoreductase. *J. Biol. Chem.* **276**, 37506–37513 (2001).
 16. Garcin, E. D. *et al.* Structural basis for isozyme-specific regulation of electron transfer in nitric-oxide synthase. *J. Biol. Chem.* **279**, 37918–37927 (2004).
 17. Aoyagi, M., Arvai, A. S., Tainer, J. A. & Getzoff, E. D. Structural basis for

- endothelial nitric oxide synthase binding to calmodulin. *EMBO J.* **22**, 766–775 (2003).
18. Piazza, M., Futrega, K., Spratt, D. E., Dieckmann, T. & Guillemette, J. G. Structure and dynamics of calmodulin (CaM) bound to nitric oxide synthase peptides: Effects of a phosphomimetic CaM mutation. *Biochemistry* **51**, 3651–3661 (2012).
 19. Xia, C., Misra, I., Iyanagi, T. & Kim, J. J. P. Regulation of interdomain interactions by calmodulin in inducible nitric-oxide synthase. *J. Biol. Chem.* **284**, 30708–30717 (2009).
 20. Campbell, M. G., Smith, B. C., Potter, C. S., Carragher, B. & Marletta, M. A. Molecular architecture of mammalian nitric oxide synthases. *Proc. Natl. Acad. Sci. U. S. A.* **111**, E3614–23 (2014).
 21. Volkmann, N. *et al.* Holoenzyme Structures of Endothelial Nitric Oxide Synthase – an Allosteric Role for Calmodulin in Pivoting the FMN Domain for Electron Transfer. *J. structural Biol.* **188**, 46–54 (2014).
 22. Yokom, A. L. *et al.* Architecture of the nitric-oxide synthase holoenzyme reveals large conformational changes and a calmodulin-driven release of the FMN domain. *J. Biol. Chem.* **289**, 16855–16865 (2014).
 23. Salerno, J. C., Ray, K., Poulos, T., Li, H. & Ghosh, D. K. Calmodulin activates neuronal nitric oxide synthase by enabling transitions between conformational states. *FEBS Lett.* **587**, 44–47 (2013).
 24. Förstermann, U. & Sessa, W. C. Nitric oxide synthases: Regulation and function. *Eur. Heart J.* **33**, 829–837 (2012).

25. Fulton, D. J. R. Transcriptional and Posttranslational Regulation of eNOS in the Endothelium. in *Advances in Pharmacology* **77**, 29–64 (2016).
26. Song, T., Hatano, N., Horii, M., Tokumitsu, H. & Yamaguchi, F. Calcium/calmodulin-dependent protein kinase I inhibits neuronal nitric-oxide synthase activity through serine 741 phosphorylation. **570**, 133–137 (2004).
27. Rameau, G. A. *et al.* Biphasic Coupling of Neuronal Nitric Oxide Synthase Phosphorylation to the NMDA Receptor Regulates AMPA Receptor Trafficking and Neuronal Cell Death. *J. Neurosci.* **27**, 3445–3455 (2007).
28. Rameau, G. A., Chiu, L. Y. & Ziff, E. B. Bidirectional Regulation of Neuronal Nitric-oxide Synthase Phosphorylation at Serine 847 by the N-Methyl-D-aspartate Receptor. *J. Biol. Chem.* **279**, 14307–14314 (2004).
29. Dimmeler, S. *et al.* Activation of nitric oxide synthase in endothelial cells by Akt-dependent phosphorylation. *Lett. to Nat.* **399**, 601–605 (1999).
30. Fulton, D. *et al.* Regulation of endothelium- derived nitric oxide production by the protein kinase Akt. **399**, 597–601 (1999).
31. Bauer, P. M. *et al.* Compensatory Phosphorylation and Protein-Protein Interactions Revealed by Loss of Function and Gain of Function Mutants of Multiple Serine Phosphorylation Sites in Endothelial Nitric-oxide Synthase *. **278**, 14841–14849 (2003).
32. Michell, B. J. *et al.* Identification of Regulatory Sites of Phosphorylation of the Bovine Endothelial Nitric-oxide Synthase at Serine 617 and Serine 635. **277**, 42344–42351 (2002).
33. Boo, Y. C. *et al.* Shear stress stimulates phosphorylation of eNOS at Ser 635

- by a protein kinase A-dependent mechanism. **30322**, (2002).
34. Gallis, B. *et al.* Identification of Flow-dependent Endothelial Nitric-oxide Synthase Phosphorylation Sites by Mass Spectrometry and Regulation of Phosphorylation and Nitric Oxide Production by the Phosphatidylinositol 3-Kinase Inhibitor LY294002 *. **274**, 30101–30108 (1999).
 35. Butt, E. *et al.* Endothelial Nitric-oxide Synthase (Type III) Is Activated and Becomes Calcium Independent upon Phosphorylation by Cyclic Nucleotide-dependent Protein Kinases *. **275**, 5179–5187 (2000).
 36. Fulton, D. *et al.* Agonist-stimulated endothelial nitric oxide synthase activation and vascular relaxation: Role of eNOS phosphorylation at Tyr83. *Circ. Res.* **102**, 497–504 (2008).
 37. Fisslthaler, B., Loot, A. E., Mohamed, A., Busse, R. & Fleming, I. Inhibition of Endothelial Nitric Oxide Synthase Activity by Proline-Rich Tyrosine Kinase 2 in Response to Fluid Shear Stress and Insulin. (2008).
doi:10.1161/CIRCRESAHA.108.172072
 38. Zhang, Y. H. Neuronal nitric oxide synthase in hypertension – an update. *Clin. Hypertens.* **22**, 20 (2016).
 39. Bogdan, C. Nitric oxide synthase in innate and adaptive immunity: An update. *Trends Immunol.* **36**, 161–178 (2015).
 40. Guo, F. H. *et al.* Molecular Mechanisms of Increased Nitric Oxide (NO) in Asthma: Evidence for Transcriptional and Post-Translational Regulation of NO Synthesis. *J. Immunol.* **164**, 5970–5980 (2000).
 41. Hickok, J. R. & Thomas, D. D. Nitric Oxide and Cancer Therapy: The

- Emperor has NO Clothes. *Curr. Pharm. Des.* **16**, 381–391 (2010).
42. Feron, O., Michel, J. B., Sase, K. & Michel, T. Dynamic regulation of endothelial nitric oxide synthase: Complementary roles of dual acylation and caveolin interactions. *Biochemistry* **37**, 193–200 (1998).
43. Heiss, E. & Dirsch, V. Regulation of eNOS Enzyme Activity by Posttranslational Modification. *Curr. Pharm. Des.* **20**, 3503–3513 (2014).
44. Montfort, W. R., Wales, J. A. & Weichsel, A. Structure and Activation of Soluble Guanylyl Cyclase, the Nitric Oxide Sensor. *Antioxid. Redox Signal.* **26**, 107–121 (2016).
45. Socco, S., Bovee, R. C., Palczewski, M. B., Hickok, J. R. & Thomas, D. D. Epigenetics: The third pillar of nitric oxide signaling. *Pharmacol. Res.* **121**, 52–58 (2017).
46. Crane, B. R., Sudhamsu, J. & Patel, B. a. Bacterial nitric oxide synthases. *Annu. Rev. Biochem.* **79**, 445–470 (2010).
47. Shiva, S. Nitrite: A physiological store of nitric oxide and modulator of mitochondrial function. *Redox Biol.* **1**, 40–44 (2013).
48. Weitzberg, E. & Lundberg, J. O. Novel Aspects of Dietary Nitrate and Human Health. *Annu. Rev. Nutr.* **33**, 129–159 (2013).
49. Lundberg, J. O., Gladwin, M. T. & Weitzberg, E. Strategies to increase nitric oxide signalling in cardiovascular disease. *Nat. Rev. Drug Discov.* **14**, 623–41 (2015).
50. Ghofrani, H. A. *et al.* Riociguat: Mode of Action and Clinical Development in Pulmonary Hypertension. *Chest* **151**, 468–480 (2017).

51. Derbyshire, E. R. & Marletta, M. A. Structure and regulation of soluble guanylate cyclase. *Annu. Rev. Biochem.* **81**, 533–59 (2012).
52. Buys, E. S., Potter, L. R., Pasquale, L. R. & Ksander, B. R. Regulation of intraocular pressure by soluble and membrane guanylate cyclases and their role in glaucoma. *Front. Mol. Neurosci.* **7**, 1–15 (2014).
53. Fritz, B. G. *et al.* Oxidation and Loss of Heme in Soluble Guanylyl Cyclase from *Manduca Sexta*. *Biochemistry* **50**, 5813–5815 (2011).
54. Stasch, J. *et al.* Targeting the heme-oxidized nitric oxide receptor for selective vasodilatation of diseased blood vessels. *J. Clin. Invest.* **116**, 2552–2561 (2006).
55. Follmann, M. *et al.* The chemistry and biology of soluble guanylate cyclase stimulators and activators. *Angew. Chem. Int. Ed. Engl.* **52**, 9442–62 (2013).
56. Ghofrani, H.-A. *et al.* Riociguat for the Treatment of Chronic Thromboembolic Pulmonary Hypertension. *N. Engl. J. Med.* **369**, 319–329 (2013).
57. Martin, F. *et al.* Structure of cinaciguat (BAY 58-2667) bound to Nostoc H-NOX domain reveals insights into heme-mimetic activation of the soluble guanylyl cyclase. *J. Biol. Chem.* **285**, 22651–22657 (2010).
58. Gheorghiade, M. *et al.* Cinaciguat, a soluble guanylate cyclase activator: Results from the randomized, controlled, phase IIb COMPOSE programme in acute heart failure syndromes. *Eur. J. Heart Fail.* **14**, 1056–1066 (2012).
59. Zhou, Z. *et al.* Soluble guanylyl cyclase activation by HMR-1766 (ataciguat) in cells exposed to oxidative stress. *Am. J. Physiol. Heart Circ. Physiol.* **295**, H1763–71 (2008).

60. Wales, J. A. *et al.* Discovery of stimulator binding to a conserved pocket in the heme domain of soluble guanylyl cyclase. *J. Biol. Chem.* **293**, 1850–1864 (2018).
61. Altan-Yaycioglu, R., Türker, G., Akdöl, S., Acunaş, G. & Izgi, B. The Effects of Beta-Blockers on Ocular Blood Flow in Patients with Primary Open Angle Glaucoma: A Color Doppler Imaging Study. *Eur. J. Ophthalmol.* **11**, 37–46 (2001).
62. Kee, C., Kaufman, P. L. & Gabelt, B. T. Effect of ticrynafen on aqueous humor dynamics in monkeys. *Arch. Ophthalmol.* **35**, 2769–2773 (1994).
63. Kotikoski, H. *et al.* Comparison of nitric oxide donors in lowering intraocular pressure in rabbits: role of cyclic GMP. *J. Ocul. Pharmacol. Ther.* **18**, 11–23 (2002).
64. Buys, E. S. *et al.* Soluble Guanylate Cyclase $\alpha 1$ -Deficient Mice: A Novel Murine Model for Primary Open Angle Glaucoma. *PLoS One* **8**, (2013).
65. Ge, P. *et al.* The soluble guanylate cyclase stimulator IWP-953 increases conventional outflow facility in mouse eyes. *Investig. Ophthalmol. Vis. Sci.* **57**, 1317–1326 (2016).
66. Stasch, J.-P., Schlossmann, J. & Hocher, B. Renal effects of soluble guanylate cyclase stimulators and activators: A review of the preclinical evidence. *Curr. Opin. Pharmacol.* **21**, 95–104 (2015).
67. Wang, Y. *et al.* Enhancing cGMP in experimental progressive renal fibrosis: soluble guanylate cyclase stimulation vs. phosphodiesterase inhibition. *Am. J. Physiol. - Ren. Physiol.* **290**, F167–F176 (2006).

68. Hoffmann, L. S., Kretschmer, A., Lawrenz, B., Hoher, B. & Stasch, J.-P. Chronic Activation of Heme Free Guanylate Cyclase Leads to Renal Protection in Dahl Salt-Sensitive Rats. *PLoS One* **10**, 1–17 (2015).
69. Ito, K. *et al.* Dietary arginine supplementation attenuates renal damage after relief of unilateral ureteral obstruction in rats. *Kidney Int.* **68**, 515–528 (2005).
70. Russwurm, M., Behrends, S., Harteneck, C. & Koesling, D. Functional properties of a naturally occurring isoform of soluble guanylyl cyclase. *Biochemistry* **335**, 125–130 (1998).
71. Plate, L. & Marletta, M. A. Nitric oxide-sensing H-NOX proteins govern bacterial communal behavior. *Trends Biochem. Sci.* **38**, 566–575 (2013).
72. Purohit, R. *et al.* YC-1 Binding to the β Subunit of Soluble Guanylyl Cyclase Overcomes Allosteric Inhibition by the α Subunit. *Biochemistry* **53**, 101–114 (2014).
73. Zhao, Y., Schelvis, J. P., Babcock, G. T. & Marletta, M. A. Identification of histidine 105 in the β 1 subunit of soluble guanylate cyclase as the heme proximal ligand. *Biochemistry* **37**, 4502–9 (1998).
74. Zhao, Y., Brandish, P. E., Ballou, D. P. & Marletta, M. A. A molecular basis for nitric oxide sensing by soluble guanylate cyclase. *Proc. Natl. Acad. Sci.* **96**, 14753–14758 (1999).
75. Ibrahim, M., Derbyshire, E. R., Soldatova, A. V, Marletta, M. A. & Spiro, T. G. Soluble guanylate cyclase is activated differently by excess NO and by YC-1: resonance Raman spectroscopic evidence. *Biochemistry* **49**, 4864–71 (2010).
76. Russwurm, M. & Koesling, D. NO activation of guanylyl cyclase. *EMBO J.*

- 23**, 4443–50 (2004).
77. Martin, E., Berka, V., Sharina, I. & Tsai, A.-L. Mechanism of binding of NO to soluble guanylyl cyclase: implication for the second NO binding to the heme proximal site. *Biochemistry* **51**, 2737–46 (2012).
 78. Huang, C. *et al.* Guanylyl cyclase sensitivity to nitric oxide is protected by a thiol oxidation-driven interaction with thioredoxin-1. *J. Biol. Chem.* **292**, 14362–14370 (2017).
 79. Fernhoff, N. B., Derbyshire, E. R. & Marletta, M. A. A nitric oxide/cysteine interaction mediates the activation of soluble guanylate cyclase. *Proc. Natl. Acad. Sci. U. S. A.* **106**, 21602–7 (2009).
 80. Guo, Y. *et al.* Regulation of nitric oxide signaling by formation of a distal receptor-ligand complex. *Nat. Chem. Biol.* **13**, 1216–1221 (2017).
 81. Ma, X., Sayed, N., Baskaran, P., Beuve, A. & van den Akker, F. PAS-mediated dimerization of soluble guanylyl cyclase revealed by signal transduction histidine kinase domain crystal structure. *J. Biol. Chem.* **283**, 1167–1178 (2008).
 82. Purohit, R., Weichsel, A. & Montfort, W. R. Crystal structure of the Alpha subunit PAS domain from soluble guanylyl cyclase. *Protein Sci.* **22**, 1439–44 (2013).
 83. Sarkar, A. *et al.* Heat Shock Protein 90 Associates with the Per-Arnt-Sim Domain of Heme-free Soluble Guanylate Cyclase: Implications for Enzyme Maturation. *J. Biol. Chem.* (2015). doi:10.1074/jbc.M115.645515
 84. Ma, X., Beuve, A. & van den Akker, F. Crystal structure of the signaling helix

- coiled-coil domain of the beta1 subunit of the soluble guanylyl cyclase. *BMC Struct. Biol.* **10**, 2 (2010).
85. Fritz, B. G. *et al.* Molecular model of a soluble guanylyl cyclase fragment determined by small-angle X-ray scattering and chemical cross-linking. *Biochemistry* **52**, 1568–82 (2013).
86. Rothkegel, C. *et al.* Dimerization region of soluble guanylate cyclase characterized by bimolecular fluorescence complementation in vivo. *Mol. Pharmacol.* **72**, 1181–1190 (2007).
87. Campbell, M. G., Underbakke, E. S., Potter, C. S., Carragher, B. & Marletta, M. A. Single-particle EM reveals the higher-order domain architecture of soluble guanylate cyclase. *Proc. Natl. Acad. Sci.* **111**, 2960–2965 (2014).
88. Rauch, A., Leipelt, M., Russwurm, M. & Steegborn, C. Crystal structure of the guanylyl cyclase Cya2. *Proc. Natl. Acad. Sci. U. S. A.* **105**, 15720–5 (2008).
89. Winger, J. A., Derbyshire, E. R., Lamers, M. H., Marletta, M. A. & Kuriyan, J. The crystal structure of the catalytic domain of a eukaryotic guanylate cyclase. *BMC Struct. Biol.* **8**, (2008).
90. Allerston, C. K., von Delft, F. & Gileadi, O. Crystal structures of the catalytic domain of human soluble guanylate cyclase. *PLoS One* **8**, 1–9 (2013).
91. Seeger, F. *et al.* Interfacial residues promote an optimal alignment of the catalytic center in human soluble guanylate cyclase: heterodimerization is required but not sufficient for activity. *Biochemistry* **53**, 2153–2165 (2014).
92. Kumar, R. P. *et al.* Structure and monomer/dimer equilibrium for the guanylyl cyclase domain of the optogenetics protein RhoGC. *J. Biol. Chem.* **292**,

- 21578–21589 (2017).
93. Smigel, M. D. Purification of the catalyst of adenylate cyclase. *J. Biol. Chem.* **261**, 1976–1982 (1986).
 94. Zhang, G., Liu, Y., Ruoho, A. E. & Hurley, J. H. Structure of the adenylyl cyclase catalytic core. *Nature* **386**, 247–253 (1997).
 95. Tesmer, J. J., Sunahara, R. K., Gilman, A. G. & Sprang, S. R. Crystal Structure of the Catalytic Domains of Adenylyl Cyclase in a Complex with Gs·GTPS. *Science* (80-.). **278**, 1907–1916 (1997).
 96. Sunahara, R. K. Isoforms of Mammalian Adenylyl Cyclase: Multiplicities of Signaling. *Mol. Interv.* **2**, 168–184 (2002).
 97. Seifert, R., Lushington, G. H., Mou, T. C., Gille, A. & Sprang, S. R. Inhibitors of membranous adenylyl cyclases. *Trends Pharmacol. Sci.* **33**, 64–78 (2012).
 98. Jaggupilli, A. *et al.* Study of adenylyl cyclase-GαS interactions and identification of novel AC ligands. *Mol. Cell. Biochem.* (2018).
doi:10.1007/s11010-018-3273-4
 99. Pinto, C. *et al.* Activation and Inhibition of Adenylyl Cyclase Isoforms by Forskolin Analogs. *J. Pharmacol. Exp. Ther.* **325**, 27–36 (2008).
 100. Brand, C. S., Hocker, H. J., Gorfe, A. A., Cavasotto, C. N. & Dessauer, C. W. Isoform selectivity of adenylyl cyclase inhibitors: characterization of known and novel compounds. *J. Pharmacol. Exp. Ther.* **347**, 265–75 (2013).
 101. Lamothe, M., Chang, F.-J., Balashova, N., Shirokov, R. & Beuve, A. Functional characterization of nitric oxide and YC-1 activation of soluble guanylyl cyclase: structural implication for the YC-1 binding site?

- Biochemistry* **43**, 3039–48 (2004).
102. Ochoa de Alda, J. A. G., Ajlani, G. & Houmard, J. Synechocystis Strain PCC 6803 *cya2*, a prokaryotic gene that encodes a guanylyl cyclase. *J. Bacteriol.* **182**, 3839–3842 (2000).
103. Sunahara, R. K. *et al.* Exchange of Substrate and Inhibitor Specificities between Adenylyl and Guanylyl Cyclases. *J. Biol. Chem.* **273**, 16332–16338 (1998).
104. Friebe, A. *et al.* Functions of conserved cysteines of soluble guanylyl cyclase. *Biochemistry* **36**, 1194–8 (1997).
105. Friebe, A., Russwurm, M., Mergia, E. & Koesling, D. A Point-Mutated Guanylyl Cyclase with Features of the YC-1-Stimulated Enzyme: Implications for the YC-1 Binding Site? *Biochemistry* **38**, 15253–15257 (1999).
106. Beste, K. Y., Burhenne, H., Kaefer, V., Stasch, J. & Seifert, R. Nucleotidyl Cyclase Activity of Soluble Guanylyl Cyclase $\alpha 1\beta 1$. *Biochemistry* **51**, 194–204 (2011).
107. Gerzer, R., Hofmann, F. & Schultz, G. Purification of a Soluble, Sodium-Nitroprusside-Stimulated Guanylate Cyclase from Bovine Lung. *Eur. J. Biochem.* **116**, 479–486 (1981).
108. Humbert, P. *et al.* Purification of soluble guanylyl cyclase from bovine lung by a new immunoaffinity chromatographic method. *Eur. J. Biochem.* **190**, 273–278 (1990).
109. Wedel, B. *et al.* Functional domains of soluble guanylyl cyclase. *J. Biol. Chem.* **270**, 24871–24875 (1995).

110. Gupta, G., Kim, J., Yang, L., Sturley, S. L. & Danziger, R. S. Expression and purification of soluble, active heterodimeric guanylyl cyclase from baculovirus. *Protein Expr. Purif.* **10**, 325–30 (1997).
111. Hoenicka, M. *et al.* Purified soluble guanylyl cyclase expressed in a baculovirus/Sf9 system: stimulation by YC-1, nitric oxide, and carbon monoxide. *J. Mol. Med.* **77**, 14–23 (1999).
112. Wagner, C., Russwurm, M., Jager, R., Friebe, A. & Koesling, D. Dimerization of nitric oxide-sensitive guanylyl cyclase requires the alpha-1 N terminus. *J. Biol. Chem.* **280**, 17687–17693 (2005).
113. Winger, J. A., Derbyshire, E. R. & Marletta, M. A. Dissociation of nitric oxide from soluble guanylate cyclase and heme-nitric oxide/oxygen binding domain constructs. *J. Biol. Chem.* **282**, 897–907 (2006).
114. Derbyshire, E. R., Fernhoff, N. B., Deng, S. & Marletta, M. A. Nucleotide Regulation of Soluble Guanylate Cyclase Substrate Specificity. *Biochemistry* **48**, 7519–7524 (2009).
115. Sharina, I., Sobolevsky, M., Doursout, M.-F., Gryko, D. & Martin, E. Cobinamides are novel coactivators of nitric oxide receptor that target soluble guanylyl cyclase catalytic domain. *J. Pharmacol. Exp. Ther.* **340**, 723–32 (2012).
116. Winger, J. A. & Marletta, M. A. Expression and characterization of the catalytic domains of soluble guanylate cyclase: interaction with the heme domain. *Biochemistry* **44**, 4083–90 (2005).
117. Underbakke, E. S., Iavarone, A. T. & Marletta, M. A. Higher-order interactions

- bridge the nitric oxide receptor and catalytic domains of soluble guanylate cyclase. *Proc. Natl. Acad. Sci. U. S. A.* **110**, 6777–82 (2013).
118. Vijayaraghavan, J., Kramp, K., Harris, M. E. & van den Akker, F. Inhibition of soluble guanylyl cyclase by small molecules targeting the catalytic domain. *FEBS Lett.* **590**, 3669–3680 (2016).
 119. Hatley, M. E. *et al.* Isolation and characterization of constitutively active mutants of mammalian adenylyl cyclase. *J. Biol. Chem.* **275**, 38626–38632 (2000).
 120. Yuen, P. S. T., Doolittle, L. K. & Garbers, D. L. Dominant Negative Mutants of Nitric Oxide-sensitive Guanylyl Cyclase. *J. Biol. Chem.* **269**, 791–793 (1994).
 121. Tang, W. J., Stanzel, M. & Gilman, A. G. Truncation and Alanine-Scanning Mutants of Type I Adenylyl Cyclase. *Biochemistry* **34**, 14563–14572 (1995).
 122. Avelar, G. M. *et al.* A Rhodopsin-Guanylyl cyclase gene fusion functions in visual perception in a fungus. *Curr. Biol.* **24**, 1234–1240 (2014).
 123. Trieu, M. M. *et al.* Expression, purification, and spectral tuning of RhoGC, a retinylidene/guanylyl cyclase fusion protein and optogenetics tool from the aquatic fungus *Blastocladiella emersonii*. *J. Biol. Chem.* **292**, 10379–10389 (2017).
 124. Chang, F.-J., Lemme, S., Sun, Q., Sunahara, R. K. & Beuve, A. Nitric Oxide-dependent Allosteric Inhibitory Role of a Second Nucleotide Binding Site in Soluble Guanylyl Cyclase. *J. Biol. Chem.* **280**, 11513–11519 (2005).
 125. Surmeli, N. B., Mu, F. M. & Marletta, M. A. The Influence of Nitric Oxide on

- Soluble Guanylate Cyclase Regulation by Nucleotides. *J. Biol. Chem.* **290**, 15570–15580 (2015).
126. Wallace, S. *et al.* Disrupted nitric oxide signaling due to GUCY1A3 mutations increases risk for moyamoya disease, achalasia and hypertension. *Clin. Genet.* **90**, 351–360 (2016).
 127. Tesmer, J. J. *et al.* Two-metal-ion catalysis in adenylyl cyclase. *Science* (80-.). **285**, 756–760 (1999).
 128. Agulló, L., Buch, I., Gutiérrez-de-Terán, H., Garcia-Dorado, D. & Villà-Freixa, J. Computational exploration of the binding mode of heme-dependent stimulators into the active catalytic domain of soluble guanylate cyclase. *Proteins Struct. Funct. Bioinforma.* **84**, 1534–1548 (2016).
 129. Yazawa, S., Tsuchiya, H., Hori, H. & Makino, R. Functional Characterization of Two Nucleotide-binding Sites in Soluble Guanylate Cyclase. *J. Biol. Chem.* **281**, 21763–21770 (2006).
 130. Benhar, M., Forrester, M. T. & Stamler, J. S. Protein denitrosylation: Enzymatic mechanisms and cellular functions. *Nat. Rev. Mol. Cell Biol.* **10**, 721–732 (2009).
 131. Beuve, A. Thiol-Based Redox Modulation of Soluble Guanylyl Cyclase, the Nitric Oxide Receptor. *Antioxid. Redox Signal.* **26**, 137–149 (2016).
 132. Gould, N. S. *et al.* Site-Specific Proteomic Mapping Identifies Selectively Modified Regulatory Cysteine Residues in Functionally Distinct Protein Networks. *Chem. Biol.* **22**, 965–975 (2015).
 133. Gould, N., Doulias, P., Tenopoulou, M., Raju, K. & Ischiropoulos, H.

- Regulation of Protein Function and Signaling by Reversible Cysteine S-Nitrosylation. *J. Biol. Chem.* **288**, 26473–26479 (2013).
134. Smith, B. C. & Marletta, M. A. Mechanisms of S-nitrosothiol formation and selectivity in nitric oxide signaling. *Curr. Opin. Chem. Biol.* **16**, 498–506 (2012).
 135. Sayed, N., Baskaran, P., Ma, X., van den Akker, F. & Beuve, A. Desensitization of soluble guanylyl cyclase, the NO receptor, by S-nitrosylation. *Proc. Natl. Acad. Sci. U. S. A.* **104**, 12312–12317 (2007).
 136. Fernhoff, N. B., Derbyshire, E. R., Underbakke, E. S. & Marletta, M. A. Heme-assisted S-nitrosation desensitizes ferric soluble guanylate cyclase to nitric oxide. *J. Biol. Chem.* **287**, 43053–43062 (2012).
 137. Beuve, A. *et al.* Identification of novel S-nitrosation sites in soluble guanylyl cyclase, the nitric oxide receptor. *J. Proteomics* **138**, 40–47 (2016).
 138. Crassous, P.-A. *et al.* Soluble guanylyl cyclase is a target of angiotensin II-induced nitrosative stress in a hypertensive rat model. *AJP Hear. Circ. Physiol.* **303**, H597–H604 (2012).
 139. Hervé, D. *et al.* Loss of $\alpha 1\beta 1$ soluble guanylate cyclase, the major nitric oxide receptor, leads to moyamoya and achalasia. *Am. J. Hum. Genet.* **94**, 385–394 (2014).
 140. Mota, F., Allerston, C. K., Hampden-Smith, K., Garthwaite, J. & Selwood, D. L. Surface plasmon resonance using the catalytic domain of soluble guanylate cyclase allows the detection of enzyme activators. *Bioorg. Med. Chem. Lett.* **24**, 1075–1079 (2014).

141. Ben Aissa, M. *et al.* Soluble guanylyl cyclase is a critical regulator of migraine-associated pain. *Cephalalgia* (2017).
doi:10.1177/0333102417737778
142. Fernandes, D. *et al.* Late, but not early, inhibition of soluble guanylate cyclase decreases mortality in a rat sepsis model. *J. Pharmacol. Exp. Ther.* **328**, 991–999 (2009).
143. Pyriochou, A. *et al.* Soluble guanylyl cyclase activation promotes angiogenesis. *J. Pharmacol. Exp. Ther.* **319**, 663–671 (2006).
144. Fraser, M., Chan, S. L., Chan, S. S. L., Fiscus, R. R. & Tsang, B. K. Regulation of p53 and suppression of apoptosis by the soluble guanylyl cyclase/cGMP pathway in human ovarian cancer cells. *Oncogene* **25**, 2203–2212 (2006).
145. Tseng, K. Y. *et al.* Inhibition of striatal soluble guanylyl cyclase-cGMP signaling reverses basal ganglia dysfunction and Akinesia in experimental parkinsonism. *PLoS One* **6**, (2011).
146. Gille, A. *et al.* Differential Inhibition of Adenylyl Cyclase Isoforms and Soluble Guanylyl Cyclase by Purine and Pyrimidine Nucleotides. *J. Biol. Chem.* **279**, 19955–19969 (2004).
147. Mou, T. *et al.* Broad Specificity of Mammalian Adenylyl Cyclase for Interaction with 2',3'-Substituted Purine- and Pyrimidine Nucleotide Inhibitors. *Mol. Pharmacol.* **70**, 878–886 (2006).
148. Suryanarayana, S. *et al.* Differential Inhibition of Various Adenylyl Cyclase Isoforms and Soluble Guanylyl Cyclase by 2',3'-O-(2,4,6-Trinitrophenyl)-

- Substituted Nucleoside 5'-Triphosphates. *J. Pharmacol. Exp. Ther.* **330**, 687–695 (2009).
149. Dove, S., Danker, K. Y., Stasch, J.-P., Kaever, V. & Seifert, R. Structure/Activity Relationships of (M)ANT- and TNP-Nucleotides for Inhibition of Rat Soluble Guanylyl Cyclase $\alpha 1\beta 1$. *Mol. Pharmacol.* **85**, 598–607 (2014).
150. Mou, T.-C., Gille, A., Fancy, D. a, Seifert, R. & Sprang, S. R. Structural basis for the inhibition of mammalian membrane adenylyl cyclase by 2'-(3')-O-(N-Methylantraniloyl)-guanosine 5'-triphosphate. *J. Biol. Chem.* **280**, 7253–61 (2005).
151. Mota, F. *et al.* A new small molecule inhibitor of soluble guanylate cyclase. *Bioorganic Med. Chem.* **23**, 5303–5310 (2015).
152. Haase, T., Haase, N., Kraehling, J. R. & Behrends, S. Fluorescent fusion proteins of soluble guanylyl cyclase indicate proximity of the heme nitric oxide domain and catalytic domain. *PLoS One* **5**, 1–10 (2010).
153. Pan, J. *et al.* Probing the Molecular Mechanism of Human Soluble Guanylate Cyclase Activation by NO in vitro and in vivo. *Sci. Rep.* **7**, (2017).
154. Busker, M., Neidhardt, I. & Behrends, S. Nitric Oxide Activation of Guanylate Cyclase Pushes the $\alpha 1$ Signaling Helix and the $\beta 1$ Heme-binding Domain Closer to the Substrate-binding Site. *J. Biol. Chem.* **289**, 476–84 (2014).
155. Nienhaus, G. U. Exploring protein structure and dynamics under denaturing conditions by single-molecule FRET analysis. *Macromol. Biosci.* **6**, 907–922 (2006).

156. Underbakke, E. S. *et al.* Nitric Oxide-Induced Conformational Changes in Soluble Guanylate Cyclase. *Struct. Des.* **22**, 1–10 (2014).
157. Balashova, N., Chang, F., Lamothe, M., Sun, Q. & Beuve, A. Characterization of a Novel Type of Endogenous Activator of Soluble Guanylyl Cyclase. *J. Biol. Chem.* **280**, 2186–2196 (2005).
158. Heckler, E. J., Crassous, P., Baskaran, P. & Beuve, A. Protein disulfide-isomerase interacts with soluble guanylyl cyclase via a redox-based mechanism and modulates its activity. *Biochem. J.* **452**, 161–169 (2013).
159. Heckler, E. J., Kholodovych, V., Jain, M., Liu, T. & Li, H. Mapping Soluble Guanylyl Cyclase and Protein Disulfide Isomerase Regions of Interaction. *PLoS One* **10**, (2015).
160. Childers, K. C. & Garcin, E. D. Structure/function of the soluble guanylyl cyclase catalytic domain. *Nitric Oxide* **77**, 53–64 (2018).
161. Ma, X., Sayed, N., Beuve, A. & van den Akker, F. NO and CO differentially activate soluble guanylyl cyclase via a heme pivot-bend mechanism. *EMBO J.* **26**, 578–88 (2007).
162. Pellicena, P., Karow, D. S., Boon, E. M., Marletta, M. A. & Kuriyan, J. Crystal structure of an oxygen-binding heme domain related to soluble guanylate cyclases. *Proc. Natl. Acad. Sci. U. S. A.* **101**, 12854–9 (2004).
163. Nioche, P. *et al.* Femtomolar sensitivity of a NO sensor from *Clostridium botulinum*. *Science (80-.)*. **306**, 1550–1553 (2004).
164. Tews, I. *et al.* The Structure of a pH-Sensing Mycobacterial Adenylyl Cyclase Holoenzyme. *Science (80-.)*. **308**, 1020–1024 (2005).

165. Vercellino, I. *et al.* Role of the nucleotidyl cyclase helical domain in catalytically active dimer formation. *Proc. Natl. Acad. Sci.* **114**, E9821–E9828 (2017).
166. Lindner, R. *et al.* Photoactivation Mechanism of a Bacterial Light-Regulated Adenylyl Cyclase. *J. Mol. Biol.* **429**, 1336–1351 (2017).
167. Ohki, M. *et al.* Structural insight into photoactivation of an adenylate cyclase from a photosynthetic cyanobacterium. *Proc. Natl. Acad. Sci.* **113**, 6659–6664 (2016).
168. Steegborn, C. *et al.* A novel mechanism for adenylyl cyclase inhibition from the crystal structure of its complex with catechol estrogen. *J. Biol. Chem.* **280**, 31754–31759 (2005).
169. Saalau-Bethell, S. M. *et al.* Crystal structure of human soluble adenylate cyclase reveals a distinct, highly flexible allosteric bicarbonate binding pocket. *ChemMedChem* **9**, 823–832 (2014).
170. DelProposto, J., Majmudar, C. Y., Smith, J. L. & Clay, W. Mocr : A novel fusion tag for enhancing solubility that is compatible with structural biology applications. *Protein Expr. Purif.* **63**, 40–49 (2009).
171. Larkin, M. A. *et al.* Clustal W and Clustal X version 2.0. *Bioinformatics* **23**, 2947–2948 (2007).
172. Goujon, M. *et al.* A new bioinformatics analysis tools framework at EMBL–EBI. *Nucleic Acids Res.* **38**, W695–699 (2010).
173. Robert, X. & Gouet, P. Deciphering key features in protein structures with the new ENDscript server. *Nucleic Acids Res.* **42**, 320–324 (2014).

174. McWilliam, H. *et al.* Analysis Tool Web Services from the EMBL-EBI. *Nucleic Acids Res.* **41**, 597–600 (2013).
175. Wheeler, J. I., Freihat, L. & Irving, H. R. A cyclic nucleotide sensitive promoter reporter system suitable for bacteria and plant cells. *BMC Biotechnol.* **13**, 1–10 (2013).
176. Gomelsky, M. cAMP, c-di-GMP, c-di-AMP and now cGMP: Bacteria use them all! *Mol. Microbiol.* **79**, 562–565 (2011).
177. Linder, J. U. cGMP production in bacteria. *Mol. Cell. Biochem.* **334**, 215–219 (2010).
178. Ryu, M. H., Moskvina, O. V., Siltberg-Liberles, J. & Gomelsky, M. Natural and engineered photoactivated nucleotidyl cyclases for optogenetic applications. *J. Biol. Chem.* **285**, 41501–41508 (2010).
179. Ryu, M. H., Youn, H., Kang, I. H. & Gomelsky, M. Identification of bacterial guanylate cyclases. *Proteins Struct. Funct. Bioinforma.* **83**, 799–804 (2015).
180. Datsenko, K. A. & Wanner, B. L. One-step inactivation of chromosomal genes in *Escherichia coli* K-12 using PCR products. *Proc. Natl. Acad. Sci.* **97**, 6640–6645 (2000).
181. Seeger, F. Biochemical and Structural Characterization of Catalytic and Regulatory Constructs of Soluble Guanylate Cyclase. (2014).
182. Maathuis, F. J. M. cGMP modulates gene transcription and cation transport in *Arabidopsis* roots. *Plant J.* **45**, 700–711 (2006).
183. Beuve, A. & Danchin, A. From adenylate cyclase to guanylate cyclase. Mutational analysis of a change in substrate specificity. *J. Mol. Biol.* **225**, 933–

- 938 (1992).
184. Kleinboelting, S. *et al.* Crystal structures of human soluble adenylyl cyclase reveal mechanisms of catalysis and of its activation through bicarbonate. *Proc. Natl. Acad. Sci.* **111**, 3727–3732 (2014).
 185. Ziegler, M. *et al.* Characterization of a novel signal transducer element intrinsic to class IIIa/b adenylate cyclases and guanylate cyclases. *FEBS J.* **284**, 1204–1217 (2017).
 186. Guex, N., Peitsch, M. C. & Schwede, T. Automated comparative protein structure modeling with SWISS-MODEL and Swiss-PdbViewer: A historical perspective. *Electrophoresis* **30**, 162–173 (2009).
 187. Waterhouse, A. *et al.* SWISS-MODEL: homology modelling of protein structures and complexes. *Nucleic Acids Res.* **46**, W296–W303 (2018).
 188. Linder, J. U. Substrate selection by class III adenylyl cyclases and guanylyl cyclases. *IUBMB Life* **57**, 797–803 (2005).
 189. Yan, S., Huang, Z., Shaw, R. S. & Tang, W. The Conserved Asparagine and Arginine Are Essential for Catalysis of Mammalian Adenylyl Cyclase. *J. Biol. Chem.* **272**, 12342–12349 (1997).
 190. Tang, W. & Gilman, A. Construction of a soluble adenylyl cyclase activated by Gs alpha and forskolin. *Science (80-.).* **268**, 1769–1772 (1995).
 191. Yan, S. Z., Hahn, D., Huang, Z. H. & Tang, W.-J. Two cytoplasmic domains of mammalian adenylyl cyclase form a Gs α - and forskolin-activated enzyme in vitro. *J. Biol. Chem.* **271**, 10941–10945 (1996).
 192. Otwinowski, Z. & Minor, W. Processing of X-Ray Diffraction Data COLlected

- in Oscillation Mode. *Methods Enzymol.* **276**, (1997).
193. McCoy, A. J. *et al.* Phaser crystallographic software research papers. *J. Appl. Crystallogr.* **40**, 658–674 (2007).
 194. Adams, P. D. *et al.* PHENIX: Building new software for automated crystallographic structure determination. *Acta Crystallogr. Sect. D Biol. Crystallogr.* **58**, 1948–1954 (2002).
 195. Emsley, P., Lohkamp, B., Scott, W. G. & Cowtan, K. Features and development of Coot. *Acta Crystallogr. Sect. D Biol. Crystallogr.* **66**, 486–501 (2010).
 196. Krissinel, E. & Henrick, K. Inference of Macromolecular Assemblies from Crystalline State. *J. Mol. Biol.* **372**, 774–797 (2007).
 197. Shah, N. B. & Duncan, T. M. Bio-layer interferometry for measuring kinetics of protein-protein interactions and allosteric ligand effects. *J. Vis. Exp.* **84**, 1–7 (2014).
 198. Dove, S. Mammalian Nucleotidyl Cyclases and Their Nucleotide Binding Sites. in *Handbook of Experimental Pharmacology* 49–66 (2015).
doi:10.1007/164
 199. Hrabie, J. A., Klose, J. R., Wink, D. A. & Keefer, L. K. New Nitric Oxide-Releasing Zwitterions Derived from Polyamines. *J. Org. Chem.* **58**, 1472–1476 (1993).
 200. Chimenti, R., Martino, G., Mazzulla, S. & Sesti, S. Effect of Nitric Oxide Release from NOR-3 on Urea Synthesis, Viability and Oxygen Consumption of Rat Hepatocyte Cultures. *Physiol. Res.* **56**, 427–432 (2007).

201. Lai, Y. P., Huang, J., Wang, L. F., Li, J. & Wu, Z. R. A new approach to random mutagenesis in vitro. *Biotechnol. Bioeng.* **86**, 622–627 (2004).
202. Greene, E. a. *et al.* Spectrum of chemically induced mutations from a large-scale reverse-genetic screen in Arabidopsis. *Genetics* **164**, 731–740 (2003).
203. Greener, A., Callahan, M. & Jerpseth, B. An Efficient Random Mutagenesis Technique Using an E . coli Mutator Strain. *Mol. Biotechnol.* 189–195 (1997).
204. Vanhercke, T., Ampe, C., Tirry, L. & Denolf, P. Reducing mutational bias in random protein libraries. *Anal. Biochem.* **339**, 9–14 (2005).
205. Dokholyan, N. V. Controlling Allosteric Networks in Proteins. (2016).
doi:10.1021/acs.chemrev.5b00544

